Analysis of Thermoelectric Composites for Power Generation

I-Le Peng

A dissertation

submitted in partial fulfillment of the

requirements for the degree of

Doctor of Philosophy

University of Washington

2019

Reading Committee:

Jiangyu Li, Chair

Jihui Yang

Ashley Emery

Program Authorized to Offer Degree:

Mechanical Engineering

University of Washington

Abstract

Analysis of Thermoelectric Composites for Power Generation

I-Le Peng

Chair of the Supervisory Committee:
Professor Jiangyu Li
Mechanical Engineering

Thermoelectric composites are promising for energy conversion between heat and electricity. However, due to the complexity of nonlinear thermoelectric coupling, the effective behavior of the thermoelectric composites have not been explored much. The goal of this dissertation is to understand the effective behavior of the thermoelectric composites and to explore the possibility of improving their performance, excluding the size and interface effects. For this purpose, we studied three types of thermoelectric composites: one-dimensional and two-dimensional periodic thermoelectric composites with macroscopic homogeneity, and one-dimensional functionally graded materials.

In the first part of this dissertation, we adopt the non-linear asymptotic homogenization theory developed by Yang[1] and redefine the effective properties to understand the macroscopic behavior of one-dimensional thermoelectric composites. We discover that the effective behavior of the composites can be described by a single-phase material with homogenized properties, though the effective electric conductivity becomes temperature-dependent. We also find that although the effective figure of merit cannot be higher than both of its constituents, the effective power factor can be substantially improved.

In the second part of the thesis, we seek an improved the conversion efficiency by matching compatibility factor with reduced current density in a functionally graded material. The results show that the enhancement by the functionally graded strategy is insignificant because as we match the compatibility with reduced current density, the effective figure of merit is inevitably sacrificed.

In the last part of the thesis, we try to understand the behavior of two-dimensional thermoelectric composites. We first examine the asymptotic homogenization theory developed by Yang and note its limitations, and then we develop a direct finite element method as an alternative solution. Through the analysis, we found that the effective behavior of the two-dimensional thermoelectric can also be described by a homogenized single-phase material, and its effective properties do correlate with its conversion efficiency. Lastly, we develop a machine learning based methodology to speed up the search for better thermoelectric composites and reduced more than 95% of the computational cost from FEA. Through this study, we found no improved effective figure of merit from the combinations of the 16 state-of-the-art p-type thermoelectric materials at a wide temperature range. Nonetheless, the developed finite element method and machine learning methodology are proved to be effective in estimating the effective behavior of two-

dimensional thermoelectric composites, which can greatly accelerate the new composite discovery and design.

TABLE OF CONTENTS

LIST OF FIGURES

LIST OF TABLES

ACKNOWLEDGEMENTS

I am thankful to my advisor, Professor Jiangyu Li, for giving me this opportunity so that all these things can be possible. Also, I would like to thank my committee members including Professor Jihui Yang, Professor Ashley Emery, and Professor Mamidala Ramulu for their valuable time and advice.

I would like to thank my lab-mates, Dr. Yang Yang, Dr. Fieyue Ma, Dr. Nataly Chen, Dr. Peiqi Wang, Dr. Chi Hou Lei, Dr. Ahmad Eshghinejad, Dr. Ehsan Esfahani, and Boyuan Huang. Although I only overlap with many of them for less than two years, but I'm want to thank them for the helps they provided. I am so lucky to have so many brothers and sisters in the Church in Seattle who stand with me, support me and pray for me at every stage.

Lastly, I would like to thank my family for all their love and encouragement. For my parents who raised me and supported me in all my pursuits. And most of all for my wife, Tingyu Yen, whom I am so lucky to have on my side during every stage of this Ph.D. study. She supports me, helping me, encouraging me whatever happed. Thank you!

Chapter 1. INTRODUCTION AND OVERVIEW

1.1 THERMOELECTRIC EFFECT

The thermoelectric effect is the direct conversion of thermal to electrical energy and vice versa. The term "thermoelectric effect" encompasses three separately identified yet interrelated effects: Seebeck effect, Peltier effect, and Thomson effect.

1.1.1 *Seebeck Effect*

The Seebeck effect is the direct conversion of heat into electricity. It was observed in the early 1820s by physicist Thomas Johann Seebeck[2], who found that a voltage existed between two junctions of two different materials in the presence of a temperature difference between the junctions.

It was later discovered that the Seebeck effect is a type of electromotive force (EMF)[3] that drives free charge carriers to flow from the higher temperature side to the lower one due to a temperature gradient, leading to the accumulation of opposite charges on two sides which results in measurable currents or voltages, as illustrated in Figure 1.1. This can be described locally by the creation of an electromotive field

$$E_{emf} = -\alpha \nabla T, \tag{1.1}$$

where α is the Seebeck coefficient, a property of the local material, and ∇T is the gradient in temperature T. The sign of the Seebeck coefficient in equation (1.1) is positive/negative for positive/negative charge carriers. The presence of electromotive forces modifies Ohm's law by generating currents even in the absence of voltage differences (or generating voltage differences without electric currents). Including the effect of E_{emf}, the local current density is given by[4]

$$J = \sigma\left(-\nabla\phi + E_{emf}\right) = -\sigma(\nabla\phi + \alpha\nabla T), \tag{1.2}$$

where ϕ is the local electric potential and σ is the local electrical conductivity. And the equation of continuity of electric charge

$$\nabla \cdot \left(J - \frac{\delta}{\delta t} \epsilon \cdot \nabla \phi \right) = 0, \tag{1.3}$$

can be written as

$$\nabla \cdot \left(\epsilon \cdot \nabla \frac{\delta \phi}{\delta t} \right) + \nabla \cdot (\sigma \cdot \alpha \cdot \nabla T) + \nabla \cdot (\sigma \cdot \nabla \phi) = 0, \tag{1.4}$$

where ϵ is the dielectric permittivity.

1.1.2 *Peltier Effect*

The reverse of the Seebeck effect is called the Peltier effect. It was first discovered by physicist Jean Charles Athanase Peltier in 1834[2]. Considering a situation with an external EMF source applied and a current *I* passing through two junctions; a rate of heating q would occur at one junction along with a rate of cooling -*q* at the other. The ratio of *q* to *I* defines the Peltier coefficient (given by $\pi = q / I$), which represent the ability of a given material to carry heat through applied current. The sign of the Peltier coefficient is positive if the electric current and the heat flux are in the same direction. Thus, the local heat flux density, J_Q, is the combination of two effects: thermal conduction and the Peltier effect,

$$J_Q = -\kappa \nabla T + \pi J, \tag{1.5}$$

where $\kappa = \kappa_\phi + \kappa_\epsilon$ is the total thermal conductivity and is composed of the phonon component κ_ϕ and the electronic component κ_ϵ. The Seebeck coefficient and Peltier coefficient are related by

$$\alpha = \pi / T. \tag{1.6}$$

By inserting equations (1.2) and (1.6) into equation (1.5) we have[4]

$$J_Q = -\kappa \nabla T + T \alpha J = -T \alpha \sigma \nabla \phi - (T \alpha^2 \sigma + \kappa) \nabla T, \tag{1.7}$$

where the heat flux J_Q is coupled with current density J. The more general form of the equation of heat flow that covers the transient analysis became

$$J_Q = -T\alpha\sigma\nabla\phi - (T\alpha^2\sigma + \kappa)\nabla T + \rho C\frac{\partial T}{\partial t}, \tag{1.8}$$

where ρ is density, and C is specific heat capacity.

1.1.3 *Thomson Effect*

The last thermoelectric effect, the Thomson effect, relates to the rate of generation of reversible heat q resulted from the passage of a current along a portion of a single conductor wherein there is a temperature difference ΔT. Because the material properties are usually temperature-dependent, the temperature difference across the material usually results in the uneven distribution of the Seebeck coefficient as well as the Peltier coefficient. Such a difference results in heat production or absorption. The heat production per unit volume q is

$$q = -\mu J\nabla T, \tag{1.9}$$

where μ is the Thomson coefficient. The Thomson coefficient is also related to the Seebeck coefficient by

$$\mu = T\frac{d\alpha}{dT}. \tag{1.10}$$

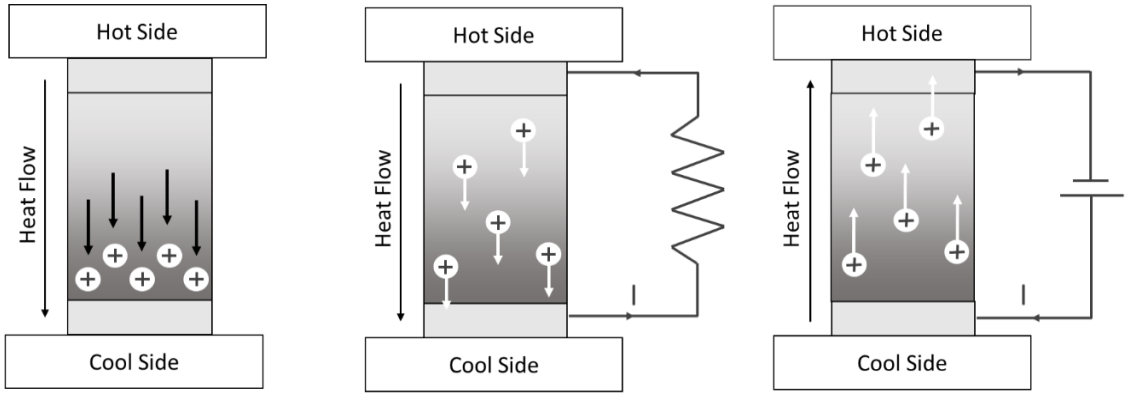

Figure 1.1: The temperature gradient drives holes in a p-type semiconductor to flow from the higher temperature side to the lower one, resulting in measurable voltage (left) or currents (middle). As an external EMF is imposed in the opposite direction, heat can be transported from the cold side to the hot side (right).

By combining the heat conduction, Joule heating, and both Peltier and Thomson effects we have the full heat equation,

$$0 = \nabla \cdot (\kappa \nabla T) + J \cdot (\sigma^{-1} J) - TJ \cdot \nabla \alpha + q_{ext} \tag{1.11}$$

where q_{ext} is the heat added from an external source (if applicable).

1.2 THERMOELECTRIC APPLICATIONS

Thermoelectric materials convert heat directly into electricity, and vice versa. Being solid-state without any moving parts, thermoelectric devices have many unique advantages[5]. First, they are very reliable in extreme environments. Second, they are quiet and do not vibrate in operation. Finally, they can be made into any sizes or shapes that make them extremely compatible and portable. On account of these unique characters, thermoelectric materials are promising in a wide range of power-generation and cooling applications.

1.2.1 *Thermoelectric Coolers*

A conventional cooling system, which includes an evaporator, a compressor, and a condenser, is quite complicated. In the evaporator, compressed refrigerant is allowed to expand, evaporate, and absorb heat. In the next step, the compressor recompresses the gaseous refrigerant into its liquid state. Then, the condenser expels the heat to the ambient environment. In contrast, a thermoelectric cooler only composed of N-type and P-type semiconductor connected electrically in series by metallic interconnects and thermally in parallel. As a DC power source is applied to a thermoelectric cooler, heat is transferred from one side to the other side by the Peltier effect as displayed in Figure 1.2.

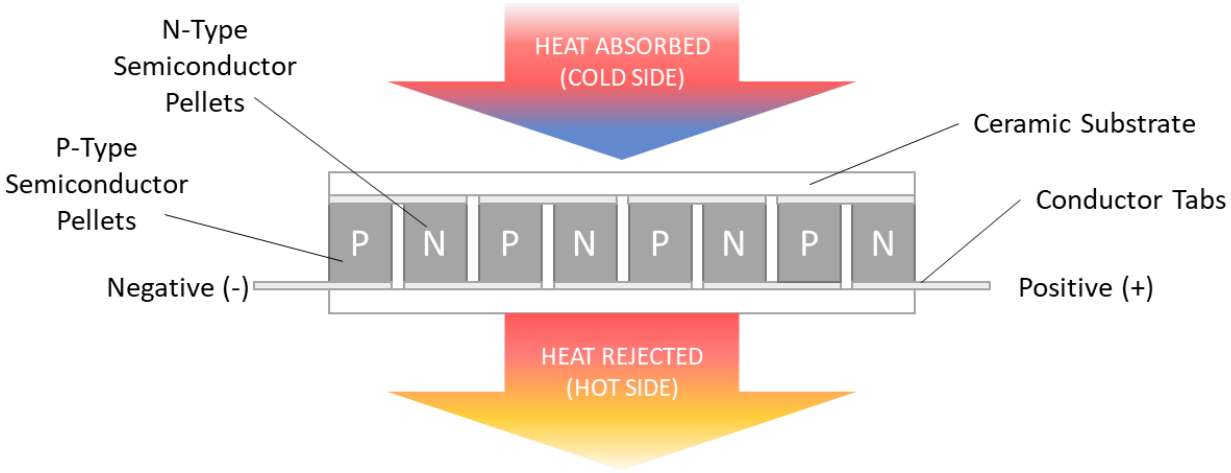

Figure 1.2: Structure and function of a thermoelectric cooler.

Due to the simplicity of the thermoelectric cooler, the associated maintenance is substantially reduced. Therefore, it has been widely used in military, such as submarines, as a cooling device for specific purposes[6,7]. Furthermore, thermoelectric coolers are also used in microelectronics to stabilize the temperature of laser diodes, to cool infrared detectors and charge-coupled devices, and to reduce unwanted noise of integrated circuits. The characteristics of small sizes and fast responses for thin film thermoelectric coolers make it possible to integrate cooling systems in microelectronic circuits[8,9].

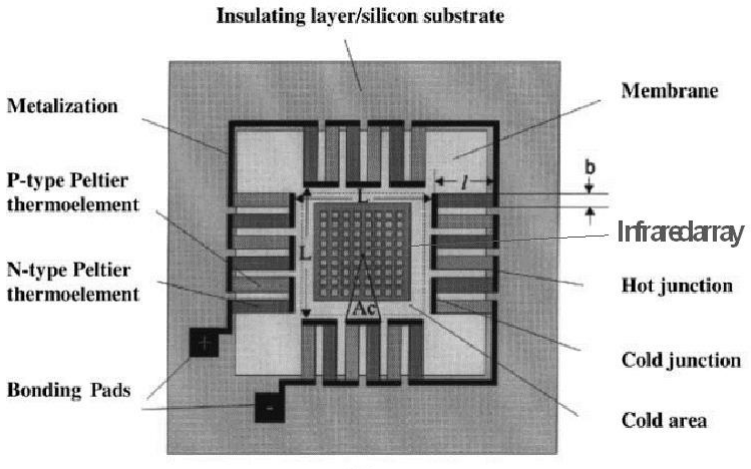

Figure 1.3: A schematic diagram showing an integrated thermoelectric microcooler with infrared components integrated onto cooled central region[8].

In recent years, climate change raises people's awareness of greenhouse gas emissions. As environmental regulations regarding the manufacture and release of (CFCs) increase, there is a need to seek alternatives to conventional refrigeration technologies. Thermoelectric devices, in which the electron gas serves as the working fluid and thus no refrigerants are used, may be expected to produce negligible direct emissions of greenhouse gases over their lifetimes[10,11].

1.2.2 *Thermoelectric Power Generation*

A thermoelectric generator is a unique heat engine-- it convers heat directly into electricity and, in principle, can use any thermal source. Furthermore, it has no moving parts, which in turn makes it very reliable. Therefore, the most established application of thermoelectric generator is using radioisotope thermoelectric generators (RTGs) in deep-space missions to provide reliable and long-lasting power sources[12], as shown in Figure 1.4(a). These RTGs provide decades of stable power sources for spacecraft in deep-space missions without any maintenance.

Another application of thermoelectric devices that have been actively studied and assessed is waste heat recovery. A typical gasoline-fueled internal combustion engine only uses 25% of the fuel energy for vehicle mobility and accessory power. The majority of the fuel energy is lost as waste heat[13]. Part of the waste heat can be recovered by integrating an automotive thermoelectric generator (ATEG) into the radiator and exhaust system, as seen in Figure 1.4(b). Beside the application on the automobiles, many researchers are exploiting potential applications on waste heat recovery in industries[14–17].

In current solar energy harvesting, photovoltaic solar cells use ultraviolet and visible sun light that accounts for 58% of the energy radiated from the sun. As shown in Figure 1.4(c), about 42% of total solar energy is in the infrared spectrum and is lost as heat, which can be potentially recovered by thermoelectric materials[18,19]. Thermoelectric materials can also be used to power

self-sustained wireless systems such as sensors placed in critical or even hazardous places: chimneys, pipelines, mines[20,21], etc. Moreover, they can be used to power wearable devices, as seen Figure 1.4(d), such as smart watches, smart glasses, and even hearing aids, with which battery life is still a challenging problem to be solved[22]. There are many more potential applications not mentioned here[8,23,24], and what hinders them to be realized is the poor performance of thermoelectric materials.

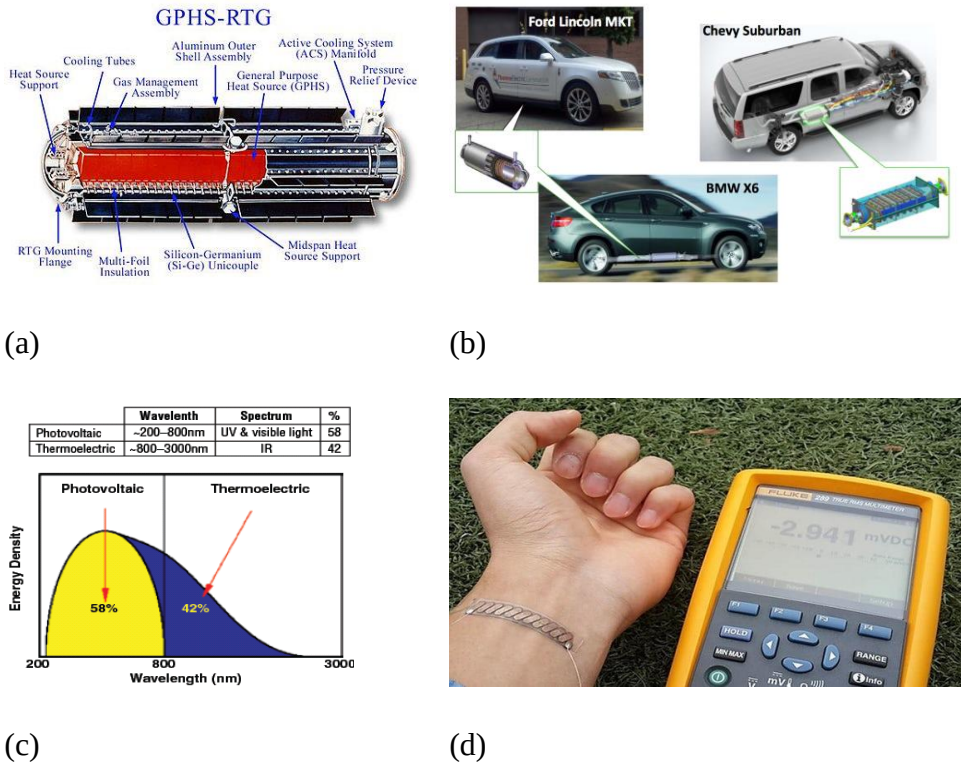

	Wavelenth	Spectrum	%
Photovoltaic	~200–800nm	UV & visible light	58
Thermoelectric	~800–3000nm	IR	42

(a) (b)

(c) (d)

Figure 1.4: Thermoelectric materials applications: (a) Configuration of a general-purpose heat source radioisotope thermoelectric generator (RTGs)[12]; (b) Automotive thermoelectric generator (ATEG) tested by auto manufacturers[13]; (c) Solar energy with a part in the ultraviolet and visible light, and the rest in the infrared[19]; (d) A wearable thermoelectric generator developed by a research group at KAIST[22].

1.3 THERMOELECTRIC POWER FACTOR AND FIGURE OF MERIT

When it comes to the performance of a thermoelectric material, two material parameters are often mentioned, thermoelectric power factor and figure of merit[25].

1.3.1 *Thermoelectric Power Factor*

The power factor of a thermoelectric material is calculated by its Seebeck coefficient and electric conductivity:

$$Power\ factor = \alpha^2\sigma \tag{1.12}$$

Materials with a higher power factor are able to generate more energy from the same temperature difference in a space-constrained condition. The maximum power output of a single TE element for a temperature difference ∇T

$$P_{max} = I_{opt} \cdot \nabla\phi_{opt} = -\sigma\left(\nabla\phi_{opt} + \alpha\nabla T\right) \cdot A \times \nabla\phi_{opt} = \alpha^2\sigma \cdot \frac{A\nabla T^2}{4} \tag{1.13}$$

is proportional to its power factor. Considering cooling applications, the cooling effect at the source junction is opposed by both Joule heating and heat conduction. As half of the Joule heating travels to each junction, the rate of heat absorption from the source can be written as,

$$Q = \alpha T_C I - \frac{1}{2}I^2R - K(T_H - T_C) \tag{1.14}$$

The maximum absorption rate is obtained when $I = \frac{\alpha T_C}{R}$ as

$$Q_{max} = \frac{1}{2}\frac{\alpha^2 T_C}{R} - K(T_H - T_C) = \frac{1}{2}\frac{\alpha^2\sigma A}{L} - K(T_H - T_C) \tag{1.15}$$

This shows that materials with a high power factor are also able to move more heat in a cooling application, but they are not necessarily more efficient in generating or moving energy.

1.3.2 *Thermoelectric Figure of Merit*

A thermoelectric material's conversion efficiency is determined by its dimensionless figure of merit, given by

$$ZT = \frac{\alpha^2 \sigma}{\kappa} T \tag{1.16}$$

In power generation, the maximum thermoelectric efficiency *H*,

$$H = \frac{energy\ supplied\ to\ the\ load}{heat\ energy\ absorbed\ at\ hot\ junction} \tag{1.17}$$

is given by[26]

$$H_{max} = \frac{T_H - T_C}{T_H} \frac{\sqrt{1+Z\bar{T}}-1}{\sqrt{1+Z\bar{T}}+\frac{T_C}{T_H}} \tag{1.18}$$

where $\bar{T} = \frac{T_H + T_C}{2}$, and all the material properties are assumed to be constant. The first term on the right hand side of equation (1.18) is the efficiency of the Carnot cycle, and the second is highly dependent on the thermoelectric figure of merit. As the value of the figure of merit goes higher, the maximum efficiency is closer to the Carnot efficiency.

In cooling applications, the performance of a refrigerator is expressed by its coefficient of performance (COP), which is defined as the cooling power produced divided by the rate of electrical energy supplied. The optimized COP can be written as

$$COP = \frac{heat\ absorbed}{electrical\ power\ input} = \frac{T_C}{T_H - T_C} \frac{\sqrt{1+Z\bar{T}}-\frac{T_H}{T_C}}{\sqrt{1+Z\bar{T}}+1} \tag{1.19}$$

which is also governed by the thermoelectric figure of merit.

1.4 Recent Development of Thermoelectric Materials

Prior to the 1990s, researchers had been searching for bulk materials with intrinsically high power factor and figure of merit for a few decades without much progress being made. It is especially

hard to find a bulk material with high figure of merit. To have high figure of merit, the thermoelectric materials need to have not only high Seebeck coefficient, but also high electric conductivity and low thermal conductivity, and these properties are intimately related to each other, making it hard to control them separately[27–29]. For example, while high electric conductivity requires a high concentration of charge carriers, a modest carrier concentration is optimal for high Seebeck coefficient[30]. Moreover, high electric conductivity usually comes with high thermal conductivity because of the Wiedemann-Franz law[31].

One possible solution to overcoming the intrinsic constraints between electric conductivity, thermal conductivity, and Seebeck coefficient in a single-phase material is to combine different materials. Through microstructure engineering and optimization, high electric conductivity, Seebeck coefficient, and low thermal conductivity can be achieved simultaneously[32–38]. In recent years, by taking advantages of size and interface effects, researchers were able to find great enhancement in thermoelectric figure of merit for a number of composite systems[39–42], as demonstrated in Figure 1.5.

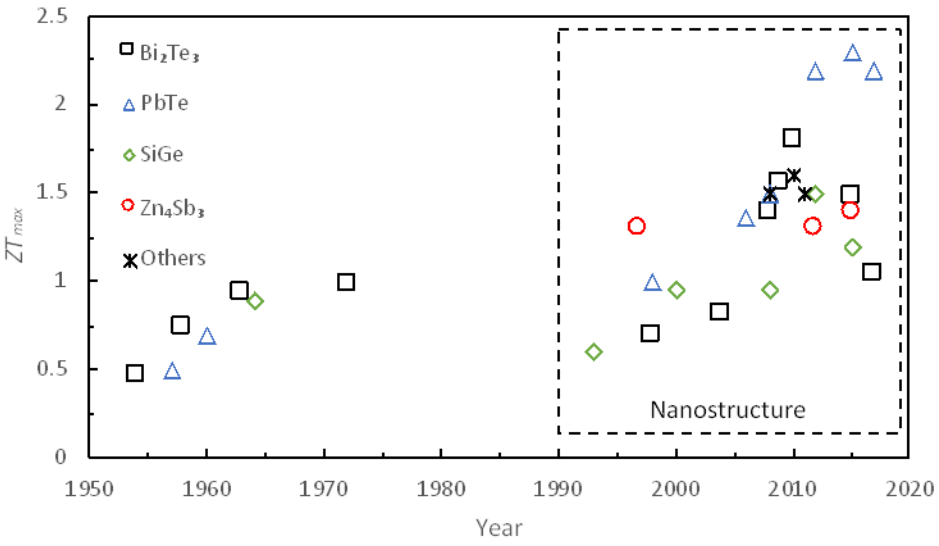

Figure 1.5: Development of ZT in the past decades shows pronounced improvement for nanostructured Bi2Te3[39,43–52], PbTe[53–61], SiGe[62–67], Zn4Sb3[68–70] series, and other good thermoelectric materials[68–70].

1.5 Motivation and Objectives

While a large number of experimental works in thermoelectric materials focus on nanostructured composites, and most theoretical studies focus on size and interfacial effects at the nanoscale using molecular dynamics and quantum mechanics[56,71–74], there have been very few theoretical efforts toward the continuum analysis of their effective behavior[1,75,76]. In earlier studies, it was argued that the effective figure of merit of a composite is bounded by the figure of merit of its constituents[77,78]. However, the analysis was built on linearized thermoelectric transport equations. The formerly suggested conclusion consequently needs to be further examined. Furthermore, heat flux has often been assumed to be divergence free, which is also not appropriate for thermoelectric materials with coupled transport of electricity and heat.

Lately, Yang used more realistic nonlinear analysis to examine the effective behavior of thermoelectric composites with different configurations. In his analysis, he took the temperature and the variation of heat flux into account, but treated material properties as constants. He first examined the bi-layered composites and found that the efficiency of the composite could be higher than both of its constituents, but the effective figure of merit was no longer correlated with the conversion efficiency[79,80]. He also examined the effective behavior of a two-phase periodic laminate thermoelectric composite. He derived the governing equations for the macroscopic temperature, potential distribution, heat flux, and electric current density. He further analyzed the overall conversion efficiency using an idealized thermoelectric module[1]. However, he did not answer the question of whether the conversion efficiency of the composite was bounded by its constituents or not. In a later study, Yang did a similar analysis on the thermoelectric composite with 2D unit cell configuration and derived its own governing equations[81]. But how this composite behaves remains unanswered. These are the questions that we seek to answer in this study.

1.6 OVERVIEW

The main reason that Yang did not mention whether the efficiency of the two-phase periodic laminate thermoelectric composites could be higher or not is that the effective figure of merit defined by him was found not to correlate with the thermoelectric conversion efficiency. As a result, he had no useful tool to examine it. Therefore, in Chapter 2, we define a new set of effective properties, so that we have an effective figure of merit to be correlated with conversion efficiency, and effective power factor correlated with maximum power output. Then, we examine the boundedness of both figure of merit and power factor. In Chapter 3, we extend our scope to functionally graded material by using the effective properties derived in Chapter 2 and the reduced variable method. In Chapter 4, we analyze the effective behavior of the thermoelectric composite

for 2D unit cell configuration base on Yang's asymptotic analysis and found many limitations through that path. Therefore, in the next chapter we took another route to analyze the behavior of thermoelectric composite with finite element method and found the effective properties of the composite defined by the finite element method does correlate the performance of the composite. In Chapter 6, we apply the basic machine learning algorithm to the data generated by the method developed in the previous chapter and show how accurate and efficient a machine learning model can predict the effective properties of thermoelectric composite. Chapter 7 summarizes the main conclusions of the dissertation, which finally lead to the discussion of future work.

Chapter 2. EFFECTIVE PROPERTIES OF PERIODIC LAYERED THERMOELECTRICS

2.1 INTRODUCTORY REMARKS

To investigate whether a thermoelectric composite with periodic microstructure, as schematically shown in Figure 2.1, can have a higher conversion efficiency than any of its constituents, a nonlinear asymptotic homogenization theory was developed by Yang[1]. In the next section, we will give the general idea and results of this theory. In his study, the effective thermoelectric properties are defined in a way that the effective thermoelectric figure of merit does not directly correlate with the thermoelectric conversion efficiency. Therefore, we will define a new set of effective properties to lead to an effective figure of merit that correlates with conversion efficiency. With this new effective figure of merit, we will examine the boundedness of the thermoelectric conversion efficiency and present numerical results and discussions.

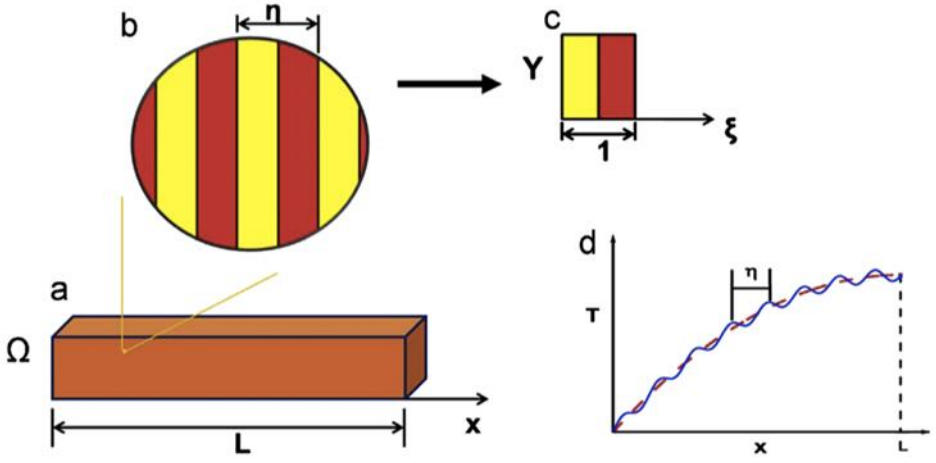

Figure 2.1. Schematics of layered composite in (a) macroscopic, (b) mesoscopic, and (c) microscopic scales, with (d) fast fluctuating actual field (solid blue line) and slow varying homogenized field (dashed red line)[1].

2.2 THEORETICAL FRAMEWORK

2.2.1 *Asymptotic Analysis*

The scope of the analysis covered in this section is confined to one-dimension, wherein all the field variables and material parameters are assumed to vary only along the x-coordinate. Also, all the material properties are assumed to be independent of temperature. The thermoelectric transport equations (1.1) and (1.3) are thus simplified to be

$$-J = \sigma \frac{d\phi}{dx} + \sigma\alpha \frac{dT}{dx}, \tag{2.1}$$

$$J_Q = \alpha T J - \kappa \frac{dT}{dx}. \tag{2.2}$$

In addition, the divergence-free current density implies that $J = |J| = const$ in 1D, and the field equation for heat flux is simplified as

$$\frac{dJ_Q}{dx} = -\frac{d\phi}{dx} J. \tag{2.3}$$

The object is a 1D composite consisting of two distinct phases layered periodically. For such a composite, two different length scales can be identified: L, the macroscopic length of the composite associated with the macroscopic coordinate x, and η, the characteristic length of the composite unit cell, for which a microscopic coordinate ξ can be introduced. While material properties $\alpha(\xi)$, $\sigma(\xi)$, and $\kappa(\xi)$ vary fast on the microscopic scale periodically, field variables such as $T(x,\xi)$, $\phi(x,\xi)$, and $J_Q(x,\xi)$ vary fast on the microscopic scale yet change slowly on the macroscopic scale, as shown in Fig. 2.1(d). The temperature, potential, and heat flux then are expanded into polynomials of η

$$T(x,\xi) = T_0(x,\xi) + \eta T_1(x,\xi) + \eta^2 T_2(x,\xi) + \cdots, \tag{2.4}$$

$$\phi(x,\xi) = \phi_0(x,\xi) + \eta \phi_1(x,\xi) + \eta^2 \phi_2(x,\xi) + \cdots, \tag{2.5}$$

$$J_Q(x,\xi) = J_{Q0}(x,\xi) + \eta J_{Q1}(x,\xi) + \eta^2 J_{Q2}(x,\xi) + \cdots. \tag{2.6}$$

Substituting these into governing equations (2.1) and (2.3) for T and ϕ, we obtain a series of equations grouped by the orders of η. Based on these equations, we know that $T_0(x,\xi) = T_0(x)$ and $\phi_0(x,\xi) = \phi_0(x)$ represent the macroscopic distributions of temperature and potential, which we are interested in. By integrating those equations over one unit cell, the governing equation for the macroscopic temperature distribution $T_0(x)$ in the layered composite

$$\frac{d^2T_0}{dx^2} + \left\langle\frac{1}{\sigma}\right\rangle\left\langle\frac{1}{\kappa}\right\rangle J^2 - \left(\left\langle\frac{\alpha}{\kappa}\right\rangle^2 - \left\langle\frac{\alpha^2}{\kappa}\right\rangle\left\langle\frac{1}{\kappa}\right\rangle\right)J^2T_0 = 0 \tag{2.7}$$

and the governing equation for the macroscopic potential distribution ϕ_0 (x) in the layered composite

$$\frac{d\phi_0}{dx} = -\left\langle\frac{1}{\sigma}\right\rangle J - \left\langle\frac{\alpha}{\kappa}\right\rangle\left\langle\frac{1}{\kappa}\right\rangle^{-1}\frac{dT_0}{dx} + \left(\left\langle\frac{1}{\kappa}\right\rangle^{-1}\left\langle\frac{\alpha}{\kappa}\right\rangle^2 - \left\langle\frac{\alpha^2}{\kappa}\right\rangle\right)JT_0 \tag{2.8}$$

are derived, where $\langle . \rangle$ indicates volume averaged quantities over the unit cell.

2.2.2 *Field Analysis*

With the governing equations (2.7) and (2.8), the temperature and potential distribution can be solved, given the imposed boundary conditions $T(0)$, $T(L)$, $\phi(0)$, $\phi(L)$, yielding

$$T_0(x) = q_1\cos\left(\sqrt{d_1}x\right) + q_2\sin\left(\sqrt{d_1}x\right) - \frac{d_2}{d_1} \tag{2.9}$$

where

$$d_1 = \left(\left\langle\frac{\alpha^2}{\kappa}\right\rangle\left\langle\frac{1}{\kappa}\right\rangle - \left\langle\frac{\alpha}{\kappa}\right\rangle^2\right)J^2,$$

$$d_2 = \left\langle\frac{1}{\sigma}\right\rangle\left\langle\frac{1}{\kappa}\right\rangle J^2,$$

$$q_1 = \frac{d_2}{d_1} + T(0),$$

$$q_2 = \frac{d_2/d_1 + T(L) - q_1\cos\left(\sqrt{d_1}L\right)}{\sin\left(\sqrt{(d_1)}L\right)},$$

and

$$\phi_0 = h_1 x + h_2 \sin\left(\sqrt{d_1}x\right) + h_3 cos\left(\sqrt{d_1}x\right) + h_4 \tag{2.10}$$

where

$$h_1 = -\left\langle\frac{1}{\sigma}\right\rangle J - \left(\left\langle\frac{1}{\kappa}\right\rangle^{-1}\left\langle\frac{\alpha}{\kappa}\right\rangle^2 - \left\langle\frac{\alpha^2}{\kappa}\right\rangle\right) J\frac{q_2}{q_1},$$

$$h_2 = -\left\langle\frac{1}{\kappa}\right\rangle^{-1}\left\langle\frac{\alpha}{\kappa}\right\rangle q_2 + \left(\left\langle\frac{1}{\kappa}\right\rangle^{-1}\left\langle\frac{\alpha}{\kappa}\right\rangle^2 - \left\langle\frac{\alpha^2}{\kappa}\right\rangle\right) J\frac{q_1}{\sqrt{d_1}},$$

$$h_3 = -\left\langle\frac{1}{\kappa}\right\rangle^{-1}\left\langle\frac{\alpha}{\kappa}\right\rangle q_1 + \left(\left\langle\frac{1}{\kappa}\right\rangle^{-1}\left\langle\frac{\alpha}{\kappa}\right\rangle^2 - \left\langle\frac{\alpha^2}{\kappa}\right\rangle\right) J\frac{q_2}{\sqrt{d_1}},$$

$$h_4 = \phi(0) - h_3.$$

As the current density J can be determined from potential boundary condition at x=L, the heat and energy fluxes can be determined to be

$$J_{Q0} = -\left\langle\frac{1}{\kappa}\right\rangle^{-1}\left[\left(-q_1\sqrt{d_1} - \left\langle\frac{\alpha}{\kappa}\right\rangle J q_2\right)\sin\left(\sqrt{d_1}x\right)\right.$$
$$\left. + \left(q_2\sqrt{d_1} - \left\langle\frac{\alpha}{\kappa}\right\rangle J q_1\right)\cos\left(\sqrt{d_1}x\right) + \left\langle\frac{\alpha}{\kappa}\right\rangle J\frac{d_2}{d_1}\right], \tag{2.11}$$

and

$$J_U = \left\langle\frac{1}{\kappa}\right\rangle^{-1}\left(\left\langle\frac{\alpha}{\kappa}\right\rangle T_0 J - \frac{dT_0}{dx}\right) + \phi_0 J. \tag{2.12}$$

2.2.3 *Effective Properties and Conversion Efficiency*

The effective thermoelectric properties are defined through the following equivalency principle. Given the same boundary conditions of temperature and electric potential, a thermoelectric composite with a set of effective thermoelectric properties should have equal current density and energy flux as a homogeneous thermoelectric with the same set of properties. With such equivalency, it is clear that the composite and homogeneous material can be mathematically exchanged in governing equations under the specified boundary conditions.

Using such equivalency principle, the effective Seebeck coefficient and effective thermal conductivity are defined under the open-circuit boundary condition (where $J = 0$), and can be derived from equations (2.8) and (2.11) as

$$\alpha^* = -\frac{d\phi_0}{dT_0} = \left\langle \frac{\alpha}{\kappa} \right\rangle, \tag{2.13}$$

and

$$\kappa^* = -\frac{J_{Q0}}{dT_0/dx} = \left\langle \frac{1}{\kappa} \right\rangle^{-1}. \tag{2.14}$$

As far as the effective electric conductivity is concerned, the close-circuit boundary condition with $\Delta T = 0$ is imposed, and the effective electric conductivity of the periodic composite is given by

$$\sigma^* = -\frac{J}{\frac{\Delta\phi}{L}} = \frac{2}{\nu\Delta\phi}\tan^{-1}\left\{\frac{\left\langle \frac{1}{\kappa} \right\rangle \nu\Delta\phi}{2\left[\left\langle \frac{1}{\sigma} \right\rangle \left\langle \frac{1}{\kappa} \right\rangle + \nu^2 T(0)\right]}\right\}, \tag{2.15}$$

where

$$\nu = \sqrt{\left\langle \frac{\alpha^2}{\kappa} \right\rangle \left\langle \frac{1}{\kappa} \right\rangle - \left\langle \frac{\alpha^2}{\kappa} \right\rangle}.$$

The effective thermoelectric figure of merit is then defined as

$$Z^* = \frac{\sigma^* \alpha^{*2}}{\kappa^*}. \tag{2.16}$$

It is worth noting that the effective electric conductivity depends on the imposed potential difference at boundaries and therefore is not an intrinsic property. As a result, there is a need to revisit the definition of thermoelectric figure of merit ZT for the composite. The thermoelectric conversion efficiency has to be examined directly through

$$H = \frac{A\cdot\phi(L)J}{A\cdot J_U\,|x=0} = \frac{\phi(L)J}{\left\langle \frac{1}{\kappa} \right\rangle^{-1}\left(\left\langle \frac{\alpha}{\kappa} \right\rangle T(0)J - \frac{dT_0}{dx}|x=0\right)}, \tag{2.17}$$

where the numerator denotes the electric energy delivered to the load resistance and the denominator denotes the heat (energy) flowing in at the joint from the hot reservoir with temperature $T(0)$. Here $\phi(0) = 0$ is assumed without loss of generality. The optimal conversion efficiency has to be evaluated numerically with respect to the current density.

2.3 Alternative Definition of The Effective Electric Conductivity

In Yang's study[1], it is concluded that the behavior of thermoelectric composite materials is very different from the behavior of homogeneous materials, and there is a large discrepancy between the actual efficiency and the efficiency evaluated from the effective figure of merit, which depends on the boundary condition. Since it is not applicable to examine the boundedness of the conversion efficiency with the effective figure of merit defined by Yang, we are motivated to seek alternative definitions for effective properties of thermoelectric composites. In so doing, the effective figure of merit is defined to correlate with the conversion efficiency, with which we can exam the boundedness of the conversion efficiency of the layered composites.

In the real world, in order to measure the intrinsic electrical conductivity of the material, we need to make sure that the whole object is kept at a constant temperature, and the electrical current needs to be limited to avoid detectable Joule heating. To do so, the imposed electric potential difference has to be small. This concept reveals a way to redefine the effective electric conductivity. We thus define the effective electric conductivity in the limit case of equation (2.15) where $\Delta\phi$ approaches 0, giving

$$\sigma^* = \lim_{\Delta\phi\to 0} -\frac{K(\Delta\phi)}{\Delta\phi/L} = \left[\left\langle\frac{1}{\sigma}\right\rangle + \left(\left\langle\frac{\alpha^2}{\kappa}\right\rangle - \left\langle\frac{\alpha}{\kappa}\right\rangle^2 \left\langle\frac{1}{\kappa}\right\rangle^{-1}\right) T(0)\right]^{-1}. \tag{2.18}$$

It is then clear that the effective electric conductivity no longer depends on the imposed potential difference at the boundary. Instead, it depends on the thermoelectric properties of the constituents,

the volume fraction *f*, and temperature. This explains why the effective electric conductivity appears dependent on the imposed potential difference in Yang's study. As the imposed potential difference increases, the electrical current density increases and causes Joule heating. Although the temperatures at two ends are set to be constant, the temperature between the two ends goes higher due to the Joule heating. Since the effective electric conductivity is temperature dependent, the average effective electric conductivity changes with respect to the actual temperature distribution.

Since the effective Seebeck coefficient and effective thermal conductivity defined by Yang are already intrinsic, there is no need to redefine them. Applying effective properties as defined in equations (2.13), (2.14), and (2.18) to the governing equations for field distributions, equations (2.7) and (2.8), the governing equations for field distributions can be written as

$$\frac{d^2T_0}{dx^2} + \frac{1}{\sigma^*\kappa^*}J^2 = 0, \tag{2.19}$$

$$\frac{d\phi_0}{dx} = -\frac{J}{\sigma^*} + \alpha^*\frac{dT}{dx} = 0. \tag{2.20}$$

where equations (2.19), and (2.20) are the same as the governing equations for homogeneous material. Up to this point, we can declare that the behavior of the periodic layered thermoelectric composite is the same as its homogeneous counterpart with temperature dependent electric conductivity, and the average effective figure of merit can be used to predict the maximum efficiency at a small temperature difference between the cold and hot sides (as we will show in the next section).

2.4 BOUNDEDNESS OF THERMOELECTRIC FIGURE OF MERIT

Now we have the effective figure of merit expressed as

$$Z^* = \frac{\alpha^{*2}\sigma^*}{\kappa^*} = \frac{\left\langle\frac{\alpha}{\kappa}\right\rangle^2}{\left\langle\frac{1}{\kappa}\right\rangle\left[\left\langle\frac{1}{\sigma}\right\rangle+\left(\left\langle\frac{\alpha^2}{\kappa}\right\rangle-\left\langle\frac{\alpha}{\kappa}\right\rangle^2\left\langle\frac{1}{\kappa}\right\rangle^{-1}\right)T\right]}. \tag{2.21}$$

First, we exam a special case with T = 0, and the figure of merit can be simplified as

$$Z^* = \frac{\left\langle\frac{\alpha}{\kappa}\right\rangle^2}{\left\langle\frac{1}{\kappa}\right\rangle\left\langle\frac{1}{\sigma}\right\rangle} = \frac{\left[\frac{\alpha_1}{\kappa_1}(1-f)+\frac{\alpha_2}{\kappa_2}f\right]^2}{\left[\frac{1}{\kappa_1}(1-f)+\frac{1}{\kappa_2}f\right]\left[\frac{1}{\sigma_1}(1-f)+\frac{1}{\sigma_2}f\right]}, \tag{2.22}$$

where f is the volume fraction of the second phase. To further simplify the calculation, we set $\frac{\alpha_2}{\alpha_1} = \alpha_r, \frac{\kappa_2}{\kappa_1} = \kappa_r, \frac{\sigma_2}{\sigma_1} = \sigma_r$, and the figure of merit can be written as

$$Z^* = \frac{\alpha_1^2\sigma_1}{\kappa_1}\frac{\left[(1-f)+\frac{\alpha_r}{\kappa_r}f\right]^2}{\left[(1-f)+\frac{1}{\kappa_r}f\right]\left[(1-f)+\frac{1}{\sigma_r}f\right]} = Z_1 Z_r. \tag{2.23}$$

By doing this we reduce the number of variables from seven to four. The simplest way to see if Z^* is bounded or not is to differentiate it by f once and see if it changes sign in the interval of $0 \leq f \leq 1$. If it does not change sign in this interval, the value of Z^* will always sits between two values corresponding to the two ends of the interval, Z_1 and Z_2. For this purpose, we focus on Z_r alone, and

$$\frac{dZ_r}{df} = -\frac{A(B+f\cdot C)}{D} \tag{2.24}$$

where

$$A(f) = [\alpha_r f + \kappa_r(1-f)]\sigma_r,$$

$$B = \kappa_r^2 + \kappa_r\sigma_r - 2\alpha_r\kappa_r\sigma_r,$$

$$C = 2\kappa_r - \alpha_r\kappa_r - \kappa_r^2 - \alpha_r\sigma_r - \kappa_r\sigma_r + 2\alpha_r\kappa_r\sigma_r,$$

$$D(f) = \kappa_r[f + \kappa_r(1-f)]^2[f + \sigma_r(1-f)]^2.$$

It is clear that A and D are always positive in the interval of $0 \leq f \leq 1$, and $B + fC$ is a linear function. In order to have a value of which is lower than both Z_1 and Z_2, B has to be greater than zero and $B + C$ has to be smaller than zero, that is, the slop of $Z^*(f)$ has to be negative at $f = 0$, and positive at $f = 1$,

$$B = \kappa_r^2 + \kappa_r\sigma_r - 2\alpha_r\kappa_r\sigma_r > 0, \tag{2.25}$$

$$B + C = 2\kappa_r - \alpha_r(\kappa_r + \sigma_r) < 0, \tag{2.26}$$

and these give the relationship of α_r, κ_r, and σ_r as

$$\frac{2\kappa_r}{\kappa_r+\sigma_r} < \alpha_r < \frac{\kappa_r+\sigma_r}{2\sigma_r} \tag{2.27}$$

which is only valid when

$$\frac{2\kappa_r}{\kappa_r+\sigma_r} < \frac{\kappa_r+\sigma_r}{2\sigma_r}. \tag{2.28}$$

requiring that

$$4\kappa_r\sigma_r < (\kappa_r + \sigma_r)^2. \tag{2.29}$$

This is valid as long as $\kappa_r \neq \sigma_r$, showing that the figure of merit is unbounded by its constituents. In the other case, in order to have a value of Z^* that is higher than both Z_1 and Z_2, B has to be smaller than zero and $B + C$ has to be greater than zero, and the relationship below has to be true

$$4\kappa_r\sigma_r > (\kappa_r + \sigma_r)^2, \tag{2.30}$$

which can be rewritten as

$$(\kappa_r - \sigma_r)^2 < 0, \tag{2.31}$$

which cannot hold true. Thus, the effective figure of merit can only be lower but not higher than both Z_1 and Z_2 when $T = 0$.

Now, as we take T into account, the effective figure of merit becomes a function of T

$$Z^* = \frac{\left\langle \frac{\alpha}{\kappa} \right\rangle^2}{\left\langle \frac{1}{\kappa} \right\rangle \left[\left\langle \frac{1}{\sigma} \right\rangle + E \cdot T \right]}, \tag{2.32}$$

where

$$E = \left\langle \frac{\alpha^2}{\kappa} \right\rangle - \left\langle \frac{\alpha}{\kappa} \right\rangle^2 \left\langle \frac{1}{\kappa} \right\rangle^{-1},$$

which can be easily proved to be always positive. In other words, with any given T, it makes the denominator larger, which in turn makes the effective figure of merit smaller. In conclusion, the effective figure of merit can only be lower than both its constituents and it is negatively dependent on T.

2.5 Boundedness of Thermoelectric Power Factor

With the well-defined effective properties, we can also examine the boundedness of the thermoelectric power factor. Following the same path, the effective power factor can be written as

$$PF^* = \frac{\left\langle \frac{\alpha}{\kappa} \right\rangle^2 \left\langle \frac{1}{\kappa} \right\rangle^{-2}}{\left[\left\langle \frac{1}{\sigma} \right\rangle + \left(\left\langle \frac{\alpha}{\kappa} \right\rangle^2 \left\langle \frac{1}{\kappa} \right\rangle^{-1} \right) T \right]}. \tag{2.33}$$

For the special, best case with T=0, the effective power factor can be simplified as

$$PF^* = \alpha_1^2 \sigma_1 \frac{\left[(1-f) + \frac{\alpha_r}{\kappa_r} f \right]^2}{\left[(1-f) + \frac{1}{\sigma_r} f \right] \left[(1-f) + \frac{1}{\kappa_r} f \right]^2} = W_1 \cdot W_r. \tag{2.34}$$

For an improved power factor, $\frac{dW_r}{df}$ must be greater than zero at $f = 0$ and less than zero at $f = 1$, namely,

$$\kappa_r^2 + 2\sigma_r \kappa_r - \sigma_r \kappa_r^2 - 2\alpha_r \kappa_r \sigma_r < 0 \; and \; 2\kappa_r - \alpha_r (2\kappa_r + \sigma_r - 1) > 0. \tag{2.35}$$

As we are interested in seeing if we can have an improved power factor even if the second material has a lower power factor, we add two additional conditions

$$0 < |\alpha_r| < 1 \; and \; 0 < \alpha_r^2 \sigma_r < 1, \tag{2.36}$$

and we know that thermal and electrical conductivities are always positive,

$$\kappa_r > 0 \; and \; \sigma_r > 0. \tag{2.37}$$

It can be proved that, under the conditions shown below, the thermoelectric power factor of a composite can be higher than both its constituents, which is consistent with the conclusion from Bergman[77].

$$\begin{cases} 0 < \alpha_r < 1 \\ \kappa_r > \frac{\alpha_r+1}{2\alpha_r} \wedge \kappa_r > \frac{2}{\alpha_r+1}, \\ \frac{\kappa_r}{2\alpha_r+\kappa_r-2} < \sigma_r < \frac{1}{\alpha_r^2} \end{cases} \tag{2.38}$$

$$\begin{cases} 0 < \alpha_r < 1 \\ \sqrt{\alpha_r^2 - \alpha_e + 1} - \alpha_r + 1 < \kappa_r < \frac{\alpha_r+1}{2\alpha_r}, \\ \frac{\kappa_r}{2\alpha_r+\kappa_r-2} < \sigma_r < -\frac{2\alpha_r\kappa_r+\alpha_r+2\kappa_r}{\alpha_r} \end{cases} \tag{2.39}$$

$$\begin{cases} -1 < \alpha_r < 0 \\ \frac{2}{\alpha_r+1} < \kappa_r \\ \frac{\kappa_r}{2\alpha_r+\kappa_r-2} < \sigma_r < \frac{1}{\alpha_r^2} \end{cases}. \tag{2.40}$$

2.6 Numerical Results and Discussions

2.6.1 *Effective Electrical Conductivity and Conversion Efficiency*

For demonstration purposes, we consider the same kind of composite in this study: a periodic thermoelectric composite consisting of Bi_2Te_3 and $Ag\left(Pb_{1-y}\,Sn_y\right)_m SbTe_{2+m}$, with their thermoelectric properties listed in Table 2.1 and the volume fraction of Bi_2Te_3 being f.

We first consider situations of only the electric potential difference being imposed, with $\phi(0) = 0V$ at one end and three different potential $\phi(L) = 0.1,\ 0.05,\ 0.01V$ at the other end. The corresponding distributions of temperature and effective electric conductivity are shown in Figure 2.2, where $f = 0.4$ is assumed, and effective electric conductivity defined by Yang is also included

for comparison. It is observed that a noticeable temperature bump is produced due to Joule heating while the higher potential difference is imposed. Also, the effective electric conductivity varies due to the temperature variation. On the other hand, while imposing a smaller potential difference, the temperature, as well as the effective electric conductivity, is almost constant, and that is how we can define the effective electric conductivity in one specific temperature. Moreover, we define the effective electric conductivity at the material level. In contrast to this approach, the imposed potential difference is not confined to be small in Yang's definition for the effective electric conductivity, which also takes all effects into account and is defined at the device level. We, then, define the effective electric conductivity at the material level.

Table 2.1. Thermoelectric properties of Bi_2Te_3 and $Ag\left(Pb_{1-y}\,Sn_y\right)_m SbTe_{2+m}$.

Material	$\alpha\ (\times 10^{-6} V/K)$	$\sigma\ (\times 10^{3} S/m)$	$\kappa\ (W/m/K)$
Bi_2Te_3	200	110	1.6
$Ag\left(Pb_{1-y}\,Sn_y\right)_m SbTe_{2+m}$	270	22	0.77

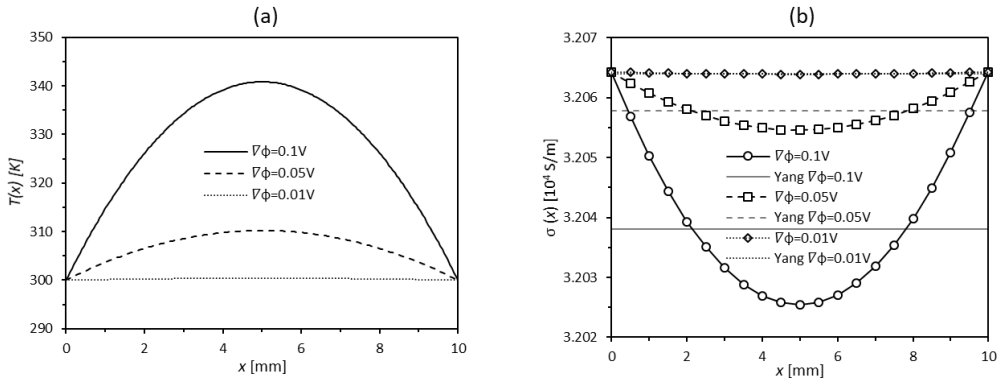

Figure 2.2. The distributions of (a) temperature, (b) effective electric conductivity defined by both ways in thermoelectric composite under an imposed potential difference of $\phi(0) = 0V$ and $\phi(L) = 0.1, 0.05, 0.01V$ with $T(0) = T(L) = 300K$ and $f = 0.4$.

Although the effective electric conductivity is a function of temperature, it does not change significantly as temperature changes. It only drops 2.2% as the temperature rises from 300K to 900K. Thus, the behavior of a thermoelectric composite material can be approximated by a single-phase material which has properties equal to the average effective properties that the composite has. If we consider either a temperature difference or an electric potential difference is imposed, the corresponding distributions of temperature, electric potential, and heat flux can be shown in Figure 2.3 and 2.4. It is clear that the field distributions of a thermoelectric composite and its single-phase equivalent are almost identical.

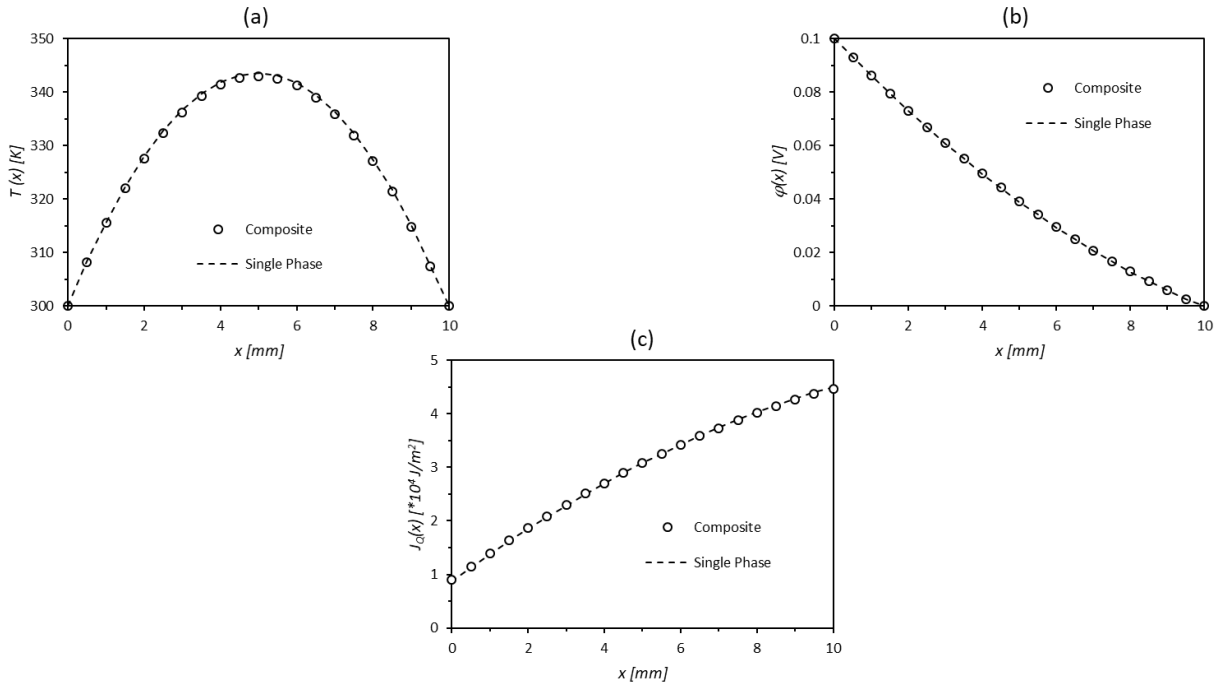

Figure 2.3. The distributions of (a) temperature, (b) electric potential, and (c) heat flux in a thermoelectric composite and its corresponding homogeneous material under the same imposed electric potential difference of $\phi(0) = 0.1V$ and $\phi(L) = 0V$, with $T(0) = T(L) = 300K$ and $f = 0.5$.

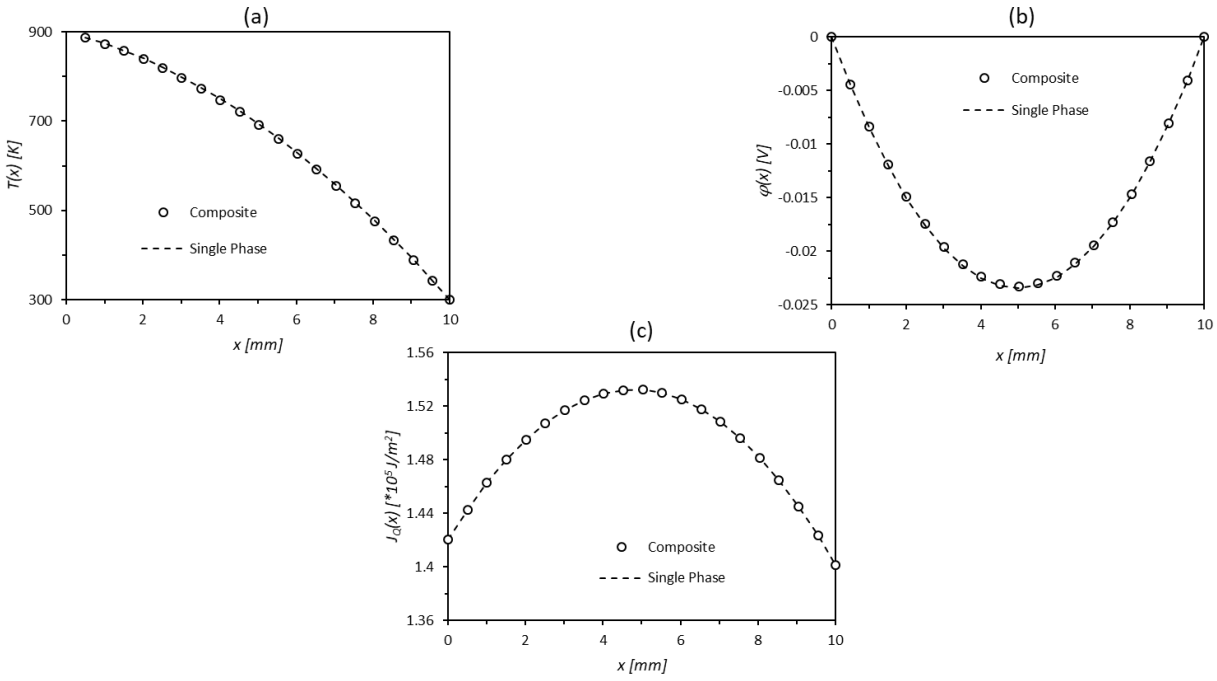

Figure 2.4. The distributions of (a) temperature, (b) electric potential, and (c) heat flux in a thermoelectric composite and its corresponding homogeneous material under the same imposed electric potential difference of $T(0) = 900K$ and $T(L) = 300K$, with $\phi(0) = \phi(L) = 0V$ and $f = 0.5$.

This set of results suggests that the optimized conversion efficiency of the composite can be predicted by equation (1.18), the classical formula relating conversion efficiency to ZT, with its average thermoelectric properties. We calculated the optimized conversion efficiency of the composite with respect to the volume fraction of Bi_2Te_3 by both methods, finding optimized efficiency numerically with equation (2.17) and using the classical equation (1.18), with $T(0) = 900K$ and $T(L) = 300K$. The results are shown in Figure 2.5. There is a good agreement between directly optimized value and the results converted from effective figures of merit, and we can say that the effective figure of merit is correlated with the optimized conversion efficiency.

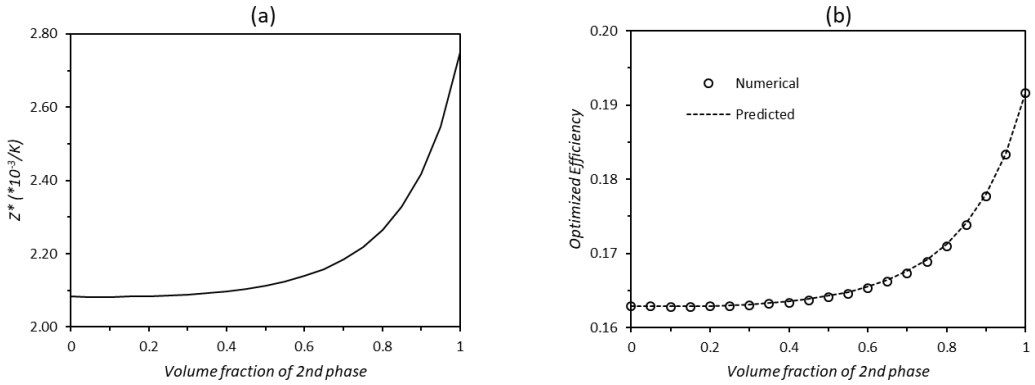

Figure 2.5. (a) Thermoelectric figure of merit and (b) conversion efficiencies of composite with respect to volume fraction calculated numerically and predicted by the classical equation.

2.6.2 *Boundedness of Thermoelectric Figure of Merit*

To show the idea that the figure of merit and the optimized conversion efficiency of a composite can be lower than both its constituents, we consider a periodic thermoelectric composite consisting of Bi_2Te_3 and a fictitious material with its thermoelectric properties listed in Table 2.2 and the volume fraction of Bi_2Te_3 being f. Using this fictitious material as the second phase in the composite, we make $\kappa_r \neq \sigma_r$ and assign a value for α_r such that it satisfies equation (2.27), which is required to have lower figure merit. Figure (2.6) shows clearly that both the figure of merit and the optimized conversion efficiency of a composite can be lower than both its constituents.

Table 2.2. Thermoelectric properties of a fictitious material

$\alpha(\times 10\text{^} - 6V/K)$	$\sigma(\times 10^3 S/m)$	$\kappa(W/m/K)$
300	22	0.8

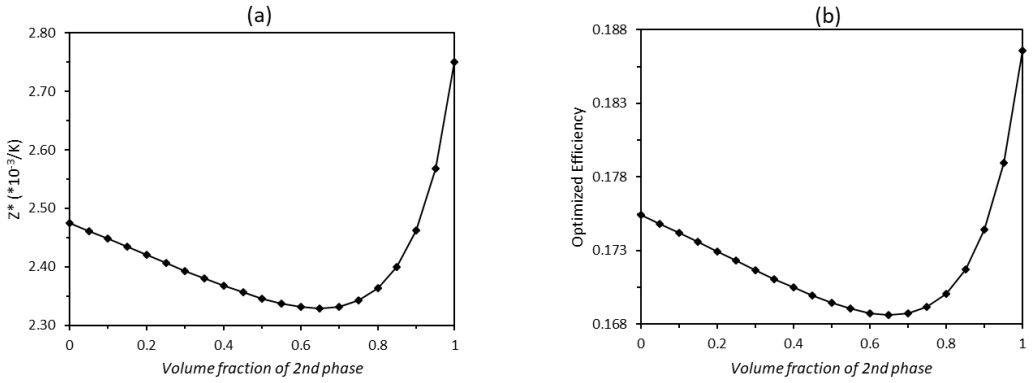

Figure 2.6. (a) Thermoelectric figure of merit, and (b) conversion efficiencies of composite with respect to the volume fraction of the second phase.

2.6.3 *Boundedness of Thermoelectric Power Factor*

Figure 2.7 shows how much the thermoelectric power factor can be enhanced under the sufficient conditions for power factor enhancement that we concluded in Section 2.5. Each point in this figure denotes the maximum power factor (with the optimized volume fraction being used) for specific values of α_r, κ_r, and σ_r. This figure shows us that we can significantly enhance the power factor by mixing a high quality thermoelectric material with a good thermal and electric conductor.

Here we first consider the power factor and figure of merit for composites made of $CoSb_3$ and metal Ni. $CoSb_3$ is a very good thermoelectric material with high thermoelectric power factor of $PF_1 = 0.0014\, J/(msK^2)$ at $T = 300K$. Figure 2.8 shows the maximal enhancement of effective power factor $(PF_e)/\,(PF_1\,) \cong 3.3$, at $f \cong 0.9$, giving about 55% of the value of Z1. In the same figure we also show that the effective figure of merit Z_e for this composite never exceeds the figure of merit for CoSb3, which is consistent with our earlier conclusion in Section 2.4.

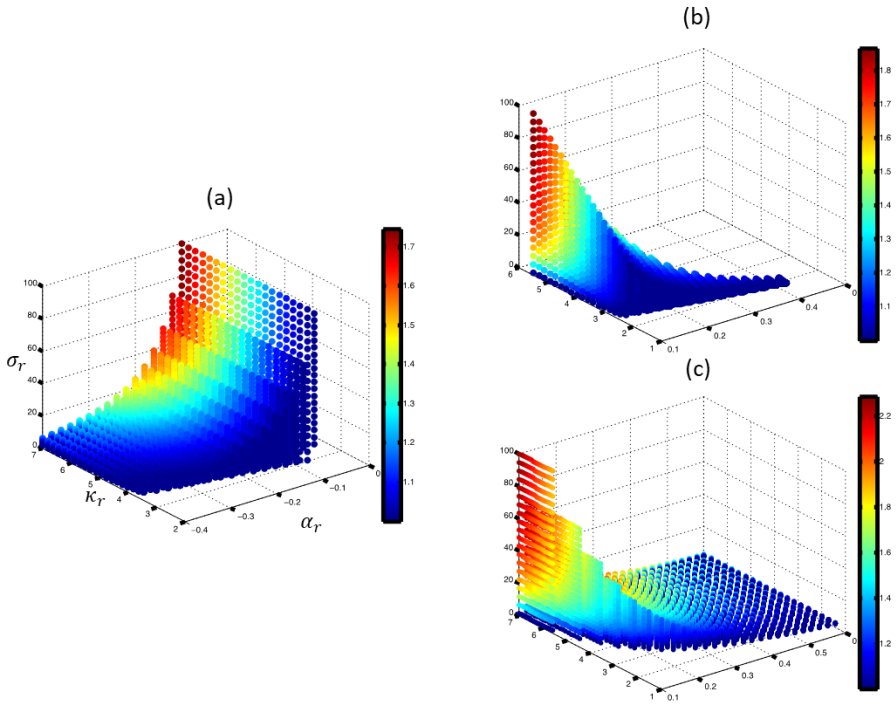

Figure 2.7. The enhanced thermoelectric power factor under the sufficient conditions by (a) equation (2.40), (b) equation (2.38), and (c) equation (2.39).

We, then, consider a more extreme case of a medium composed of $BiSbTe$ and Al that leads to $\sigma_r = 285$ and $\kappa_r = 214$. The high parameter ratio results in a sharp peak of $(PF_e)/(PF_1) \cong 34.6$. However, such a composite still keeps about 50% of the value of effective figure of merit as compared to Z_1, as shown in Figure 2.9

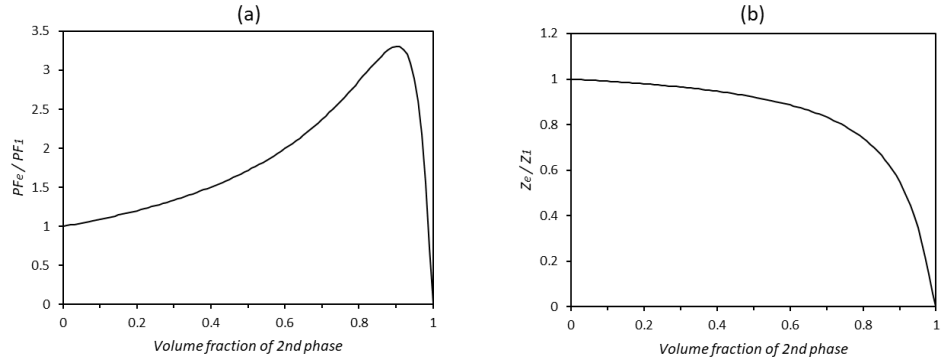

Figure 2.8. (a) Thermoelectric power factor PF_e/PF_1 and (b) figure of merit of the composite $CoSb_3 - Ni$.

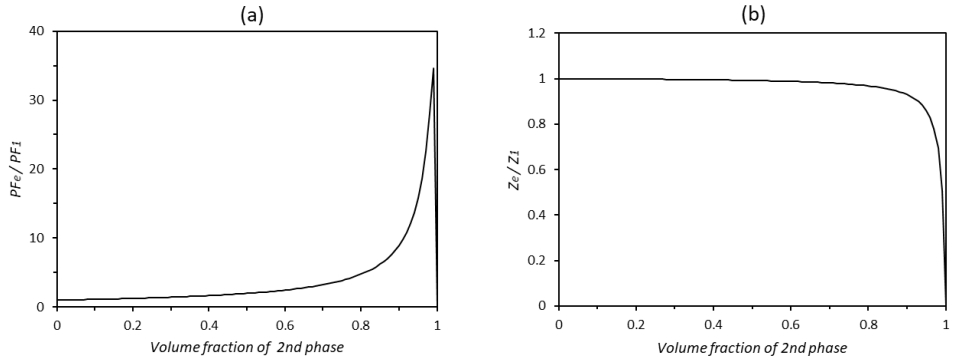

Figure 2.9. (a) Thermoelectric power factor PF_e/PF_1 and (b) figure of merit of the composite $BiSbTe - Al$.

2.7 SUMMARY

In this chapter, we defined a new set of effective properties for the periodic layered composite which does correlate with its thermoelectric performance. Then we proved that the effective figure of merit of the composite could not exceed both of its constituents, but the effective power factor could be greatly enhanced. In other words, even though the maximum conversion efficiency cannot be improved, the maximum power output can be enhanced. This becomes especially valuable when designing a thermoelectric device which will be used in a space restricted condition. This set of effective properties can serve as a simple tool to find the balance between enhancing power output and keeping conversion efficiency in thermoelectric device design.

Chapter 3. FUNCTIONALLY GRADED THERMOELECTRIC MATIERAL

3.1 INTRODUCTORY REMARKS

Our analysis in the previous chapter shows that the figure of merit of a thermoelectric composite with periodic layered microstructure cannot exceed both of its constituents. But the figure of merit is not the only factor that decides the conversion efficiency of a thermoelectric device. While the figure of merit decides the maximum efficiency, the material does not reach its maximum efficiency unless it is imposed with its optimal current for given temperatures. These bring in the concept of compatibility factor $s = \sqrt{1+ZT}/(\alpha T)$, a material property which describes the optimal condition for power generation. The relative current density $u = \frac{J}{\kappa \nabla T}$ equals to the compatibility only at some point in the medium and only if that part of the medium can reach its optimal efficiency. In homogeneous material, this match only happens once; only one point in the material works at its optimal condition. Now, we consider a functionally graded material constituted by two different materials, as schematically shown in Figure 3.1, in which each has a different compatibility factor. Since we developed the equations to predict the effective properties of a layered composite with specific volume fraction, we can tailor the volume fraction over the material so that the optimality can be realized everywhere, and possibly reach a higher overall conversion efficiency.

In the following section, we briefly describe the 1D model that we used to calculate the efficiency of a thermoelectric element. Then, we propose a procedure that helps us find the optimal design in Section 3. Numerical results and discussions are presented in Section 4. In Section 5, the summary for this chapter is provided.

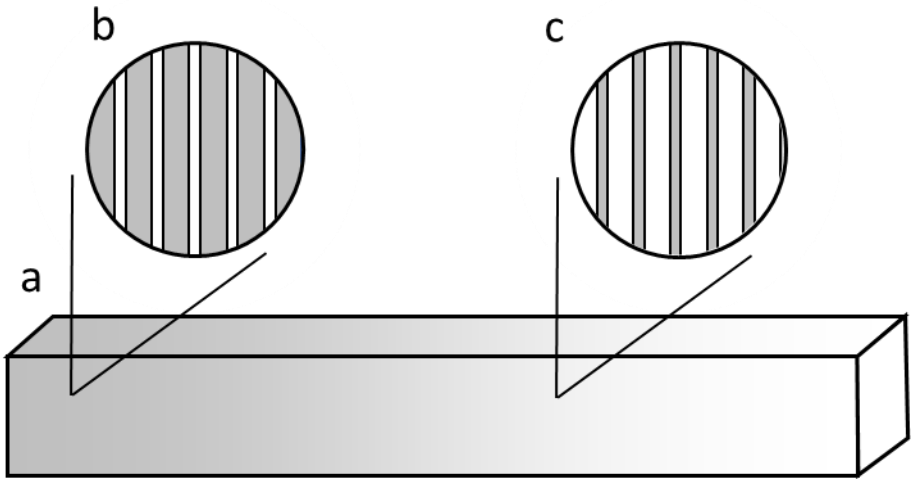

Figure 3.1. Schematics of functionally graded material; (a) macroscopic scale; (b) mesoscopic scale, with the lower volume fraction of 2nd phase; (c) mesoscopic scales, with the higher volume fraction of 2nd phase.

3.2 Reduced Current and Compatibility

The 1D model is described in detail by Snyder[82] and it takes into account all thermoelectric effects (the Seebeck, Peltier, and Thomson effects), Joule heating, heat conduction and the temperature dependence of all the thermoelectric material properties. Here, we do not consider heat losses, thermal and electrical contact resistances and only report the efficiency under the optimal condition. The 1D model defines and uses intrinsic variables that are independent on the system size. The new variable, reduced current density $u = J/\kappa\nabla T$, is defined as the ratio between the current density (J) and the heat flux by conduction. The reduced current density is independent of both the length and cross-sectional area of the element, and is only a function of the material properties and the temperature along the element. Once u is defined at a point, the value of u at any temperature along the element is determined by the differential equation

$$\frac{du}{dT} = u^2 T \frac{d\alpha}{dT} + u^3 \rho\kappa, \tag{3.1}$$

where ρ is the electrical resistivity. The properties in the model are related to the temperature along the element rather than a spatial coordinate x. Therefore we do not need to worry about the temperature distribution. This model thus helps us avoid the complex numerical methods used to predict the performance, and serves as a perfect tool for our purpose.

The efficiency along the infinitesimal distance dx can also be rewritten as a function of the material properties, temperature and reduced current density as

$$\eta = \frac{dT}{T}\frac{u(\alpha - u\rho\kappa)}{u\alpha + \frac{1}{T}}, \tag{3.2}$$

where the first term is the infinitesimal Carnot efficiency, and the second term is called reduced efficiency. It is clear that the reduced efficiency is a function of u, and only one value of u gives the largest reduced efficiency, which we refer to as the thermoelectric compatibility factor s:

$$s = \frac{\sqrt{1+ZT}-1}{\alpha T}. \tag{3.3}$$

This largest reduced efficiency η_r $(u = s)$ is given by

$$\eta_{rmax} = \frac{\sqrt{1+ZT}-1}{\sqrt{1+ZT}+1} \tag{3.4}$$

Within each of these infinitesimal steps, the temperature can be seen as evenly distributed. Thus, the effective properties in each section can be calculated by the equations we developed in the previous chapter. From the reduced current densities evaluated at the cold and hot sides, $u_c = u(T_c)$ and $u_h = u(T_h)$, the efficiency of a TE element can be found to be

$$\eta = 1 - \frac{\alpha_c T_c + \frac{1}{u_c}}{\alpha_h T_h + \frac{1}{u_h}}. \tag{3.5}$$

3.3 OPTIMIZATION

Here we propose a procedure to find the best composition for a specific temperature range:

1. We set the desired temperature range, that is, the temperature values at the cold and hot ends, and choose an end as our starting point, either hot end or cold end;
2. We assign an initial u for a certain material at the starting point. We choose the material with the highest figure of merit among the materials of our consideration;
3. While proceeding from the starting point to the other end, for every ΔT we calculate u, s, reduced efficiency, and choose a material or a combination of two materials that best matches one of our criteria;
4. Using equation (3.5), the efficiency of a TE element can be calculated. The maximum efficiency can be found by varying the initial u conditions and repeating steps (2) ~ (4).

In this study, we try three different local criteria for maximizing efficiency: best match of u and s, highest figure of merit, and highest reduced efficiency, and the results will be shown in the next section. The effective properties of composite material are calculated by the equations that we derived in the previous chapter. For the computation of u, the differential equation can be approximated by combining the zero Thomson effect ($d\alpha/dT = 0$) solution with the zero resistance ($\rho\kappa = 0$) soution:

$$\frac{1}{u_n} = \frac{1}{u_{n-1}}\sqrt{1 - 2u_{n-1}^2\overline{\rho\kappa}\Delta T} - \bar{T}\Delta\alpha. \tag{3.6}$$

where $\Delta\alpha = \alpha(T_n) - \alpha(T_{n-1})$ and $\overline{\rho\kappa}$ denotes the average of $\rho\kappa$ between T_n and T_{n-1}.

3.4 NUMERICAL RESULTS AND DISCUSSIONS

3.4.1 *Two Materials with The Same Figure of Merit*

To examine if the composite can have higher conversion efficiency than both of its constituents, we calculate efficiency of a functionally graded material, FGM, consisting of Bi_2Te_3 and a fictitious material, with $T_c = 300K$ and $T_h = 500K$. This fictitious material has the same figure of merit (but different compatibility) as Bi_2Te_3. The material constants used in the calculation are listed in Table 3.1. The reason why we choose these numbers is because we are trying not to sacrifice too much of the figure of merit, but at the same time we can tune the compatibility factor in every location.

Figure 3.2(a) and (b) show that these two materials have different compatibilities and different optimal reduced current densities. It is also seen that the reduced current density and compatibility only intersect once in each material. On the other hand, in a functionally graded material u and s can perfectly match each other, as shown in Figure 3.2(c). However, there is almost no improvement from this FGM. The optimal efficiencies of FGM and pure Bi_2Te_3 are 8.783% and 8.769% respectively.

Table 3.1. Thermoelectric properties of a fictitious material

Material	$\alpha(\times 10^{-6}V/K)$	$\sigma(\times 10^{3}S/m)$	$\kappa(W/m/K)$	$Z\ (\times 10^{-3}K^{-1})$
Bi_2Te_3	200	110	1.6	2.75
Fictitious	170	110	1.225	2.75

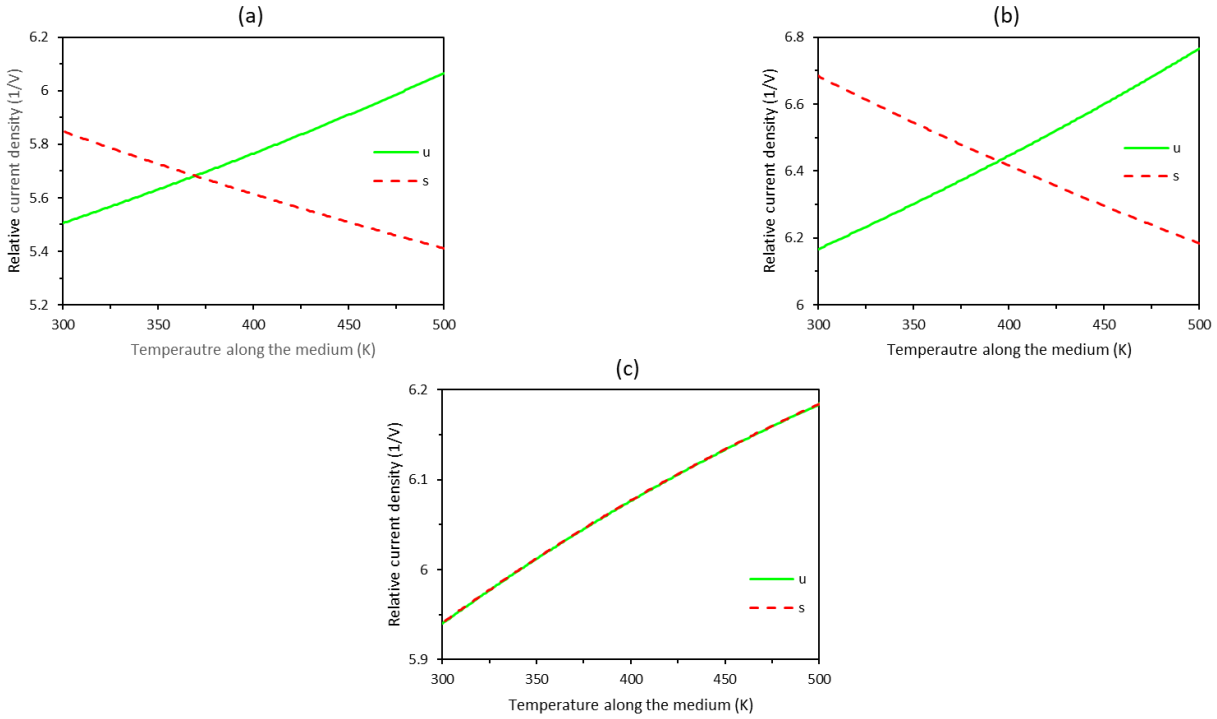

Figure 3.2. Reduced current density and compatibility with respect to temperature between cold side and hot side for (a) Bi_2Te_3, (b) the fictitious material, and (c) functionally graded material in the temperature range 300-500K.

The reason why there is no improvement is because the Seebeck coefficients of the two materials must be different so as to make compatibility factor, $s = \frac{\sqrt{1+ZT}}{\alpha T}$, tunable while keeping the ZT at the same time. Thus, the ratio of the thermal conductivity of the two materials must be different from the ratio of the electric conductivity of the two. These happen to be the condition that makes the effective figure of merit lower than both its constituents, as shown in Figure 3.3. Although, the optimal condition is met everywhere and the FGM has higher values of reduced efficiency at two ends, the sacrifice of the figure of merit and the reduced efficiency in the middle makes the FGM no better case, as seen in Figure 3.4.

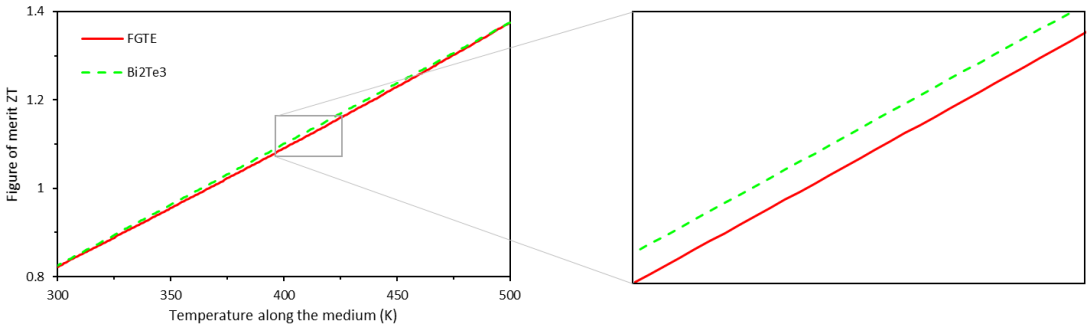

Figure 3.3. The figure of merit with respect to temperature for functionally graded material and pure Bi_2Te_3 in the temperature range 300-500K.

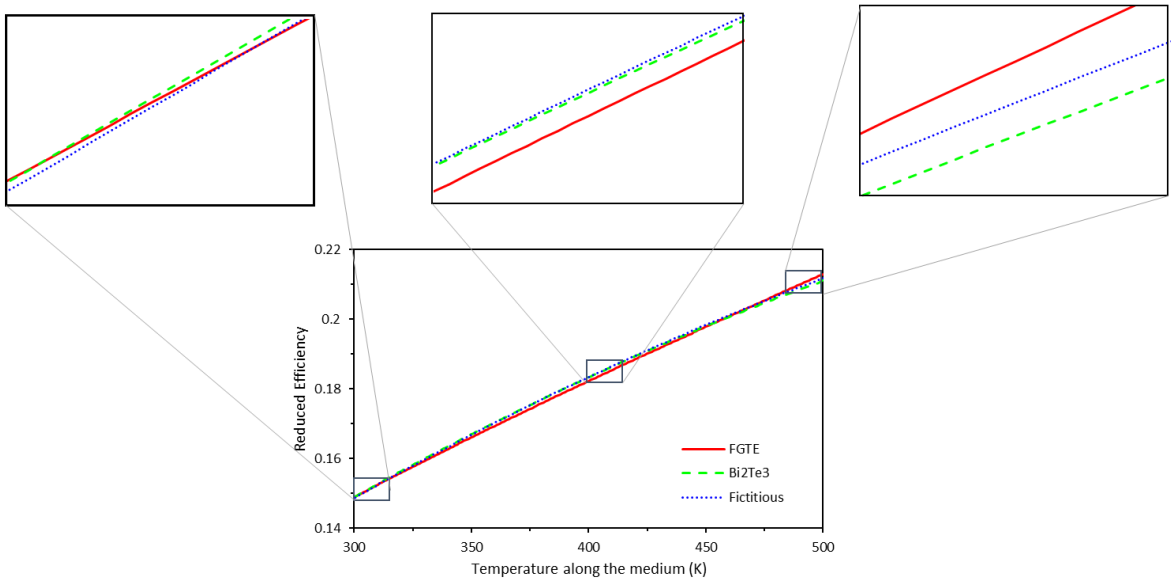

Figure 3.4. The reduced efficiency with respect to temperature for functionally graded material, pure Bi_2Te_3, and fictitious material in the temperature range 300-500K.

3.4.2 *Materials with Temperature Dependency*

To further extend our study, we consider the real state-of-the-art n- and p-type TE materials. All the thermoelectric properties are provided by Gerald Jeffrey Snyder, California Institute of Technology. Figure 3.5 shows the figure of merit ZT and the compatibility factors as functions of temperature for both p- and n-type materials.

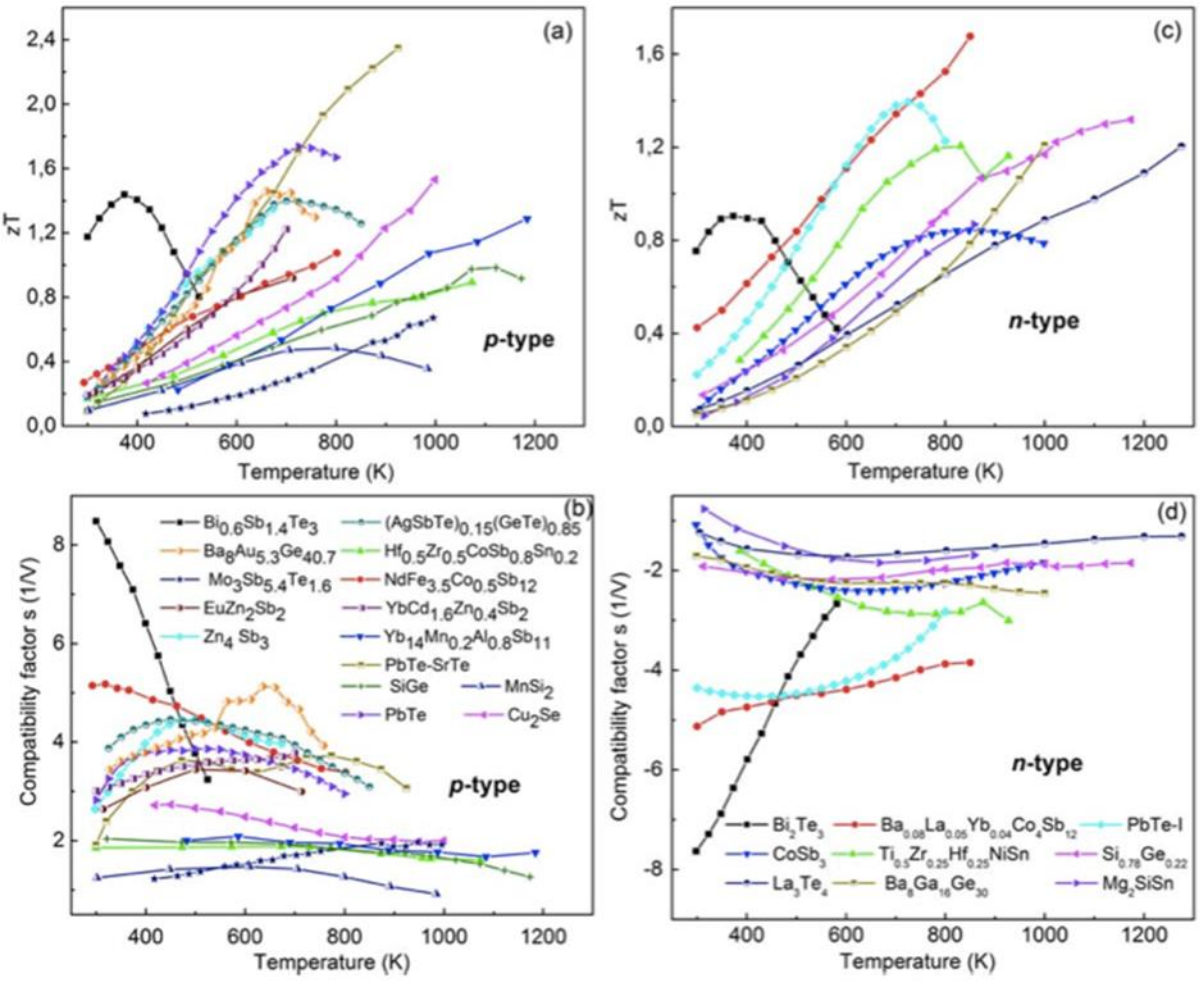

Figure 3.5. Figure of merit and compatibility factor of the state-of-the-art p- and n-type thermoelectric material. Material data is provided by Gerald Jeffrey Snyder, California Institute of Technology, USA[83].

Figure 3.6 demonstrates the optimized compositions of p-type materials with cold side temperature at $T_c = 300K$, and hot side temperature at $T_t = 1100K$. Here, we show 3 different compositions with 3 different settings. The first one is simply choosing the material with the highest ZT at each temperature. With this composition, the TE element has the optimal efficiency of 20.88%. As it is compared with the best case from the literature, where the highest efficiency, 19.99%, can be achieved by putting three materials, $Bi_{0.6}Sb_{1.4}Te_3$, $PbTe - SrTe$, and $SiGe$ in segment, 5% improvement is made. The second case is to choose the material that results in the highest reduced efficiency in each step while not allowing the mixing of the materials (i.e. only allowing the segmented design). This composition is very similar to the first one, and it only adds two more materials between 1000K and 1070K. Although these two materials do not have the highest figure of merit at the temperatures, they still help improve efficiency to 20.95%. The reason that the second composition has the higher efficiency can be seen in Figure 3.7, which shows the relative current density and compatibility factor with respect to temperature between cold side and hot side. These two materials help bring closer the gap between the relative current density and compatibility factor and improve the total efficiency. The last case uses the same criteria as the second case, and allows mixing the materials. There are mixtures of $PbTe$ and $PbTe - SrTe$, and $Mo_3Sb_{5.4}Te_{1.6}$ is introduced to be mixed with Cu_2Se. The relative current density and compatibility factor are brought closer in this case, and the higher efficiency, 21.01%, is achieved. Figure 3.8 shows the absolute value of the difference between u and s. It is worth noting that the gaps are not only closed at the locations where the additional materials are introduced, but also at most part of the element.

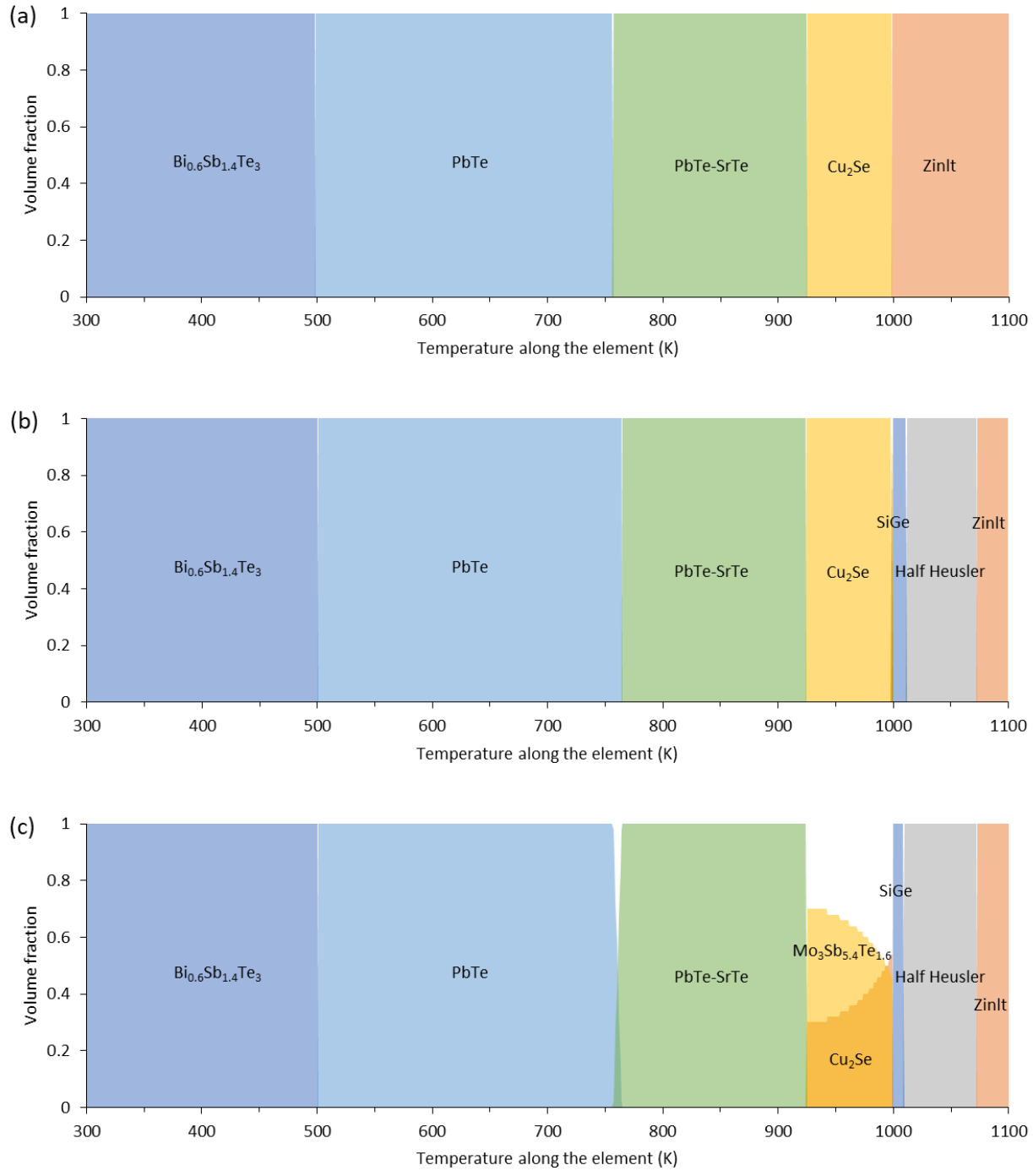

Figure 3.6. Compositions are optimized with the criteria of choosing (a) the material that has the highest *ZT*, (b) the material that results in the highest reduced efficiency, and (c) the material or combination of material that results in the highest reduced efficiency.

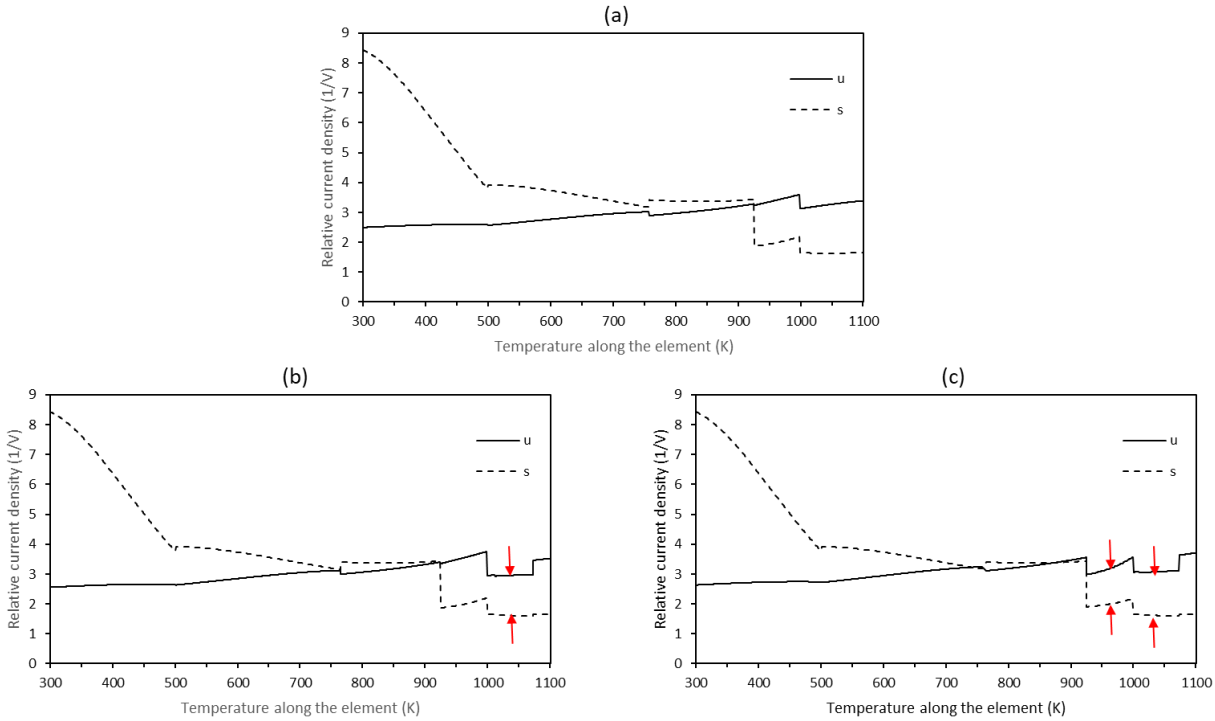

Figure 3.7. Compositions are optimized with the criteria of choosing (a) the material that has the highest ZT, (b) the material that results in the highest reduced efficiency, and (c) the material or combination of material that results in the highest reduced efficiency.

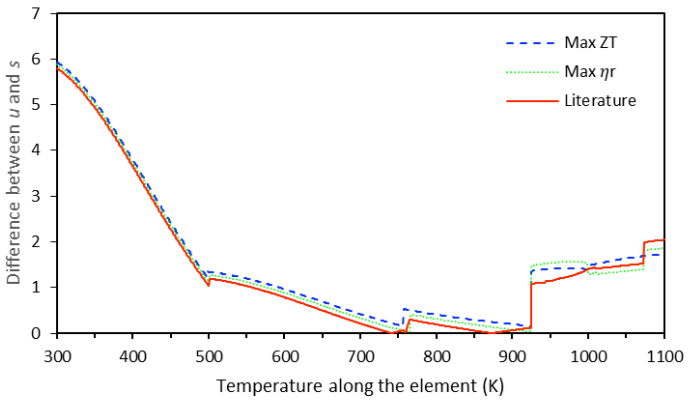

Figure 3.8. The absolute differences between u and s for the three different compositions optimized by three different criteria.

Table 3.2 summarizes the results, and it is worth noting that adding two more materials only improves the efficiency by about 1%, and the gain of efficiency with the other two cases is rather insignificant. The same conclusion is made while we carried out the same process on the n-type materials, where the results are summarized in Table 3.3. That is because the figure of merit has a higher impact on the efficiency than the matching of the compatibility factor. Figure 3.9 shows the relationship between the reduced current density and the reduced efficiency, and it is seen that the reduced efficiency does not change much while the relative current density is close to its compatibility factor. This explains the small improvement of trying to match reduced current density to the compatibility factor.

Table 3.2. The optimal efficiency and the number of materials used in the p-type TE element

	Number of materials	Optimal efficiency
Literature	3	19.99%
Maximum ZT	5	20.88%
Maximum reduced efficiency _ segmented	7	20.95%
Maximum reduced efficiency _ mixture	8	21.01%

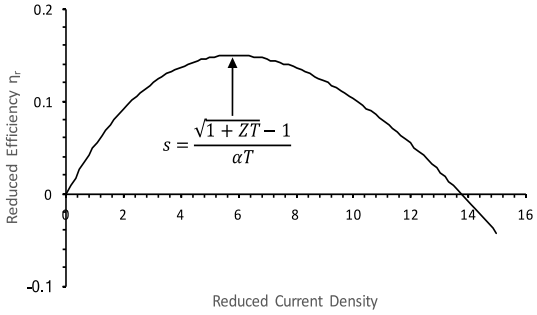

Figure 3.9. Variation of reduced efficiency with reduced current density for Bi_2Te_3.

Table 3.3. The optimal efficiency and the number of materials used in the n-type TE element

	Number of materials	Optimal efficiency
Literature	3	16.38%
Maximum ZT	8	17.23%
Maximum reduced efficiency _ segmented	7	17.99%
Maximum reduced efficiency _ mixture	7	17.99%

3.5 SUMMARY

In this chapter, we show that the efficiency gain from the layered microstructure is insignificant. The tunable compatibility factor makes it possible to optimize the relative current density everywhere, which, however, comes with the sacrifice of the figure of merit as a drawback.

Chapter 4. ASYMPTOTIC HOMOGENIZATION OF 2D THERMOELECTRIC COMPOSITES

4.1 INTRODUCTORY REMARKS

In foregoing chapters, we analyzed 1D periodic and functionally graded composites with layered microstructure. It was proved that not much improvement could be made under that scope. In this chapter, we study the thermoelectric composite with 2D unit cell configuration, which introduces more adjustable parameters, and better opportunity to make improvement. The asymptotic analysis on 2D thermoelectric composite was done by Yang, and he derived the 2D homogenized thermoelectric governing equation for the distributions of macroscopic temperature and electric potential. We extended his work and analyzed the effective behavior of the composite. In our analysis we discovered some limitations of this model.

In a very similar way as we did in the second chapter, we will give the general idea and results of Yang's work in Section 4.2. In Section 4.3, we do the field analysis and define the effective properties. Then we present the numerical results in Section 4.4. Along with the results, we discuss the limitations and uncertainties of this method. The summary is provided in the last section.

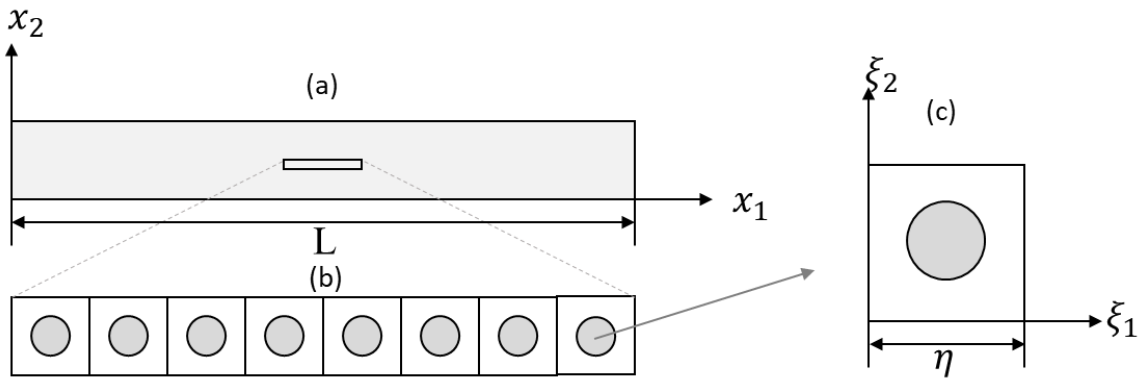

Figure 4.1. Schematics of a 2D composite in (a) macroscopic, (b) mesoscopic, and (c) microscopic scales.

4.2 TWO-DIMENSIONAL ASYMPTOTIC ANALYSIS

4.2.1 *Asymptotic Analysis*

Details of the asymptotic analysis are first described by Yang[81]. In his analysis, he applied the asymptotic homogenization method on a 2D/3D thermoelectric composite and established the unit cell problems for both general and pseudo 2D/3D cases. For the purpose of analyzing the performance of the thermoelectric composite in power generation, we only consider the pseudo 2D case. In this case, the macroscopic field variables only vary along x_1 (but not x_2), and no energy or charge carrier exchange between cells in the x_2 direction.

Now, we consider a composite comprises two distinct phases with periodic distribution, as schematically shown in Figure 4.1. For such a composite, two different length scales can be identified. One is L, the macroscopic length of the composite associated with the macroscopic coordinate x_i. The other is η, the characteristic length of the composite unit cell, for which a microscopic coordinate $\xi_i = x_i / \eta$ can be introduced. As we know that, the material properties $\alpha(\xi_i)$, $\sigma(\xi_i)$, and $\kappa(\xi_i)$, vary fast on the microscopic scale periodically. Thus, the field variables such as $T(x_1, \xi_i)$, $\varphi(x_1, \xi_i)$ vary both fast on microscopic scale and slowly on macroscopic scale. The goal of this analysis is to deduce the governing equations which govern the macroscopic variations of these fields where the fast fluctuations is are averaged out.

Being different from the 1D case, the current density J and energy flux J_U in the 2D case are no longer constant. Therefore, the governing equations cannot be deduced by simply inserting the expended field functions

$$T(x_1, \xi_i) = T^{(0)}(x_1, \xi_i) + \eta T^{(1)}(x_1, \xi_i) + \eta^2 T^{(2)}(x_1, \xi_i) + \cdots, \tag{4.1}$$

$$\phi(x_1, \xi_i) = \phi^{(0)}(x_1, \xi_i) + \eta \phi^{(1)}(x_1, \xi_i) + \eta^2 \phi^{(2)}(x_1, \xi_i) + \cdots \tag{4.2}$$

into the thermoelectric transport equations

$$-J = \sigma\nabla\phi + \sigma\alpha\nabla T, \tag{4.3}$$

$$J_U = -(\sigma\phi + \sigma\alpha T)\nabla\phi - (\kappa + \sigma\alpha\phi + \sigma\alpha^2 T)\nabla T. \tag{4.4}$$

However, this way of insertion still gives us the first piece of information that $T^{(0)} = T^{(0)}(x_1)$ and $\phi^{(0)} = \phi^{(0)}(x_1)$, which do not depend on ξ_i, that is, namely that $T^{(0)}$ and $\phi^{(0)}$ are the macroscopy field distributions (which are of particular interest to us). It also shows that the governing equations of this composite can be written as

$$-J = \sigma\left(\frac{\partial\phi^{(0)}}{\partial x_1} + \frac{\partial\phi^{(1)}}{\partial\xi_1}\right) + \sigma\alpha\left(\frac{\partial T^{(0)}}{\partial x_1} + \frac{\partial T^{(1)}}{\partial\xi_1}\right), \tag{4.5}$$

$$\begin{aligned} J_U = &-\left(\sigma\phi^{(0)} + \sigma\alpha T^{(0)}\right)\cdot\left(\frac{\partial\phi^{(0)}}{\partial x_1} + \frac{\partial\phi^{(1)}}{\partial\xi_1}\right) \\ &-\left(\kappa + \sigma\alpha\phi^{(0)} + \sigma\alpha^2 T^{(0)}\right)\cdot\left(\frac{\partial T^{(0)}}{\partial x_1} + \frac{\partial T^{(1)}}{\partial\xi_1}\right), \end{aligned} \tag{4.6}$$

and the macroscopy governing equations are the averaged values of these two equations evaluated on a unit cell, giving

$$\langle -J(x_1,\xi_1,\xi_2)\rangle = -\int_0^1\int_0^1\int_0^1 J(x_1,\xi_1,\xi_2)\,d\xi_1 d\xi_2 \tag{4.7}$$

$$\langle -J_U(x_1,\xi_1,\xi_2)\rangle = -\int_0^1\int_0^1\int_0^1 J_U(x_1,\xi_1,\xi_2)\,d\xi_1 d\xi_2. \tag{4.8}$$

The difficulty of this analysis is how to solve $T^{(1)}$ and $\phi^{(1)}$. Once the $T^{(1)}$ and $\phi^{(1)}$ are solved, we have the macroscopy governing equation, and the effective behavior of the composite can be examined. Yang found the solutions of $T^{(1)}$ and $\phi^{(1)}$ by first inserting the expanded field functions equations (4.1) and (4.2) into

$$\nabla\cdot J = 0, \tag{4.9}$$

$$\nabla\cdot J_U = 0, \tag{4.10}$$

to get additional equations, and guessed the structure of $T^{(1)}$ and $\phi^{(1)}$ and substituted them into these equations. He hypothesized that

$$T^{(1)} = N^{(1)}(\xi)\frac{1}{T^{(0)}-X}\frac{\partial \phi}{\partial x} + N^{(2)}(\xi)\frac{1}{T^{(0)}-X}\frac{\partial T}{\partial x} + N^{(3)}(\xi)\frac{\partial \phi}{\partial x} + N^{(4)}(\xi)\frac{\partial T}{\partial x}, \quad (4.11)$$

$$\phi^{(1)} = M^{(1)}(\xi)\frac{1}{T^{(0)}-X}\frac{\partial \phi}{\partial x} + M^{(2)}(\xi)\frac{1}{T^{(0)}-X}\frac{\partial T}{\partial x} + M^{(3)}(\xi)\frac{\partial \phi}{\partial x} + M^{(4)}(\xi)\frac{\partial T}{\partial x}, \quad (4.12)$$

where $N^{(1)}(\xi)$, $N^{(2)}(\xi)$, $N^{(3)}(\xi)$, $N^{(4)}(\xi)$, $M^{(1)}(\xi)$, $M^{(2)}(\xi)$, $M^{(3)}(\xi)$, $M^{(4)}(\xi)$ are unknown variables of ξ, and X is a constant that needs to be determined. By doing so, eight governing equations for the unit cell problem are derived. Using these governing equations and together with additional interface conditions and boundary conditions, which are established by the continuity and periodic conditions, $N^{(1)}\sim N^{(4)}$, $M^{(1)}\sim M^{(4)}$ can be solved by finite element method and thus give us the expression for $T^{(1)}$ and $\phi^{(1)}$.

By substituting them into equations (4.7) and (4.8) the equations of the macroscopic current density and energy flux are derived as

$$\langle -J \rangle = \frac{G^{(1)}+G^{(3)}\tilde{T}^{(0)}}{\tilde{T}^{(0)}}\frac{d\phi^{(0)}}{dx_1} + \frac{G^{(2)}+G^{(4)}\tilde{T}^{(0)}}{\tilde{T}^{(0)}}\frac{dT^{(0)}}{dx_1}, \quad (4.13)$$

$$\begin{aligned}\langle J_U \rangle = {} & \left(H^{(3)}\tilde{T}^{(0)} + G^{(3)}\phi^{(0)} + H^{(1)} + XH^{(3)} + K^{(3)}\right)\frac{d\phi^{(0)}}{dx_1} \\ & + \frac{G^{(1)}\phi^{(0)}+XH^{(1)}+K^{(1)}}{\tilde{T}^{(0)}}\frac{d\phi^{(0)}}{dx_1} \\ & + \left(H^{(4)}\tilde{T}^{(0)} + G^{(4)}\phi^{(0)} + H^{(2)} + XH^{(4)} + K^{(4)}\right)\frac{d\tilde{T}^{(0)}}{dx_1} \\ & + \frac{G^{(2)}\phi^{(0)}+XH^{(2)}+K^{(2)}}{\tilde{T}^{(0)}}\frac{d\tilde{T}^{(0)}}{dx_1}, \end{aligned} \quad (4.14)$$

with effective properties

$$
\begin{aligned}
G^{(1)} &= \left\langle \sigma \frac{\partial N^{(1)}}{\partial \xi_1} + \sigma\alpha \frac{\partial M^{(1)}}{\partial \xi_1} \right\rangle, \\
G^{(2)} &= \left\langle \sigma \frac{\partial N^{(2)}}{\partial \xi_1} + \sigma\alpha \frac{\partial M^{(2)}}{\partial \xi_1} \right\rangle, \\
G^{(3)} &= \left\langle \sigma \frac{\partial (N^{(3)}+\xi_1)}{\partial \xi_1} + \sigma\alpha \frac{\partial M^{(3)}}{\partial \xi_1} \right\rangle, \\
G^{(4)} &= \left\langle \sigma \frac{\partial N^{(4)}}{\partial \xi_1} + \sigma\alpha \frac{\partial (M^{(4)}+\xi_1)}{\partial \xi_1} \right\rangle, \\
H^{(1)} &= \left\langle \sigma\alpha \frac{\partial N^{(1)}}{\partial \xi_1} + \sigma\alpha^2 \frac{\partial M^{(1)}}{\partial \xi_1} \right\rangle, \\
H^{(2)} &= \left\langle \sigma\alpha \frac{\partial N^{(2)}}{\partial \xi_1} + \sigma\alpha^2 \frac{\partial M^{(2)}}{\partial \xi_1} \right\rangle, \\
H^{(3)} &= \left\langle \sigma\alpha \frac{\partial (N^{(3)}+\xi_1)}{\partial \xi_1} + \sigma\alpha^2 \frac{\partial M^{(3)}}{\partial \xi_1} \right\rangle, \\
H^{(4)} &= \left\langle \sigma\alpha \frac{\partial N^{(4)}}{\partial \xi_1} + \sigma\alpha^2 \frac{\partial (M^{(4)}+\xi_1)}{\partial \xi_1} \right\rangle, \\
K^{(1)} &= \left\langle \kappa \frac{\partial M^{(1)}}{\partial \xi_1} \right\rangle, \\
K^{(2)} &= \left\langle \kappa \frac{\partial M^{(2)}}{\partial \xi_1} \right\rangle, \\
K^{(3)} &= \left\langle \kappa \frac{\partial M^{(3)}}{\partial \xi_1} \right\rangle, \\
K^{(4)} &= \left\langle \kappa \frac{\partial (M^{(4)}+\xi_1)}{\partial \xi_1} \right\rangle.
\end{aligned}
$$

4.2.2 *Solving the Unit Cell Problem*

4.2.3 *Two Sub-problems*

The unit cell problem formed in the last sub-section is difficult to solve analytically due to its complex 2D structure. Therefore, a finite element method is applied to find the solutions numerically. This unit cell problem can actually be formed into two sub-problems that can be solved separately. The first sub-problem is characterized as

$$
\begin{cases}
\frac{\partial}{\partial \xi_i}\left(A \frac{\partial u}{\partial \xi_i}\right) = 0, \ \xi \in \Omega, \\
[u]|_{\Sigma} = 0, \ \left[A \frac{\partial u}{\partial \xi_i}\right]|_{\Sigma} = 0, \\
u(0, \xi_2) = [0\ 0\ 0\ 0]^T, \\
u(1, \xi_2) = [0\ 0\ 1\ 0]^T, \\
u(\xi_1, 0) = u(\xi_1, 1) = [0\ 0\ \xi_1\ 0]^T
\end{cases}
\tag{4.15}
$$

where $[.]|_{\Sigma}$ denotes the jump of values across the interface Σ and

$$A = \begin{bmatrix} \sigma & \sigma\alpha & 0 & 0 \\ X\sigma\alpha & X\sigma\alpha^2 + \kappa & 0 & 0 \\ 0 & 0 & \sigma & \sigma\alpha \\ \sigma\alpha & \sigma\alpha^2 & 0 & \kappa \end{bmatrix}, u = \begin{bmatrix} N^{(1)} \\ M^{(1)} \\ \widetilde{N}^{(3)} + \xi_1 \\ M^{(3)} \end{bmatrix}. \tag{4.16}$$

The other sub-problem is characterized as

$$\begin{cases} \frac{\partial}{\partial \xi_i}\left(A \frac{\partial \tilde{u}}{\partial \xi_i}\right) = 0, \ \xi \in \Omega, \\ [\tilde{u}]|_{\Sigma} = 0, \ \left[A \frac{\partial u}{\partial \xi_i}\right]|_{\Sigma} = 0, \\ \tilde{u}(0, \xi_2) = [0\ 0\ 0\ 0]^T, \\ \tilde{u}(1, \xi_2) = [0\ 0\ 0\ 1]^T, \\ \tilde{u}(\xi_1, 0) = \tilde{u}(\xi_1, 1) = [0\ 0\ 0\ \xi_1]^T, \end{cases} \tag{4.17}$$

where

$$\tilde{u} = \begin{bmatrix} N^{(2)} \\ M^{(2)} \\ \widetilde{N}^{(4)} \\ M^{(4)} + \xi_1 \end{bmatrix}. \tag{4.18}$$

4.2.4 *Finding X*

Before we can solve these two sub-problems, we need to find the unknown constant X first. By grouping $N^{(1)}$ and $M^{(1)}$ together and modifying matrix A provides we obtain the following problem that helps to find the value of the constant X.

$$\begin{cases} \frac{\partial}{\partial \xi_i}\left(A \frac{\partial \tilde{u}}{\partial \xi_i}\right) = 0, \ \xi \in \Omega, \\ [u]|_{\Sigma} = 0, \ \left[A \frac{\partial u}{\partial \xi_i}\right]|_{\Sigma} = 0, \\ u|_{\partial\Omega} = 0, \end{cases} \tag{4.19}$$

where

$$A = \begin{bmatrix} \sigma & \sigma\alpha \\ X\sigma\alpha & X\sigma\alpha^2 \end{bmatrix}, u = \begin{bmatrix} N^{(1)} \\ M^{(1)} \end{bmatrix}. \tag{4.20}$$

This problem must be incompletely defined or we would have $u = 0$, which is an impossible result. For this to be an incompletely defined problem the overall matrix K^a in $K^a u^a = 0$ has to be a singular matrix and

$$|K^a| = 0 \tag{4.21}$$

This equation can be written as

$$|K_1^a + XK_2^a| = 0, \tag{4.22}$$

which is equivalent to the generalized eigenvalue problem

$$K_1^a x = -XK_2^a x, \tag{4.23}$$

where K_1^a and K_2^a are matrices, $-X$ and x are respectively eigenvalue and eigenvector. Through solving this eigenvalue problem, we can find a number of possible X's that make this unit cell problem solvable.

4.2.5 *Solving Field Variables*

Up to this point, we have the value(s) of X such that the Finite Element method can be applied to the two sub-problems represented by equations (4.15) and (4.17). To make these problems complete, the equations for the interface condition are included, making these problems have more equations than variables. This over-determined system can be solved by the least least-square method. Since we have numbers of possible values of X from the last step, we need to plug each one of them back to the sub-problems and to solve them, and check which X results in the minimum residual value in the least-square method. The X that results in the minimum residual value is the one that we are looking for.

4.3 THE EFFECTIVE BEHAVIOR

4.3.1 *Macroscopic Field Analysis*

Since the equations that govern the distributions of macroscopic temperature and electric potential are highly nonlinear and coupled, it is very difficult to solve the field distribution analytically. Here we solve the coupling problem of temperature and electric potential with known boundary conditions iteratively. The solution procedure is first assuming the temperature distribution being linear across the TE element. This assumption is especially applicable in electric generation where very small current passes through the element. Second, we solve the electric potential distribution by a shooting method with

$$\phi_{xx}^{(0)} = \left(\frac{G^{(1)}}{\tilde{T}^{(0)2}}\tilde{T}_x^{(0)}\phi_x^{(0)} + \frac{G^{(2)}}{\tilde{T}^{(0)}}\tilde{T}_x{}^{(0)2} - G^{(4)}\tilde{T}_{xx}^{(0)}\right)/G^{(3)}, \tag{4.24}$$

which is the derivative of equation (4.13) with respect to x_1 and the subscript x denotes the partial derivatives that are being taken with respect to x_1, which make it more identifiable, wherein T is treated as a known variable from the last step. Third, using the result from the second step to solve the temperature distribution by another shooting method with

$$\begin{aligned}\tilde{T}_{xx}^{(0)} = \Bigg(&-\left(H^{(3)}\tilde{T}_x^{(0)} + G^{(3)}\phi_x^{(0)} + \frac{G^{(1)}\phi_x^{(0)}\tilde{T}^{(0)} - G^{(1)}\phi^{(0)}\tilde{T}_x^{(0)}}{\tilde{T}^{(0)2}}\right)\phi_x^{(0)} \\ &-\left(H^{(3)}\tilde{T}^{(0)} + G^{(3)}\phi^{(0)} + H^{(1)} + XH^{(3)} + K^{(3)} + \frac{G^{(1)}\phi^{(0)} + XH^{(1)} + K^{(1)}}{\tilde{T}^{(0)}}\right)\phi_{xx}^{(0)} \\ &-\left(H^{(4)}\tilde{T}_x^{(0)} + G^{(4)}\phi_x^{(0)} + \frac{G^{(2)}\phi_x^{(0)}\tilde{T}^{(0)} - G^{(2)}\phi^{(0)}\tilde{T}_x^{(0)}}{\tilde{T}^{(0)2}}\right)\tilde{T}_x^{(0)}\Bigg) \\ &/\left(H^{(4)}\tilde{T}^{(0)} + G^{(4)}\phi^{(0)} + H^{(2)} + XH^{(4)} + K^{(4)} + \frac{G^{(2)}\phi^{(0)} + XH^{(2)} + K^{(2)}}{\tilde{T}^{(0)}}\right),\end{aligned} \tag{4.25}$$

which is the derivative of equation (4.14) with respect to x_1. Finally, we repeat steps 2 and 3 until the solutions are converged.

4.3.2 *The Effective Properties and Conversion Efficiency*

All the effective thermoelectric properties are examined with the equivalency principle. Based on experience we have, we know that the effective properties of the composite can be temperature dependent even if the properties of its constituents are independent of temperature. Thus, all the effective properties needed to be defined under very limited conditions. When we examine the effective electric conductivity, we need to consider a boundary condition of very small electric potential difference being imposed with $\frac{dT}{dx_1} = 0$, and compare the current density between homogeneous thermoelectric and composite. The effective electric conductivity of the composite is given by

$$\sigma^*(\Delta\phi, \Delta T = 0) = \lim_{\Delta\phi \to 0} -\frac{J}{\Delta\phi/L}, \tag{4.26}$$

with the current density given by equation (4.13), resulting in

$$\sigma^* = \frac{G^{(1)} + G^{(3)}\tilde{T}}{\tilde{T}}. \tag{4.27}$$

As expected, the effective electric conductivity is a function of temperature. The effective Seebeck coefficient can be easily obtained by using the same equation, but with an imposed open-circuit boundary condition where $J = 0$, such that

$$\frac{d\phi}{dx_1} = -\frac{G^{(2)} + G^{(4)}\tilde{T}}{G^{(1)} + G^{(3)}\tilde{T}} \frac{dT}{dx_1}, \tag{4.28}$$

and

$$\alpha^* = -\frac{d\phi}{dT} = \frac{G^{(2)} + G^{(4)}\tilde{T}}{G^{(1)} + G^{(3)}\tilde{T}}. \tag{4.29}$$

To examine the effective thermal conductivity, we need to know the expression of the heat flux, which can be obtained from equation (4.14). Equation (4.14) can be rearranged as

$$-J_U = \left(H^{(3)}T + K^{(3)} + \frac{H^{(1)}T + K^{(1)}}{\tilde{T}}\right)\frac{d\phi}{dx_1} + \left(H^{(4)}T + K^{(4)} + \frac{H^{(2)}T + K^{(2)}}{\tilde{T}}\right)\frac{d\tilde{T}}{dx_1} \left(\frac{G^{(1)} + G^{(3)}\tilde{T}^{(0)}}{\tilde{T}}\frac{d\phi}{dx_1} + \frac{G^{(2)} + G^{(4)}\tilde{T}^{(0)}}{\tilde{T}^{(0)}}\frac{d\tilde{T}}{dx_1}\right)\phi. \tag{4.30}$$

It is clear that the last term is equal to J_{ϕ}, which is the electric energy density, and the heat flux can be written as

$$-J_Q = \left(H^{(3)}T + K^{(3)} + \frac{H^{(1)}T+K^{(1)}}{\tilde{T}}\right)\frac{d\phi}{dx_1} + \left(H^{(4)}T + K^{(4)} + \frac{H^{(2)}T+K^{(2)}}{\tilde{T}}\right)\frac{d\tilde{T}}{dx_1}. \quad (4.31)$$

While we examine the effective thermal conductivity, the imposed temperature difference needs to be very small to yield the effective thermal conductivity at a specific temperature. The effective thermal conductivity of the composite can be written as

$$\kappa^*(\Delta T, J = 0) = -\frac{J_Q}{dT/dx_1}, \quad (4.32)$$

and

$$\kappa^* = \left(H^{(3)}T + K^{(3)} + \frac{H^{(1)}T+K^{(1)}}{\tilde{T}}\right)\frac{d\phi}{dT} + \left(H^{(4)}T + K^{(4)} + \frac{H^{(2)}T+K^{(2)}}{\tilde{T}}\right), \quad (4.33)$$

where under the open-circuit condition

$$\frac{d\phi}{dT} = -\alpha^*. \quad (4.34)$$

The effective thermal conductivity can be written as

$$\kappa^* = -\alpha^* \cdot \left(H^{(3)}T + K^{(3)} + \frac{H^{(1)}T+K^{(1)}}{\tilde{T}}\right) + \left(H^{(4)}T + K^{(4)} + \frac{H^{(2)}T+K^{(2)}}{\tilde{T}}\right). \quad (4.35)$$

The effective thermoelectric figure of merit is then defined as

$$\frac{d\phi}{dT} = -\alpha^*. \quad (4.36)$$

It is worth noting that all the effective thermoelectric properties of the composite with 2D unit cell configuration are functions of temperature, while only the effective electric conductivity of the composite with layered microstructure is a function of temperature. The other thing worth noting is that the structure of equation (4.31) is so different from equation (1.5), the equation for the heat flux in homogeneous material. Substituting our effective properties back to equation (4.31) fails

to recover the equation to equation (1.5). To recover equation (4.31) to equation (1.5) it requires that

$$H^{(3)}T + K^{(3)} + \frac{H^{(1)}T + K^{(1)}}{\tilde{T}} = T\alpha^*\sigma^* = \frac{G^{(2)} + G^{(4)}\tilde{T}}{\tilde{T}}T, \tag{4.37}$$

$$H^{(4)}T + K^{(4)} + \frac{H^{(2)}T + K^{(2)}}{\tilde{T}} = T\alpha^{*2}\sigma^* + \kappa^*, \tag{4.38}$$

which, however, does not always hold true. This means that composite with 2D unit cell configuration behaves differently from the homogeneous materials, and the classic equation for predicting the optimal conversion efficiency, equation (1.18), does not work for the composite. In other words, the effective thermoelectric figure of merit does not correlate with the optimized conversion efficiency.

Since the effective figure of merit does not correlate with conversion efficiency, the thermoelectric conversion efficiency has to be examined directly by

$$H = \frac{A \cdot \phi(L)J}{A \cdot J_U\,|x=0} = \frac{\phi(L)J}{\left\langle \frac{1}{\kappa} \right\rangle^{-1}\left(\left\langle \frac{\alpha}{\kappa} \right\rangle T(0)J - \frac{dT_0}{dx}|x=0\right)}, \tag{4.39}$$

where the numerator denotes the electric energy delivered to the load resistance, whereas the denominator denotes the heat (energy) flowing in at the joint from the hot reservoir with temperature $T(0)$. The optimal conversion efficiency has to be evaluated numerically with respect to the current density.

4.4 NUMERICAL RESULTS AND DISCUSSIONS

4.4.1 *Field Distributions*

To demonstrate the analysis, we consider a thermoelectric composite consisting of Bi_2Te_3 and $Ag(Pb_{1-y}Sn_y)_mSbTe_{2+m}$ with circular fillets. We use $Ag(Pb_{1-y}Sn_y)_mSbTe_{2+m}$ as the fillets and Bi_2Te_3 as the matrix. If we consider either only a temperature difference or an electric potential difference is being imposed, the corresponding distributions of temperature, electric potential, and heat flux are shown in Figure 4.2 and Figure 4.3, where the volume fraction of the fillets is 38.48%. Homogeneous materials with $f = 0$ and 1 are also included for comparisons. Despite the fact that the equation for the composite different from the equation for the homogeneous material, the variations of temperature and electric potential in the composite are very similar to those of homogeneous materials.

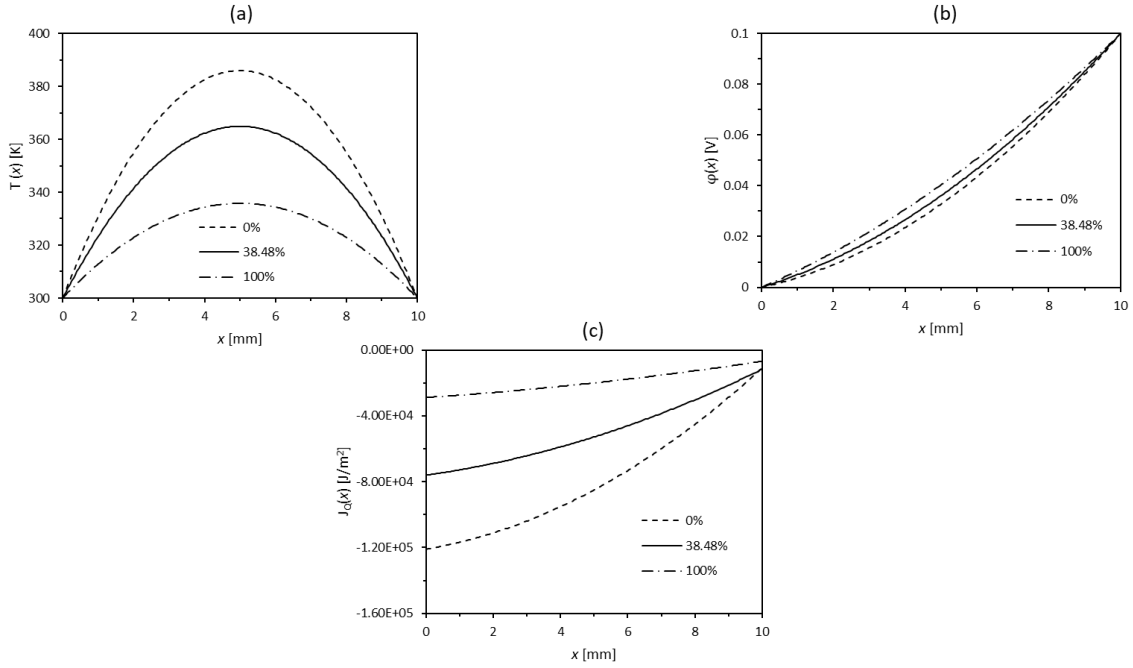

Figure 4.2. Distributions of (a) temperature, (b) electric potential, (c) heat flux in thermoelectric composite and homogeneous materials under an imposed electric potential difference of $\phi(0) = 0V$ and $\phi(L) = 0.1V$, with $T(0) = T(L) = 300K$ and f = 0%, 38.48%, 100%.

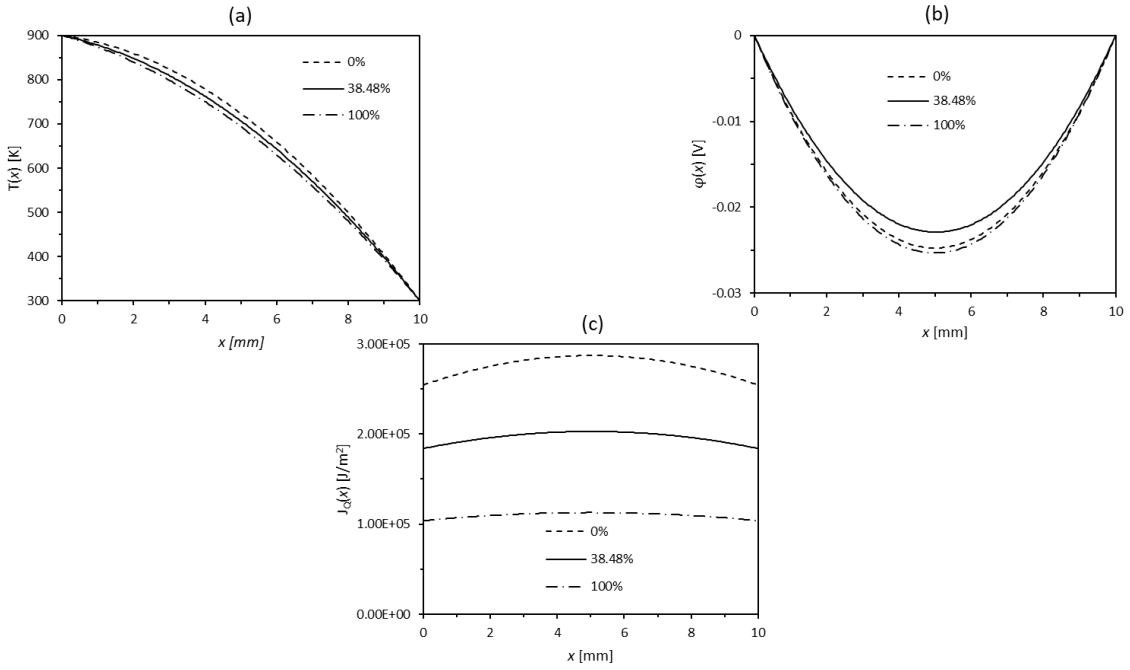

Figure 4.3. Distributions of (a) temperature, (b) electric potential, and (c) heat flux in thermoelectric composite and homogeneous materials under an imposed temperature difference of $T(0) = 900K$ and $T(L) = 300K$, with $\phi(0) = \phi(L) = 0V$ and $f = 0\%, 38.48\%, 100\%$.

4.4.2 *The Effective Properties and Conversion Efficiency*

Since the field distributions of the composite are only slightly different from those of homogeneous materials, we define a set of effective properties using equivalency principle, equations (4.27), (4.29), and (4.35). Comparisons of the original distributions and those of homogeneous material, which has its thermoelectric properties equal to the effective properties of the composite, in Figure 4.4 and Figure 4.5, show that distributions of these two materials are almost identical in temperature and electric potential, but there is a very clear discrepancy in heat flux. This can be explained by the fact that the equation of electric current density for the composite can be recovered to the one for homogeneous material with effective properties, but the equation of heat flux cannot. Because the structure of the equation of heat flux for composite is quite different from

that for homogeneous material, the heat flux of the composite is not the same as the homogeneous material, even though they have the same value of thermal conductivity. Thus, the effective figure of merit does not correlate with the conversion efficiency, and the optimal conversion efficiency has to be evaluated numerically by equation (4.39).

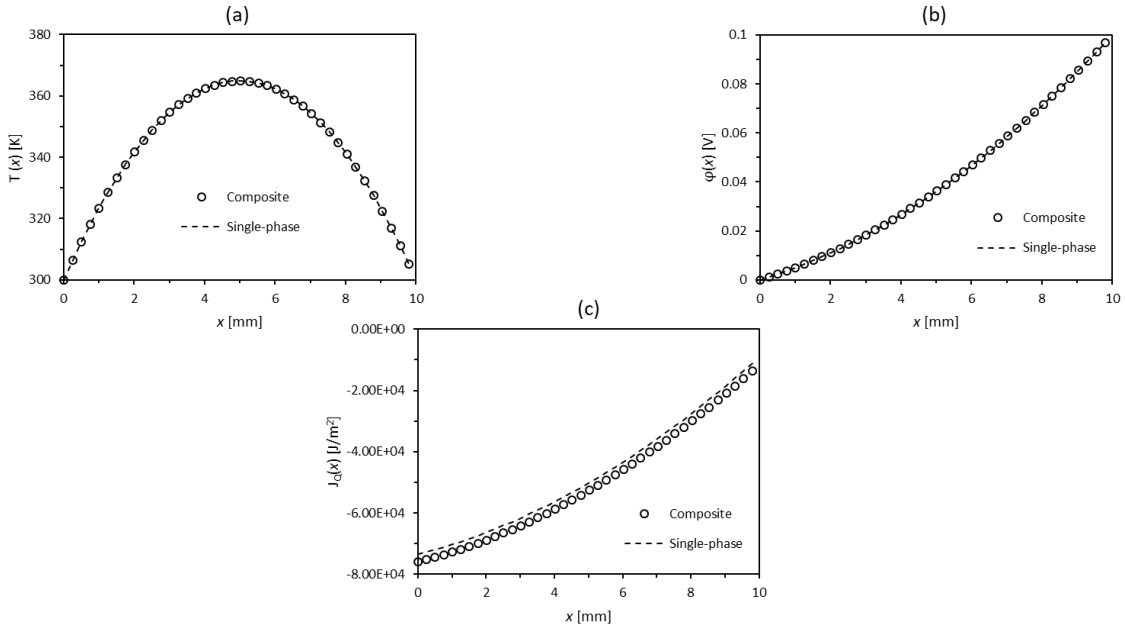

Figure 4.4. Distributions of (a) temperature, (b) electric potential, and (c) heat flux in thermoelectric composite and homogeneous materials under an imposed electric potential difference of $\phi(0) = 0V$ and $\phi(L) = 0.1V$, with $T(0) = T(L) = 300K$ and $f = 38.48\%$.

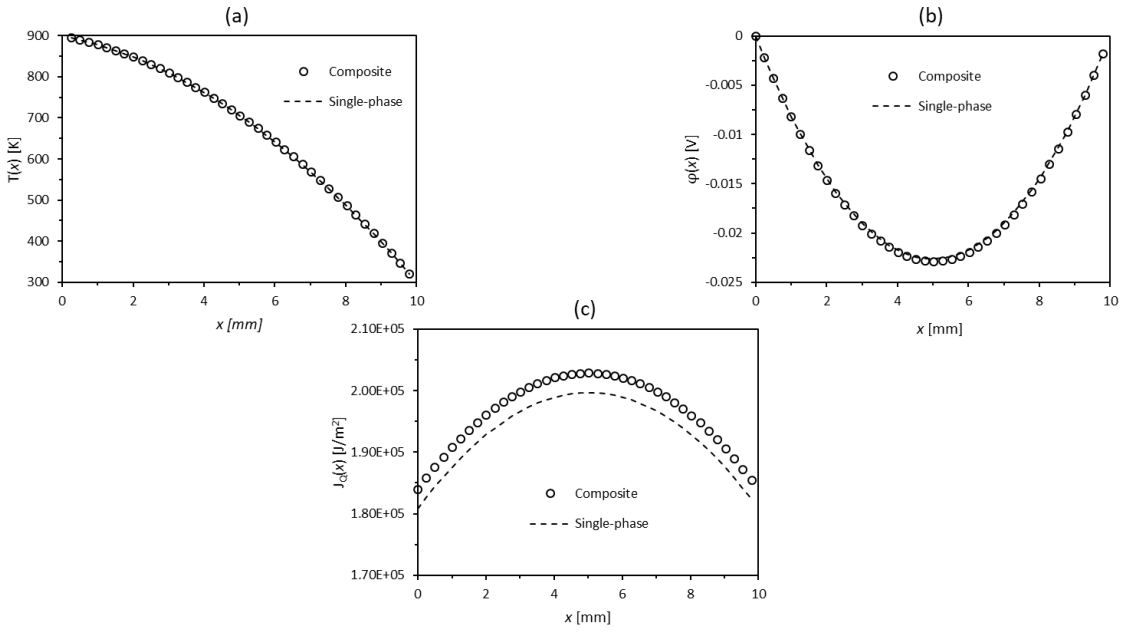

Figure 4.5. Distributions of (a) temperature, (b) electric potential, and (c) heat flux in thermoelectric composite and homogeneous materials under an imposed temperature difference of $T(0) = 900K$ and $T(L) = 300K$, with $\phi(0) = \phi(L) = 0V$ and $\phi(L) = 0V$ and $f = 38.48\%$.

We calculate the effective figure of merit and the optimal efficiency of the composite versus the volume fraction of $Ag\left(Pb_{1-y}Sn_y\right)_m SbTe_{2+m}$ with the value predicted by the classic equation. Results are shown in Figure 4.6, where we can see that even though the effective figure of merit of the composite does correspond to the trend of the efficiency, it deviates from the values predicted by the classic equation as the volume fraction increases. This suggests that the approximated optimal efficiency can be calculated by the effective figure of merit while the fillets are small. As the volume fraction of the fillets increases, the optimal efficiency has to be evaluated numerically.

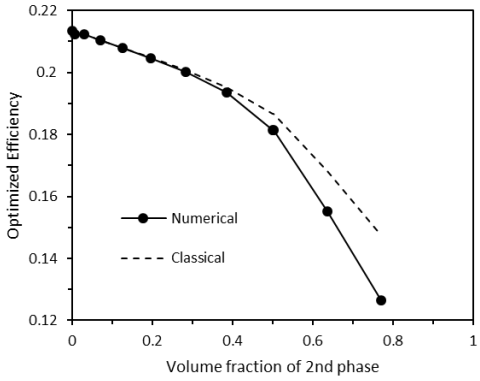

Figure 4.6. Conversion efficiencies of composite with respect to volume fraction calculated both numerically and with the classical equation.

4.4.3 *Other Configurations*

Up to this point, we have learned that the effective figure of merit is ill-defined, and the optimal conversion efficiency must be calculated numerically. As we want to find a fillet shape that helps improve the conversion efficiency, we need to do it case by case. Here we consider five different configurations: parallel, layered, unit cell with fillers with round, square, and diamond shapes, as seen in Figure 4.7. It was claimed that the upper bound of the thermoelectric conversion efficiency is attained when the composite has the first microstructure, and the lower bound attained is attained when the composite has the second microstructure. The effective figure of merit for the first configuration can be calculated by

$$Z^*T = \frac{\alpha^{*2}\sigma^*}{\kappa^*}, \tag{4.40}$$

where

$$\sigma^* = \langle\sigma\rangle,\ \alpha^* = \langle\alpha\sigma\rangle/\ \sigma^*,\ \kappa^* = \langle\kappa + T\sigma\alpha^2\rangle - T\sigma^*\alpha^{*2},$$

and the effective figure of merit for the second configuration can be calculated by equation (2.21), and both of them are well defined and can be used to predict the optimal conversion efficiency. We use these two configurations as the benchmark for other configurations.

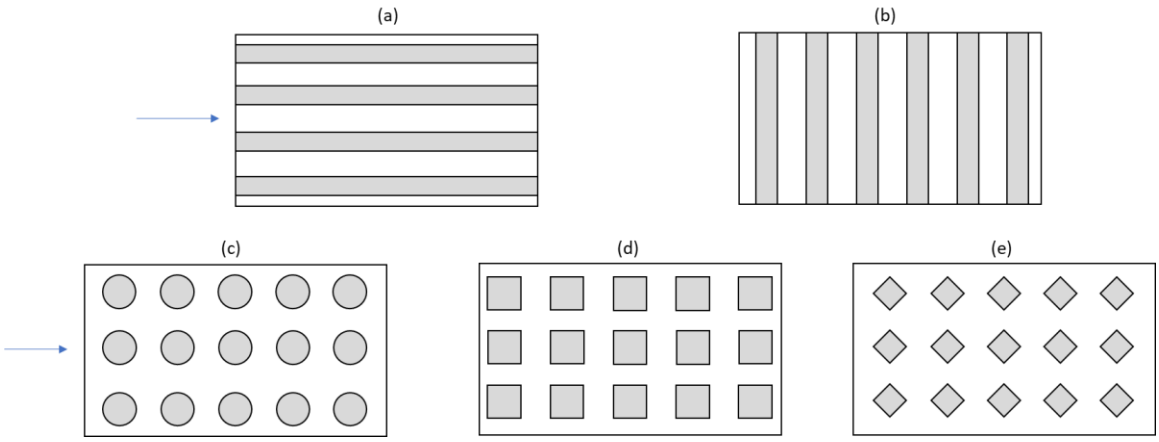

Figure 4.7. Schematics of microstructures: (a) parallel aligned with the direction of the flow; (b) layered structure perpendicular to the direction of the flow; (c) unit cells with round, (d) square, and (e) diamond shape fillers.

Figure 4.8 shows the optimized conversion efficiency of composites with three different shapes of fillers with respect to the volume fraction of Bi_2Te_3. Each case was simulated first with Bi_2Te_3 as the fillers then we swapped it for $Ag\left(Pb_{1-y}Sn_y\right)_m SbTe_{2+m}$, and each case was compared with the theoretical upper and lower bounds. For the composite with round fillers, the curve is smooth. But, there is a curve that dives below the lower bound, and we need other route to verify this result. The results for the other two cases also look less reasonable, as they are not smooth and sometimes too low. What makes this model less dependable is the process of selecting the constant X. We do not have a better way to pick the value of X other than choosing the value of X that results in the smallest residual value. In some cases, the residual values are similarly small for several different values of X, but differences among those values of X are quite large, as shown in Fig. 4.9, and the value of the constant X greatly affects the final results. In addition, we cannot see a clear physical meaning behind the constant X.

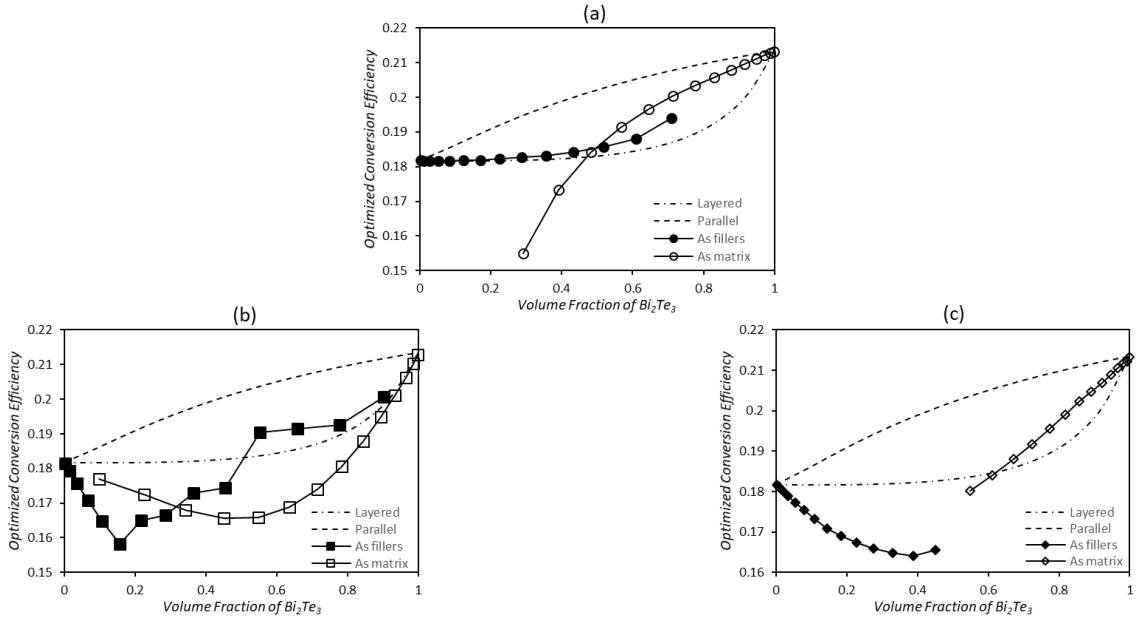

Figure 4.8. Optimized conversion efficiency with respect to the volume fraction of the 2nd phase of composites with (a) round (b) square, and (c) diamond shape fillers.

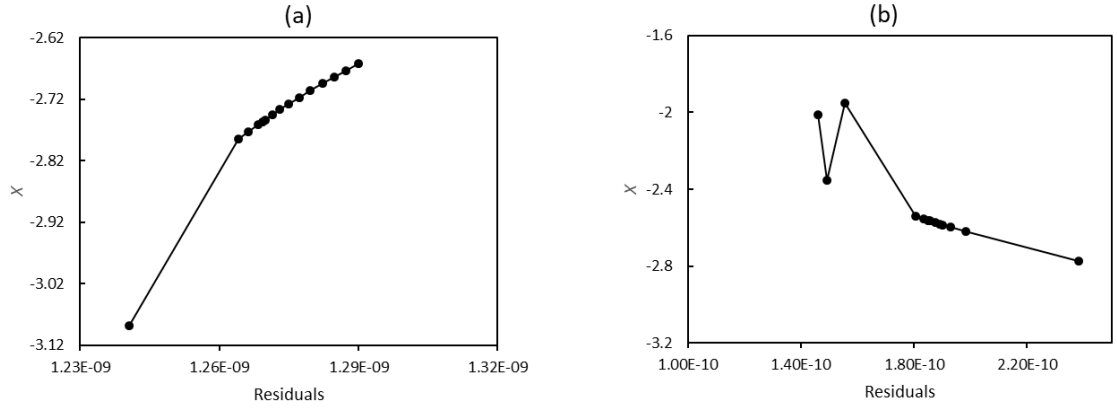

Figure 4.9. The *X* values calculated correspond to the resulting residual values for (a) circle and (b) squire unit cell structure, for the volume fraction of 12.5%, and 70% respectively. For most cases with circle unit cell structure there are appreciable drops in residual values and the corresponding values of *X*, as shown in (a). But in many cases, it is not that clear as shown in (b).

4.5 SUMMARY

In this chapter, we have presented that the behavior of the composite with 2D configuration is very different from that of single-phase materials. Its effective properties, especially the effective thermal conductivity, are ill-defined, and the effective thermoelectric figure of merit does not directly correlate with the conversion efficiency. Thus, the optimized conversion efficiency has to be evaluated numerically. We have also shown that the method developed by Yang has its limitation as it can only be used in certain special cases. Thus, we need an alternative way to analyze the behavior of thermoelectric composites with 2D, or even 3D, microstructures.

Chapter 5. ANALYSIS OF THERMOELECTRIC COMPOSITES BY FINITE ELEMENT METHOD

5.1 INTRODUCTORY REMARKS

As discussed in the last chapter, there are few drawbacks for using the asymptotic homogenization method to solve 2D thermoelectric problems. It is computationally expensive and there are many uncertainties. Therefore, we need an alternative way to solve the 2D/3D thermoelectric problem. Since it is not computationally cheap by applying the asymptotic homogenization method first and then solving the variables with finite element method, we think of solving the entire problem with finite element method directly, as shown in Figure 5.1. By having enough number of repeating cells, we can achieve smooth field distributions, which can be seen as an approached macroscopic field distribution of a homogenized composite. Rather than writing our own finite element program, this study is done by using ANSYS Workbench (v. 16.0), a commercial finite element analysis software. ANSYS, which has a large library of elements, supports many different types of analysis and its ability to performing the thermoelectric analysis has been enhanced since ANSYS 9.0[84].

In the next section, we will show the formulation of thermoelectric finite element model in ANSYS as a foundation of this study. Then we will verify the models by comparing the model results with the more established solutions. In Section 5.4, we define effective properties and analyze the conversion efficiency to show how the effective figure of merit correlates to the optimized efficiency. The summary for the chapter is presented in the last section.

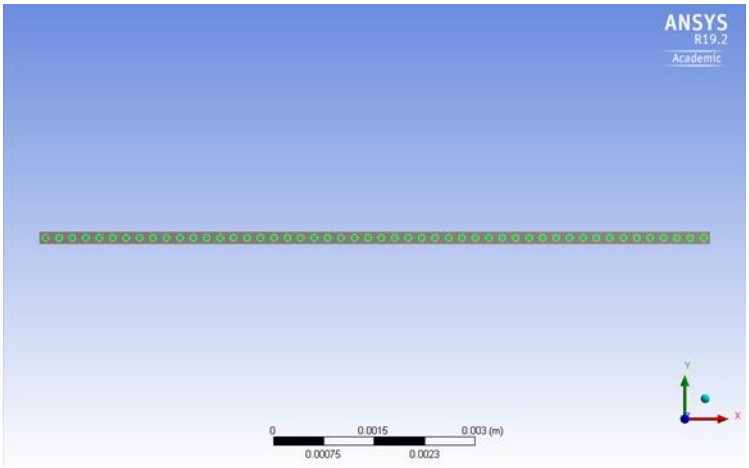

Figure 5.1. 2D thermoelectric model in ANSYS

5.2 FINITE ELEMENT FORMULATION

In ANSYS, the system of thermoelectric finite element equations is obtained by applying the Galerkin method[85] to the equations of heat flow equation (1.8) and continuity of electric charge equation (1.4). That is to approximate the temperature T and electric potential ϕ over a finite element as:

$$T = N \cdot T_e, \tag{5.1}$$

$$\phi = N \cdot \phi_e, \tag{5.2}$$

where N is a vector of element shapes functions, T_e is a vector of nodal temperatures, and ϕ_e is a vector of nodal electric potentials. Second, writing the system of equations (5.1) and (5.2) in a weak projective form. Then integrating the projective equations by parts over the element volume V. Lastly, taking into account the Neumann boundary conditions. The system of thermoelectric finite element equations is:

$$\begin{bmatrix} C^{TT} & 0 \\ 0 & C^{\phi\phi} \end{bmatrix} \begin{Bmatrix} \dot{T}_e \\ \dot{\phi}_e \end{Bmatrix} + \begin{bmatrix} K^{TT} & 0 \\ K^{\phi T} & K^{\phi\phi} \end{bmatrix} \begin{Bmatrix} T_e \\ \phi_e \end{Bmatrix} = \begin{Bmatrix} Q + Q^P + Q^e \\ I \end{Bmatrix}, \tag{5.3}$$

where the element matrices and load vectors are obtained by numerical integration (using Gauss quadrature):

$K^{TT} = \int_V \nabla N \cdot [\kappa] \cdot \nabla N dV$ – thermal stiffness matrix

$K^{\phi\phi} = \int_V \nabla N \cdot [\sigma] \cdot \nabla N dV$ – electric stiffness matrix,

$K^{\phi T} = \int_V \nabla N \cdot [\sigma] \cdot [\alpha] \cdot \nabla N dV$ – Seebeck stiffness matrix,

$C^{TT} = \rho \int_V CNN dV$ – thermal damping matrix,

$C^{\phi\phi} = \int_V \nabla N \cdot [\epsilon] \cdot \nabla N dV$ – dielectric damping matrix,

Q – vector of combined heat generation loads,

$Q^P = \int_V \nabla NT[\alpha] \cdot J dV$ – Peltier heat load vector,

$Q^e = -\int_V N \nabla \phi \cdot J dV$ – electric power load vector,

I – electric current load vector.

Thermal loads (Q) can be in the form of imposed temperature, point heat flow rate, surface heat flux, convection, or radiation, as well as body heat generation rate for causes other than electric power dissipation (accounted for in Q^e). Electrical loads (I) can be in two different form: the form of imposed electric potential and point electric current.

The ANSYS input of material matrices $[\kappa]$, $[\sigma]$, $[\alpha]$, $[\epsilon]$ is in the form of their diagonal terms, i.e. material coefficients along the x, y, z axes, which can be directional. All material properties can be temperature dependent. Therefore, Thomson effect is also taken into account.

The global matrix equation is then assembled from the equations of individual finite element. Since the thermal load vector depends on the electric solution, the analysis is non-linear and requires at least two iterations to converge.

The solution of the global matrix yields temperature (T_e) and electric potentials (ϕ_e) at each node, or reactions in the form of heat flow rate and electric current at nodes with imposed temperature and electric potential, respectively. The temperature gradient and electric field can be calculated as

$$\nabla T = \nabla N \cdot T_e, \tag{5.4}$$

$$E = -\nabla N \cdot \phi_e, \tag{5.5}$$

which are then substituted into equations (5.4) and (5.5) to obtain the values of J, q fields, and Joule heat generation density for each element. Thus, the problem is solved completely.

5.3 VERIFICATION OF FINITE ELEMENT MODELS

5.3.1 *Single Phase Thermoelectric Material and Bi-layered Composite*

To verify the credibility of the results from ANSYS, we consider a single-phase thermoelectric element, as shown in Figure 5.2 (a), which is subject to specified temperatures and electric potentials of ($T_0,\ \phi_0$) and ($T_1,\ \phi_1$) at both ends. All the material properties are assumed to be independent of temperature and it is assumed that no heat transfer occurs on the lateral direction. Under theses assumption, the analytical solutions of the distribution of electric potential, distribution of temperature, heat flux and current density can be easily derived[79].

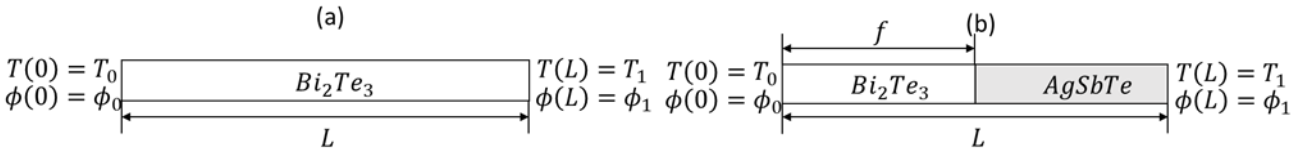

Figure 5.2. Schematics of (a) a single-phase thermoelectric material and (b) a bi-layered composite thermoelectric element

The distribution of electric potential, temperature, and current density of a single-phase thermoelectric element are governed by

$$\phi(x) = \frac{\alpha J^2}{2\kappa\sigma}x^2 - \left(\frac{\alpha J^2}{2\kappa\sigma}\cdot L + \frac{\alpha(T_1-T_0)}{L} + \frac{J}{\sigma}\right)x + \phi_0, \tag{5.6}$$

$$T(x) = -\frac{J^2}{2\kappa\sigma}x^2 + \left(\frac{J^2}{2\kappa\sigma}\cdot L + \frac{T_1-T_0}{L}\right)x + T_0, \tag{5.7}$$

$$J = [\sigma\alpha\,(T_0 - T_1) + \sigma(\phi_0 - \phi_1)]/L, \tag{5.8}$$

respectively. We also considered a slightly more complicated case with a bi-layered thermoelectric element which consists of two distinct materials subject to the same boundary conditions as the first case, as shown in Figure 5.2 (b). The distribution of electric potential and temperature can be calculated by the following equations

$$\phi = \begin{cases} \frac{\alpha_A J^2}{2\sigma_A\kappa_A}x^2 - \left(\frac{J}{\sigma_A} + \alpha_A a_A\right)x + c_A & 0 \le x < f, \\ \frac{\alpha_B J^2}{2\sigma_B\kappa_B}x^2 - \left(\frac{J}{\sigma_B} + \alpha_B a_B\right)x + c_B & f < x \le L, \end{cases} \tag{5.9}$$

and

$$T = \begin{cases} -\frac{J^2}{2\sigma_A\kappa_A}x^2 + a_A x + b_A & 0 \le x < f, \\ -\frac{J^2}{2\sigma_B\kappa_B}x^2 + a_B x + b_B & f < x \le L, \end{cases} \tag{5.10}$$

Where a_A, a_B, b_A, and b_B can be obtained by solving the following system of linear equations

$$\begin{bmatrix} 0 & 1 & 0 & 0 \\ 0 & 0 & L & 1 \\ f & 1 & -f & -1 \\ (\alpha_A - \alpha_B)f - \kappa_A & J(\alpha_A - \alpha_B) & \kappa_B & 0 \end{bmatrix}\begin{bmatrix} a_A \\ b_A \\ a_B \\ b_B \end{bmatrix} = \begin{bmatrix} T_0 \\ T1 + \frac{J^2L^2}{2\sigma_B\kappa_B} \\ -\frac{J^2f^2}{2\sigma_B\kappa_B} + \frac{J^2f^2}{2\sigma_A\kappa_A} \\ \frac{(\alpha_A-\alpha_B)J^3f^2}{2\sigma_A\kappa_A} + \frac{(\sigma_A-\sigma_B)J^2f}{\sigma_A\sigma_B} \end{bmatrix}. \tag{5.11}$$

The first two rows represent the temperature boundary conditions at two ends and the last two rows represent the continuity conditions of temperature and heat flux at the interface, $x = f$. The subscript A and B denote the first and the second materials in the bi-layered thermoelectric

elements. The current density can be solved based on the continuity of electric potential at the interface.

Two finite element models have been developed in ANSYS that correspond to the two cases presented above, and the dimensions of the two models are shown in Figure 5.3. ANSYS has included one element type, PLANE223, to handle 2-D thermal-electric systems. PLANE223, which has been used in this study, is 8-node quadrilateral that allows degeneration into a 6-node triangle, and coupled-field properties with structural, thermal, and electrical degrees of freedom at their nodes. The properties of the modeled materials Bi_2Te_3 and $Ag\left(Pb_{1-y}Sn_y\right)_m SbTe_{2+m}$ are listed in Table 2.1. By comparing modeling results with the analytical solution, it is shown that the element size of 1 mm is sufficient, resulting in only 10 elements needed in each model. The temperature and electric potential differences are imposed to the thermoelectric elements with $T(0) = 1500K$, $\phi(0) = 0V$ at the one end and $T(L) = 300K$, $\phi(L) = 0.1V$ at the other end. Figure 5.4 shows that the field distributions calculated from the finite element model are nearly identical with the analytical solution. The difference of calculated current density between finite element analysis and the analytical solution is under 0.1%. This outcome verifies the credibility of the results from ANSYS model.

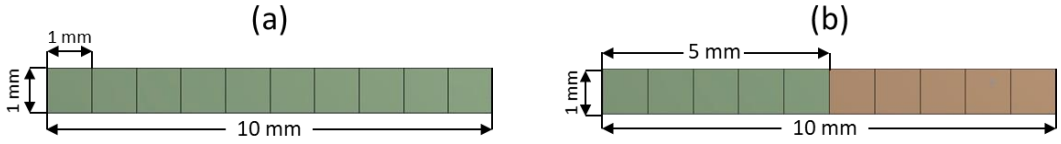

Figure 5.3. Finite elements models of (a) a single-phase thermoelectric material and (b) a bi-layered composite thermoelectric element where the different colors denote different materials assigned to the element.

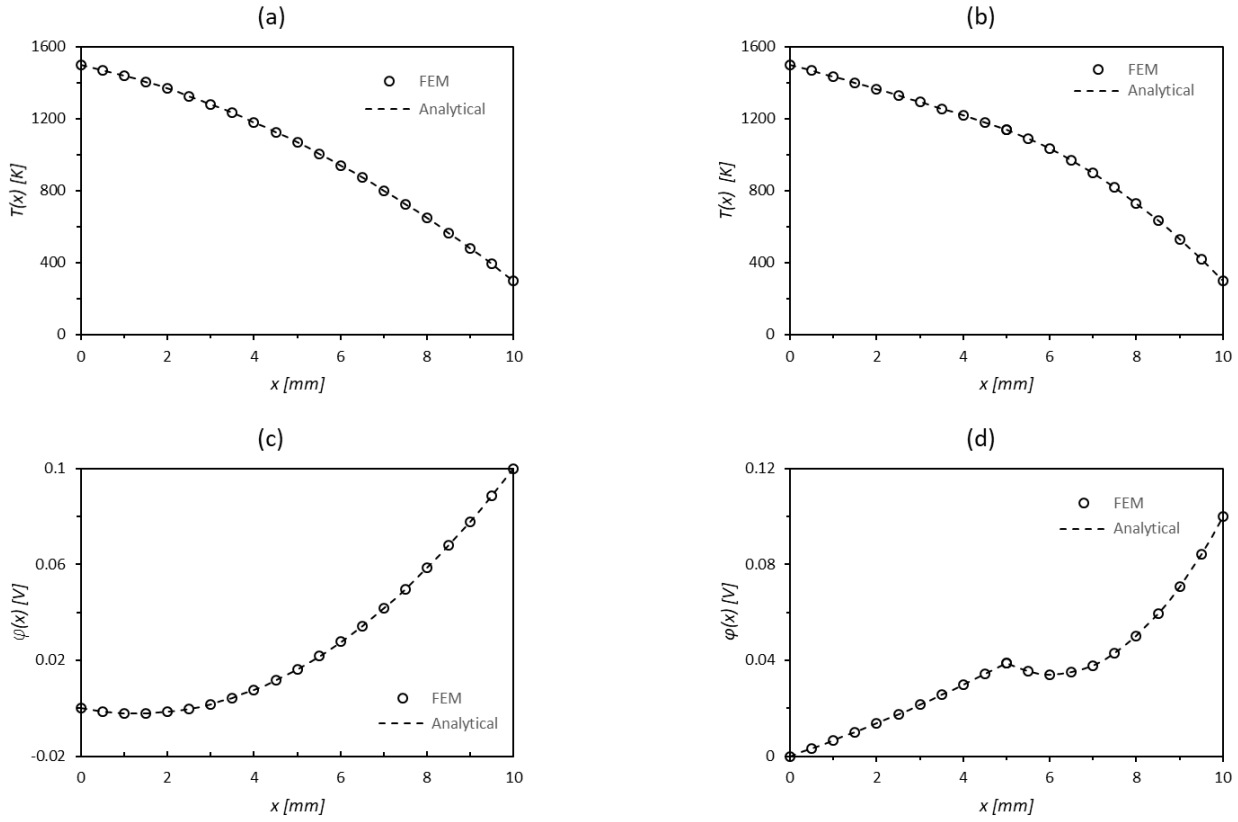

Figure 5.4. The comparison of the distributions of temperature, (a) and (b), and electric potential, (c) and (d), for the single-phase thermoelectric material, (a) and (c), and bi-layered composite, (b) and (d), under an imposed electric potential difference of 0.1 V, with T(0) = 1500K, T(10) = 300K.

5.3.2 *Periodic Layered Composite*

To verify the idea that the behavior of a thermoelectric composite with periodic microstructure can be simulated by a finite element model with a sufficient number of repeating cells, we consider a layered thermoelectric composite, in which all the field variables and materials parameters are dependent only on axial direction without any lateral flow, for which we have rigorous analytical solutions developed in Chapter 2. Several finite element models, with different numbers of repeating cells, were developed to compare with the analytical solutions, as shown in Figure 5.5. Each cell contained two distinctive materials, $Ag\left(Pb_{1-y}Sn_y\right)_m SbTe_{2+m}$ and Bi_2Te_3. The models were run under the boundary of $T(0) = 1500K$, $T(L) = 300K$, $\phi(0) = 0V$, and $\phi(L) = 0.1V$. The simulation results showed that the field distribution became smooth without fluctuating and almost identical with the analytical solutions when the number of repeating cells reached 50, as shown in Figure 5.6. The discrepancy of calculated current density went under 0.1% when the number of periods went over 50 and the discrepancy of calculated heat flux went under 0.1% when the number of periods went over 20. Therefore, the behavior of a thermoelectric composite with periodic microstructure can be simulated by a finite element model with 50 repeating cells. The finite elements model can provide satisfactory accuracy even when the size of the cell, 0.2 mm, does not fall under the microscopic scale.

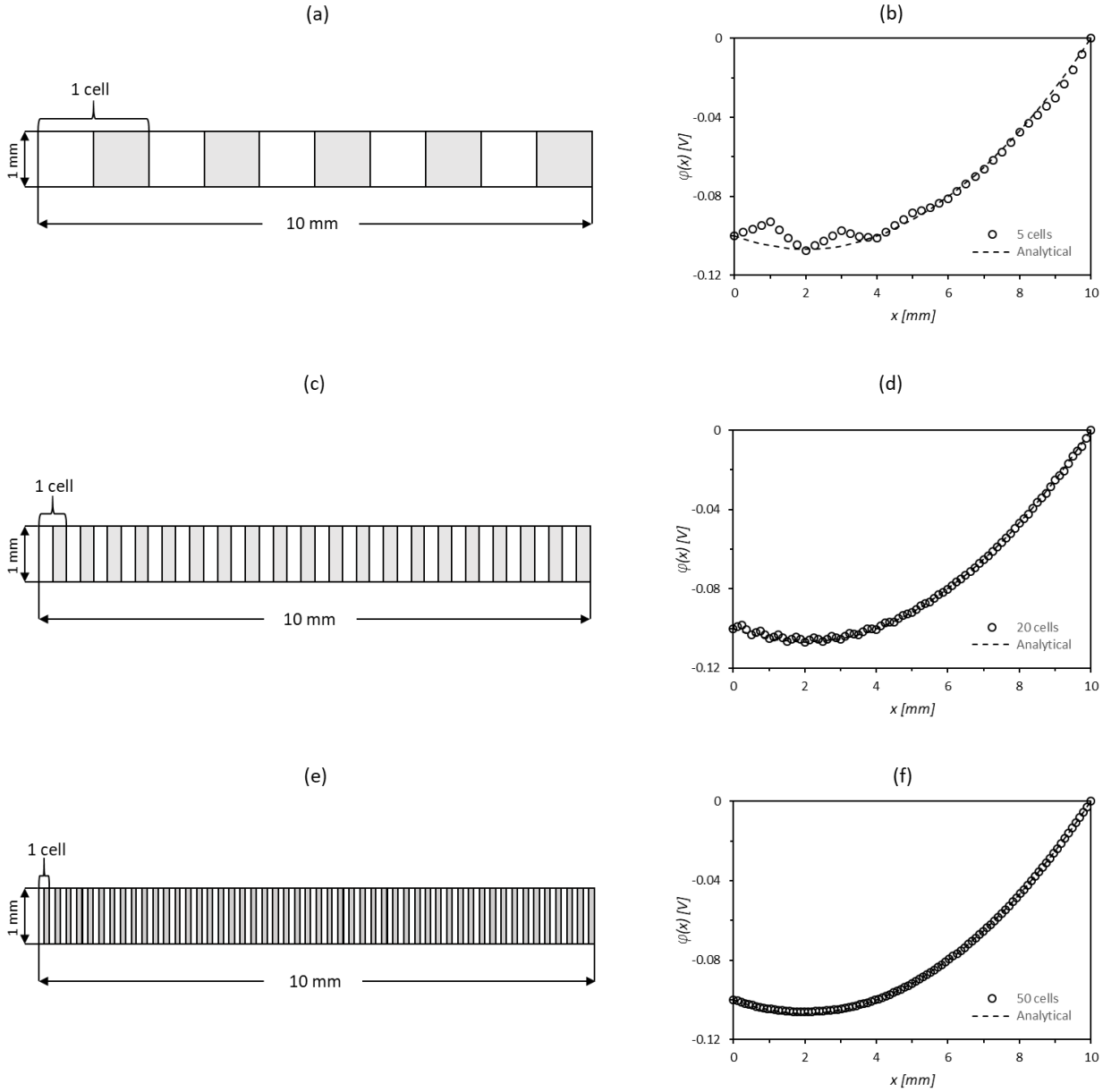

Figure 5.5. Finite element models with (a) 5 cells, (c) 20 cells, (e) 50 cells and corresponding electric potential distributions (b), (d), and (f) under an imposed electric potential difference of 0.1 V, with T(0) = 1500K, T(10) = 300K.

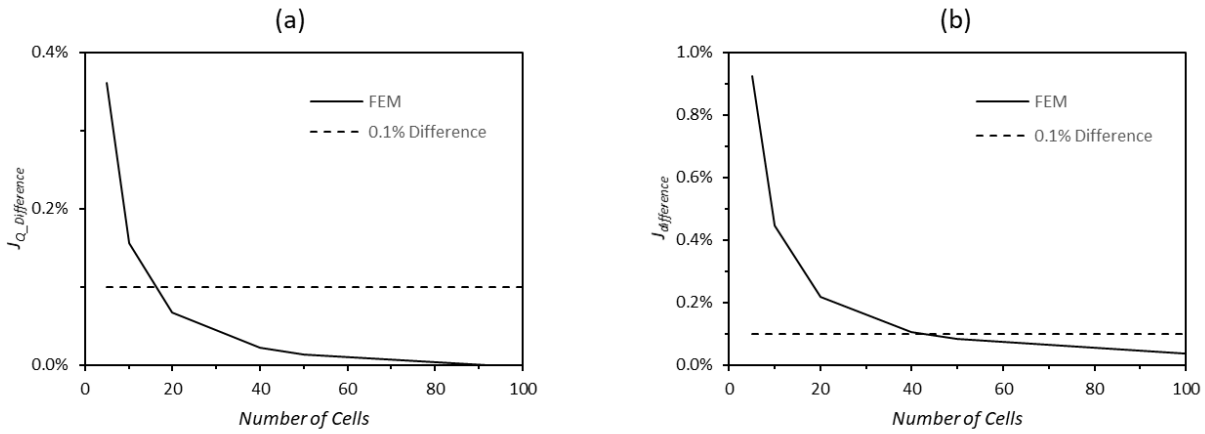

Figure 5.6. The differences of the calculated (a) heat flux at the hot end and (b) current density between the finite element model and analytical solution. As the number of cells gets larger, both values converge to the analytical solutions.

5.3.3 *Composite with 2D Configuration*

As we move from 1D cases to 2D cases, we consider a thermoelectric composite with round fillets, which we have learned the solutions from the last chapter, as shown in Figure 5.7. Due to the uncertainties of the solutions from the asymptotic analysis for the composite with larger fillets, the fillers of the tested composite are limited to a smaller size. A finite element model with 50 cells was built where a round fillet with a radius of 0.04 mm was in the center of each 0.2 mm cell. $Ag\left(Pb_{-1y}Sn_y\right)_m SbTe_{2+m}$ was used as matrix and Bi_2Te_3 as fillers. Temperatures and electric potentials were imposed at two ends with no lateral flow through the boundaries. Figure 5.8 shows the results of the model under the boundary condition of $T(0) = 900K$, $T(L) = 300K$, $\phi(0) = 0V$, and $\phi(L) = 0.1V$. The field distributions obtained by the finite element model are identical with the solutions from the last chapter. As far as the optimum mesh density is concerned, a parametric study of element size versus heat flux and current density has been performed to show that a model with 5000 elements could yield good accuracy and it converges at 20,000 elements.

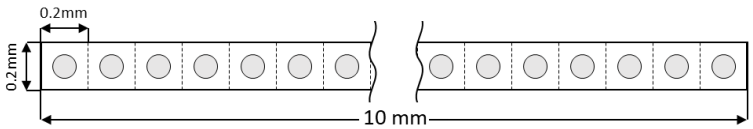

Figure 5.7. Finite element model with 50 round fillets.

Numerical tests suggested that the 2D ANSYS model worked well as compared to the known solution. As a result, the 2D system will be analyzed following the same modeling approaches used in the numerical validation process.

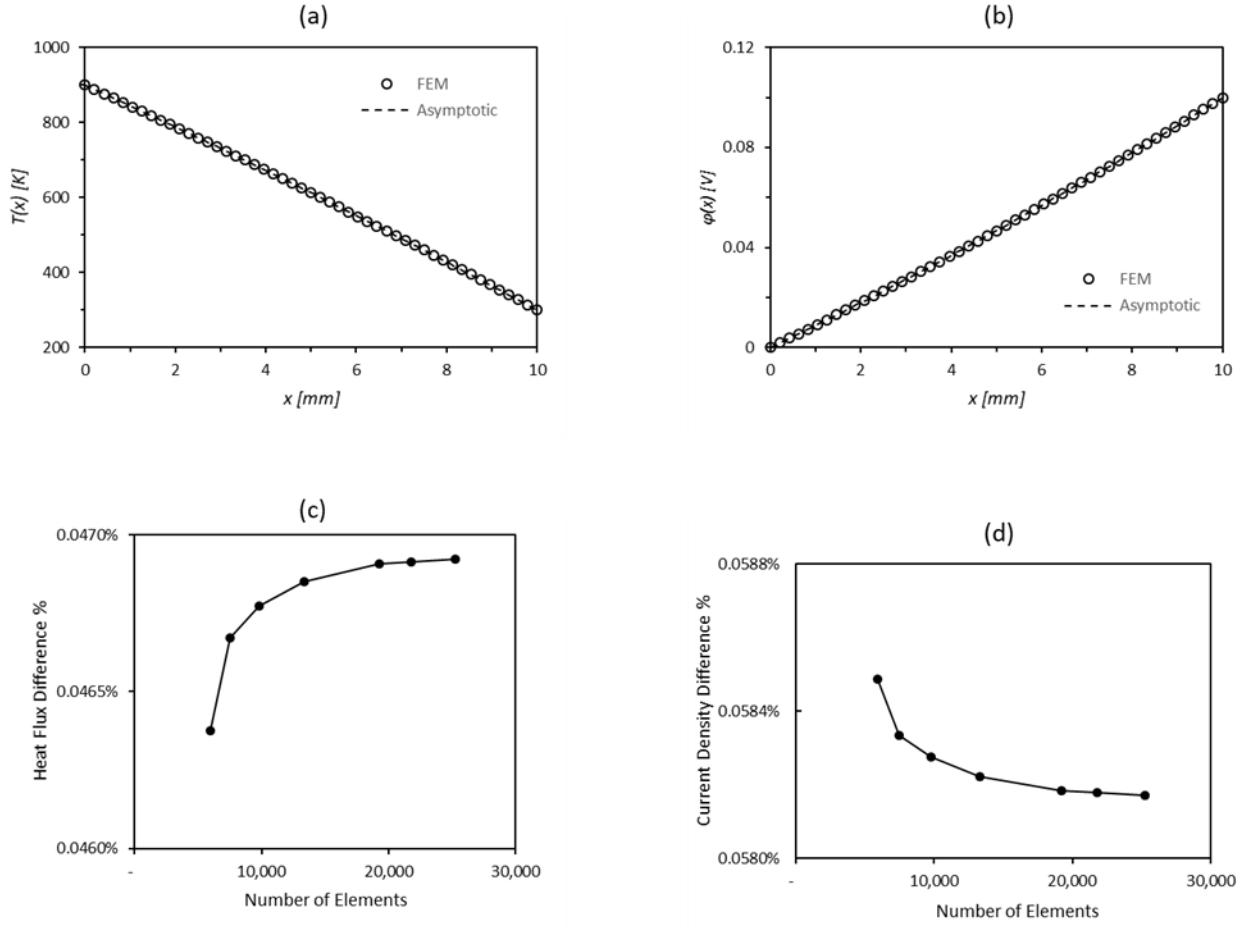

Figure 5.8. the field distribution of (a) temperature and (b) electric potential of thermoelectric composite calculated by both finite element analysis and asymptotic analysis under an imposed electric potential difference of 0.1 V, with T(0) = 900K, T(10) = 300K. The increase in the number of elements leads to the convergence of both (c) calculated heat flux and (d) current density.

5.4 Effective Properties and Effective Behavior of 2D TE Composites

5.4.1 *The Effective Thermoelectric Properties*

All the effective thermoelectric properties are defined with the same equivalency principle used in the previous chapters, as shown in equations (4.26), (4.29), and (4.32). From what we have learned, we know that all the effective properties need to be defined under very limited conditions because the effective properties of the composite can be temperature dependent. Therefore, a parametric study of imposed temperature and an electric potential difference versus defined effective thermoelectric properties has been performed. Figure 5.9 shows that the effective Seebeck coefficient and thermal conductivity start to converge when the imposed temperature difference is smaller than 1K, and the electric conductivity also converges when the imposed electric potential differences get smaller than 0.01V. Based on this study, the electric potential difference of 0.01V and temperature difference of 0.1K were selected as the test conditions for the effective properties.

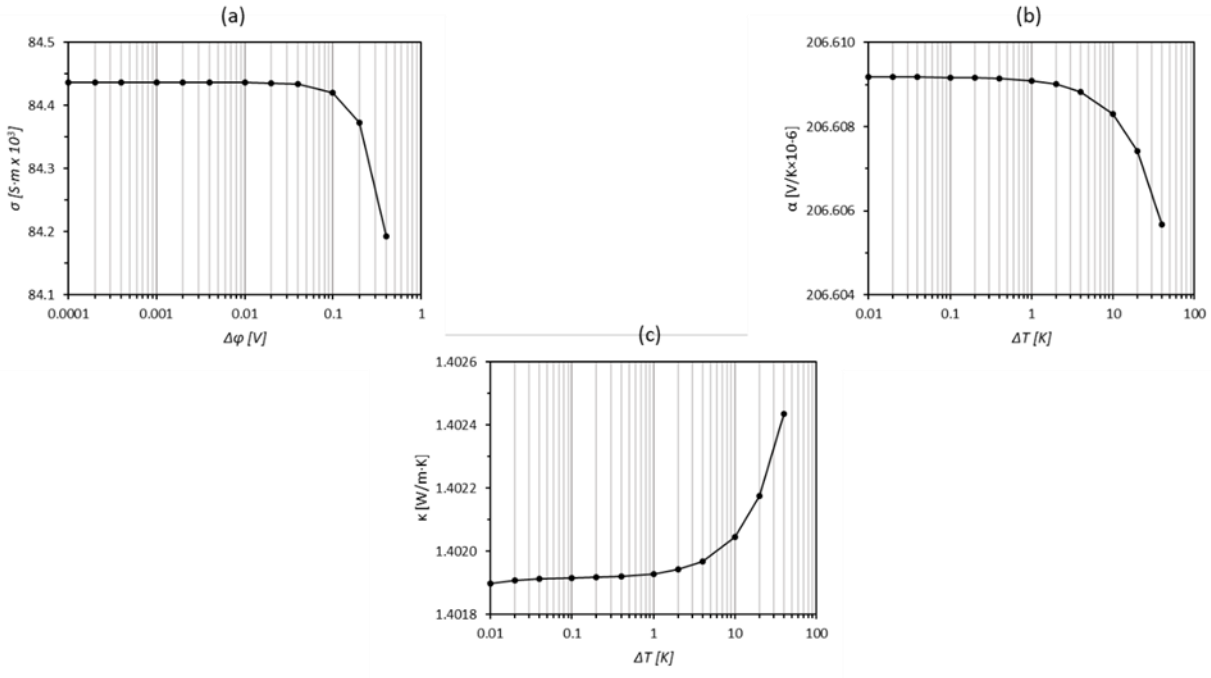

Figure 5.9. Effective (a) electric conductivity, (b) Seebeck coefficient, and (c) thermal conductivity versus imposed (a) electric potential and (b), (c) temperature differences.

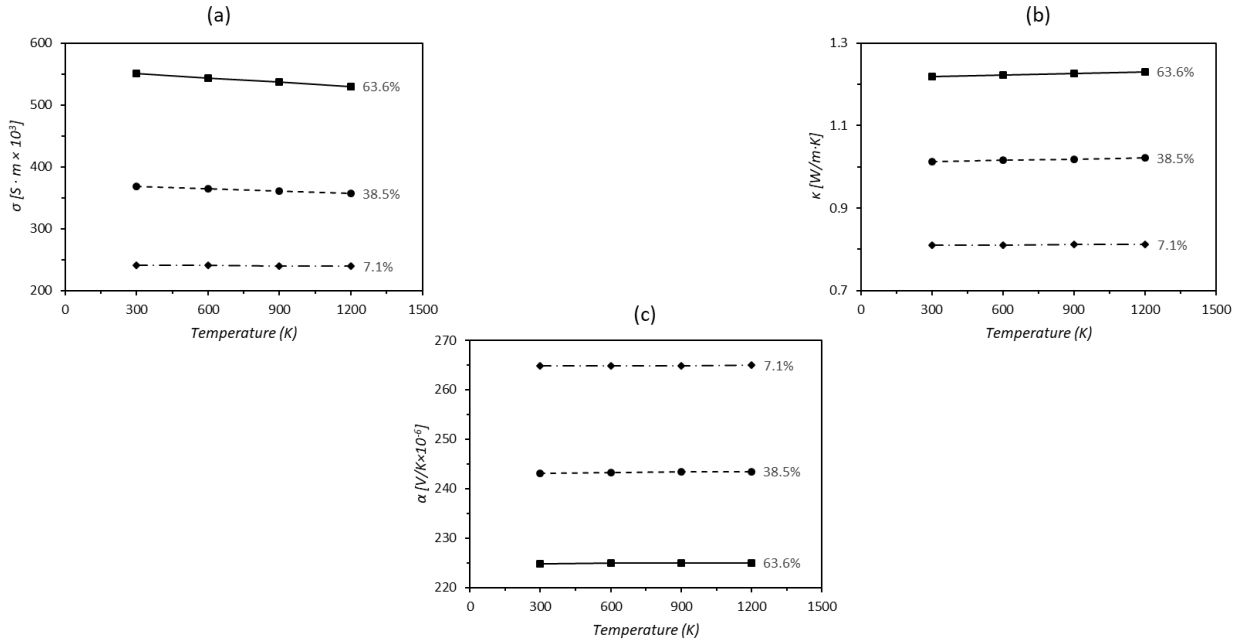

Figure 5.10. The effective (a) electric conductivity, (b) thermal conductivity, and (c) Seebeck coefficient versus temperature and the different volume fraction of the fillers as represented by different curves.

5.4.2 *Effective Behavior*

We have learned from the last chapter that the behavior of the thermoelectric composites is different from the behavior of single-phase thermoelectric materials. But how great is the difference? If the difference is small, can the behavior of a composite be approached by the behavior of a single-phase material with its properties equal to the effective properties of the composite? If the answer is yes, the effective properties of a composite can be used to estimate the performance of that specific composite.

To answer this question, the finite element model of the 2D composite was compared with two single-phase models. One model was developed in ANSYS with temperature dependent thermoelectric properties equal to the values calculated in the last section. The other model was a simple 1-D model with constant thermoelectric properties equal to the average value of the

effective properties that could be solved analytically. These models were compared under two specific boundary conditions with 3 different filler sizes. The first boundary condition had only a temperature difference being imposed, with $T_1 = 300K$ at cold end and $T_0 = 900K$ at the hot end. The second boundary condition had only an electric potential difference being imposed, with $\phi_1 = 0V$ at the right end and $\phi_0 = 0.1V$ at the left end. The three filler radii were 0.03 mm, 0.07 mm, and 0.09 mm which resulted in the volume fractions of the filler of 7.1%, 38.5%, and 63.6%, respectively.

The distributions of temperature, and electric potential of the most extreme case, the composite with the largest filler size, are shown in Figure 5.11. The field distributions of the single-phase finite element model are almost identical with the field distributions of the composite. More surprisingly, the distributions calculated analytically by ignoring the temperature dependency of the material properties are also very close to the other cases. Figure 5.12. shows that the calculated heat flux and current density of the single-phase material are deviating from those of the composite as the volume fraction of the composite fillers increases. The discrepancies, however, are all under 1.7% difference.

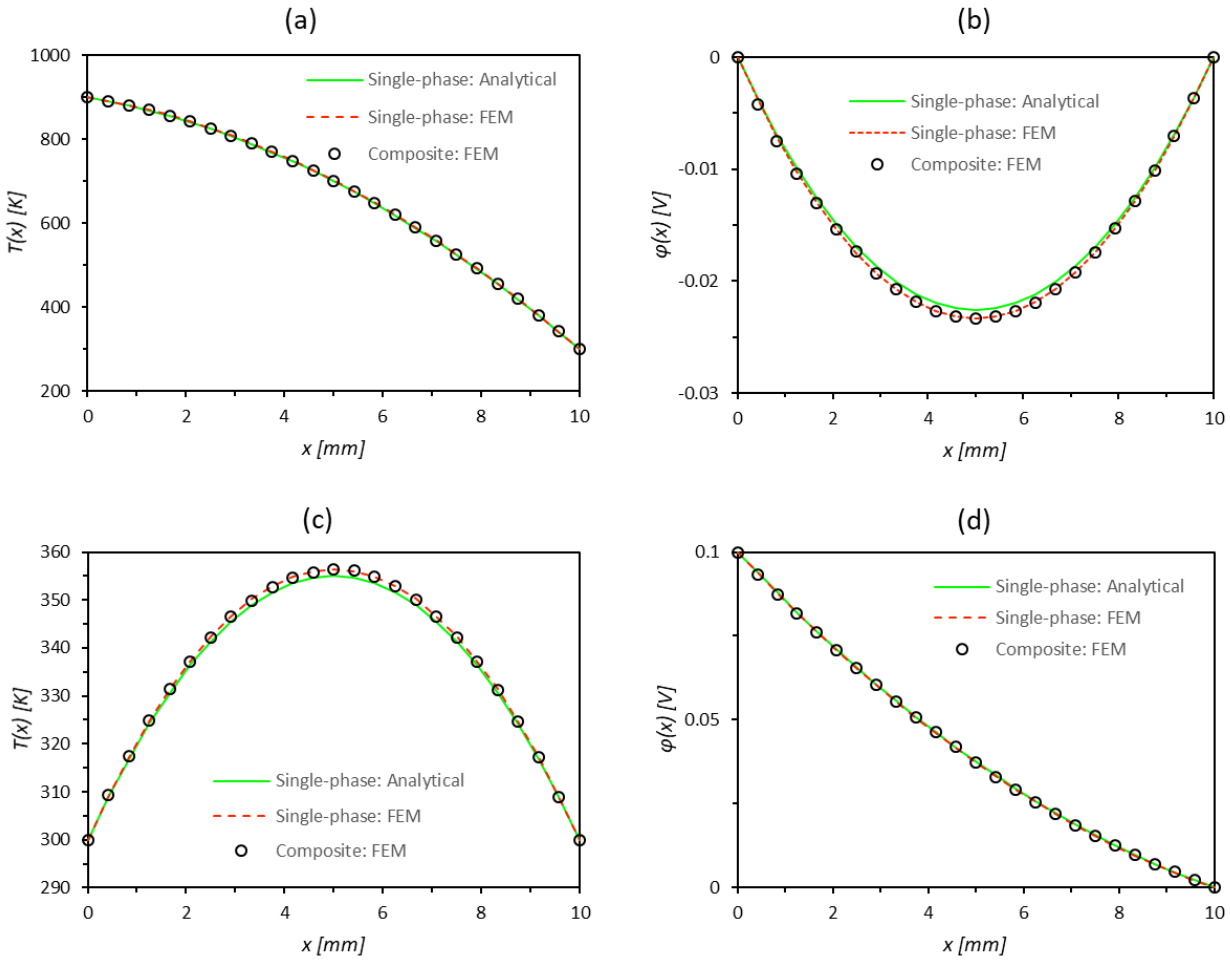

Figure 5.11. The (a), (c) temperature and (b), (d) electric potential distributions of three models under (a), (b) imposed temperature difference, and (c), (d) imposed electric potential difference.

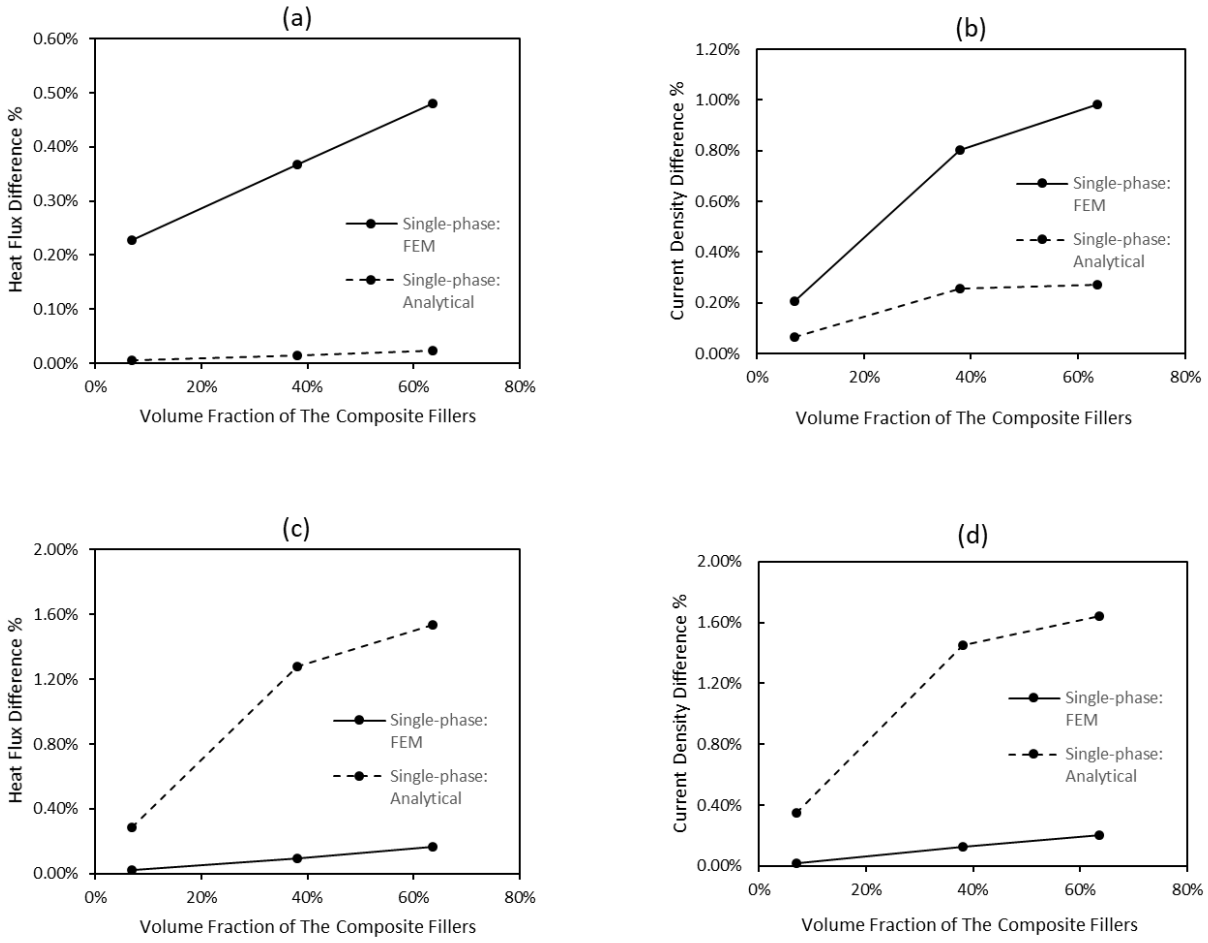

Figure 5.12. Differences of (a), (c) heat flux and (b), (d) current density between the single-phase modes and the composite model under (a), (b) imposed temperature difference and (c), (d) electric potential difference.

5.4.3 *Conversion Efficiency*

One of the most crucial things we want to know is that if the composite's effective thermoelectric figure of merit correlates to its optimal conversion efficiency. If the effective figure of merit does correlate to optimal conversion efficiency, the performance of any combination of two materials, with specific filler size, can be evaluated by two simple steps of finite element analysis: first, to evaluate the effective electric conductivity and, secondly, to evaluate the effective thermal conductivity and effective Seebeck coefficient. We calculated the optimized conversion efficiency

of the composite, considered Bi_2Te_3 both as fillers and matrix, versus the volume fraction of Bi_2Te_3 with $T(0) = 900K$ amd $T(L) = 300K$, as shown in Figure 5.13, along with the conversion efficiency predicted using the average effective figure of merit based on a classical equation 1.18. It is clear that there is almost no discrepancy between the actual efficiency and the efficiency predicted from the effective figure of merit. The is only 0.03% of difference between the actual and predicted efficiency from the most extreme case. This suggests that the effective thermoelectric figure of merit of composite does correlate with its thermoelectric conversion efficiency and can be used to estimate the performance of thermoelectric composite.

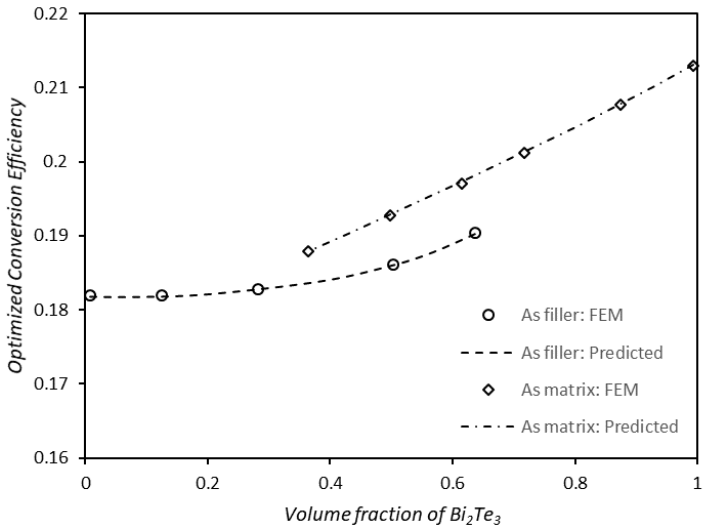

Figure 5.13. Conversion efficiencies of composite versus volume fraction of Bi_2Te_3 both as fillers and matrix. There is almost no difference between directly optimized value and the results converted from effective figures of merit.

We also carried out the same analysis on the composite with different filler shapes, square and diamond. In both cases they behave very similarly to the composite with round fillers, and their effective figure of merits are also correlated to their conversion efficiency. Figure 5.14 shows the optimized conversion efficiency of composite, with three different filler shape, versus the volume

fraction of Bi2Te3 along with the theoretical upper and lower bounds. All the curves are smooth, and, in general, lay between the upper and lower bounds. There are only a few points under the lower bound, but no points go higher than the upper bounds. It yields a similar conclusion to what we obtained in chapter 2 that the optimized conversion efficiency of the composite, composed by $Ag(Pb_{1-y}Sn_y)_mSbTe_{2+m}$ and Bi_2Te_3, can only be lower but not higher than both of its constituents even with two-dimensional configuration.

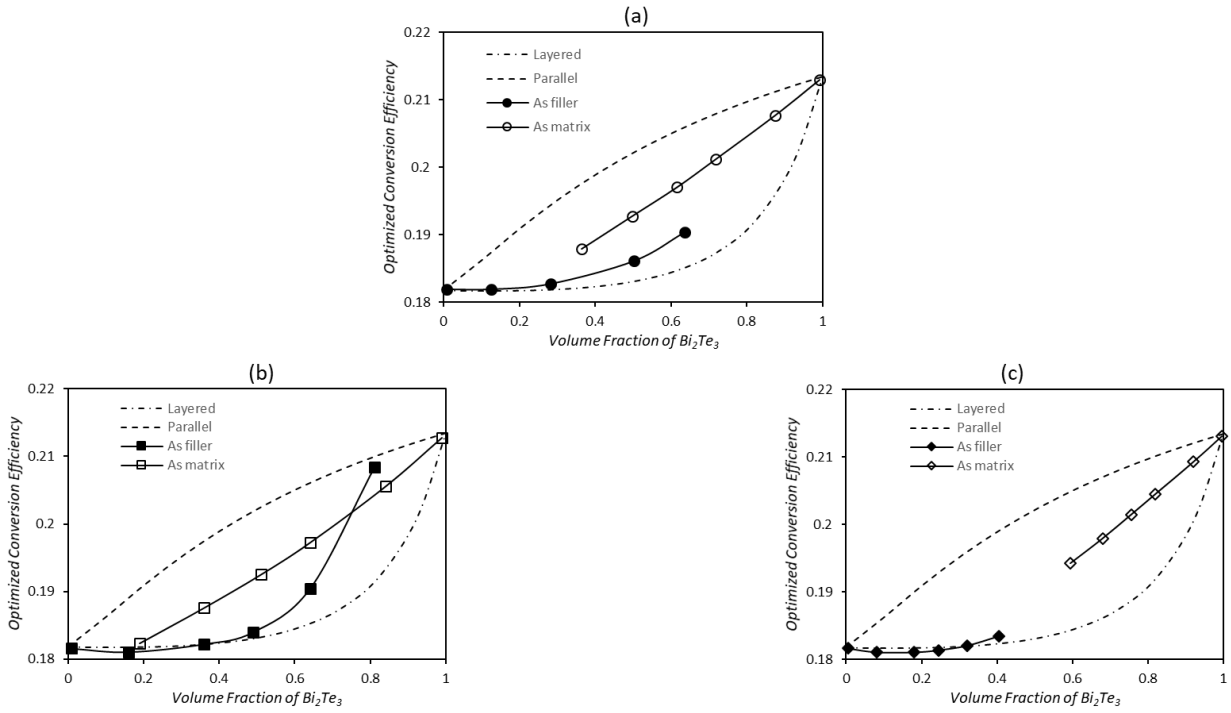

Figure 5.14. Conversion efficiencies of composite with three different filler shapes, (a) round, (b) square, and (c) diamond versus volume fraction of Bi_2Te_3 both as fillers and matrix alone with the theoretical upper and lower bounds.

5.5 SUMMARY

In this chapter, we developed a finite element model of a thermoelectric composite with two dimensional fillers. The model was verified with well-established solutions and proved to be reliable. With the model, we solved for the effective behaviors that were very close to those in single-phase materials. We further analyzed the overall conversion efficiency and showed that the effective thermoelectric properties are well-defined, and the effective thermoelectric figure of merit does correlate with the thermoelectric conversion efficiency. Thus, this method was proved to be effective in evaluating the performance of thermoelectric composites with 2D fillers.

Chapter 6. ACCELERATE THE SEARCH OF BETTER THERMOELECTRIC COMPOSITE BY MACHINE LEARNING

6.1 INTRODUCTORY REMARKS

In the previous chapter, a finite element method was developed and proven effective on estimating the effective figure of merit of thermoelectric composites. Although no improved figure of merit found with the material combination used in the previous chapter, there are many more possible combinations that not yet been tested and could lead to an improved figure of merit. But finite element analysis (FEA) is a time-consuming and resource intensive process, it is not practical to test each case with FEA.

Machine learning techniques have been applied to exploit material databases and discover trends and mathematical relations for material design[86]. There are two major categories of machine learning algorithms: supervised learning and unsupervised learning. Supervised learning algorithms build a mathematical model that maps the input data to the desired outputs. It has been employed in establishing the process-composition-property relation for metals[87,88] and predicting polymer composites properties based on the composition-properties database[86,89]. Unsupervised learning algorithms take a set of data that contains only inputs, and find structure in the data, like grouping or clustering of data points, which is used to reduce the complexity of parameter set to address the need of material design[90].

In this study, we propose a machine learning methodology for identifying the more promising combinations and reducing the need of using FEA; the methodology is outlined in Section 6.2. An unsupervised learning algorithm is first applied to find the similarities among all the possible combinations, which helps reduce the number of combinations needed to be analyzed by FEA (Section 2.2). The results of the FEA are then used to train a supervised machine learning mode that predicts effective thermoelectric figure of merit based on the combination attributes (Section 2.4). We demonstrate the strength of the proposed method with the 16 state-of-the-art p-type thermoelectric materials in Section 6.3.

6.2 METHODOLOGY

In the presence of a large number of possible combinations, the key research question is how to narrow down to a smaller set of more promising combinations that could lead to improved effective figure of merit. A machine-learning-based method is proposed to exploit the material database, as shown in Figure 6.1 and outlined in the following steps:

(1) Preprocess the material data and list all the possible combinations of materials from the material database;

(2) Group combinations according to their similarity by using an unsupervised machine learning algorithm;

(3) Select combinations from every group and use the finite element analysis (FEA) approach developed in the last chapter to calculate the effective properties of those combinations, so as to obtain the results across the whole spectrum of all the possible combinations;

(4) Train a machine learning model with the effective properties generated by FEA;

(5) Use the model to predict the effective figure of merit of all the possible combinations that maps the more promising combinations;

(6) Calculate the more promising combinations with FEA to check if those combinations lead to improved figure of merit;

(7) Increase the accuracy of the model by training the model with newly generated data;

(8) Repeat steps 5~7 until all the promising combinations are tested.

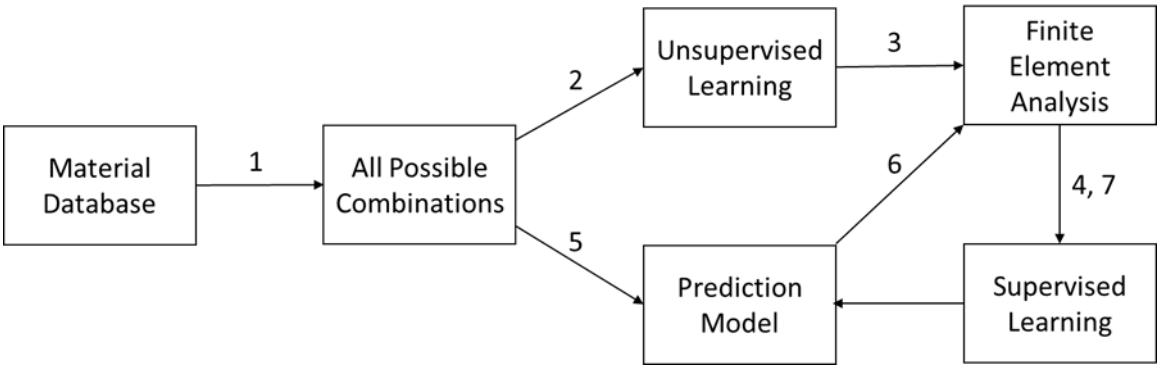

Figure 6.1. Framework of the identification of machine-learning-based high thermoelectric performance composites identification

6.2.1 *Preprocessing the Material Data*

In order to calculate the effective properties, the material properties of the two mixed materials must be defined at the same temperature. However, not all the materials are necessarily tested under the same temperature. Therefore, in step 1 of the proposed framework a linear interpolation function is used to estimate material properties between two tested temperatures, so that we may have material data defined at the same temperature. The material properties of each material are estimated from 300K to 2000K in increments of 25K as long as the data range of that material covers that temperature.

After all the material properties are lined up at each temperature, all the available material at the same temperature are paired into combinations of matrix and fillers. Thus, we have a complete list of all possible combinations of two materials in the available material data.

6.2.2 *Unsupervised machine Learning — Cluster Analysis*

After we have the full list of possible combinations, the next step is to select a small set of combinations that will be used in the initial finite element analysis. Due to the high computational cost of finite element analysis, this set cannot be too large. At the same time, this set of combinations needs to be able to represent the full set of combinations. If the selected set only represents part of the possible combinations, the model created by the supervised machine learning can have very poor accuracy on the other part of the possible combinations. Therefore, an unsupervised machine learning, cluster analysis, is proposed to aid the initial set selection. The cluster analysis is a branch of machine learning that groups the data by identifies the commonalities in the un-labelled data. That is, all the combinations in a group or cluster, should have similar matrix properties, filler properties, as a result, similar effective figure of merit. By pick one or two combination from each cluster, we should be able to have a small but representative sub-set of combinations.

6.2.2.1 K-Means Clustering

K-means clustering[91], one of the most popular methods for cluster analysis is used in this study. K-means clustering aims to partition n observations ($x_1, x_2 \dots, x_n$), where each observation is a d-

dimensional real vector, into k clusters $S = \{S_1, S_2, \dots, S_k\}$ in which each observation belongs to the cluster with the nearest mean, or cluster centroid m_i, so as to minimized the within-cluster sum of squares (WCSS).

$$min \sum_{i=1}^{k} \sum_{x \in S_i} ||x - m_i||^2 \tag{6.1}$$

The most common algorithm is by using an iterative refinement technique. An initial set of k means $m_1^{(1)}, \dots, m_k^{(1)}$ is randomly generated in the beginning, and the algorithm proceeds by alternating between two steps:

Assignment step: Assign each observation to the cluster whose mean has the least squared distance

$$S_i^{(t)} = \left\{ x_p : \left\| x_p - m_i^{(t)} \right\|^2 \leq \left\| x_p - m_j^{(t)} \right\|^2 \ \forall j, 1 \leq j \leq k \right\} \tag{6.2}$$

Update step: Calculate the new means to be the centroids of the observations in the new clusters

$$m_i^{(t+1)} = \frac{1}{\left| S_i^{(t)} \right|} \sum_{x_j \in S_j^{(t)}} x_j \tag{6.3}$$

The algorithm is converged when the assignments no longer change. The algorithm is demonstrated in Figure 6.2. The algorithm does not guarantee convergence to the global minimum, and the results depend on the initial set of means. To find the global optimum, it is common to run it multiple times with different starting conditions.

Figure 6.2. Demonstration of the k-means algorithm

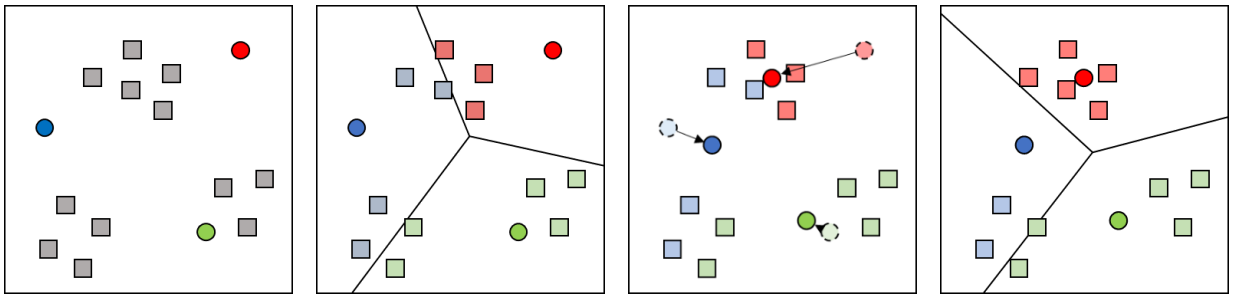

1. k initial means (colored dots) are randomly generated within the data domain.

2. Every observation is assigned to the nearest mean to form k clusters.

3. The centroid of the k clusters becomes the new mean.

4. Step 2 and 3 are repeated until the assignments no longer change.

6.2.2.2 Elbow Method

As it was mentioned that K-means algorithm groups observations into k clusters, but how can we determine what is the appropriate number of k for each specific dataset? One method to validate the number of clusters is the elbow method[92]. The idea of the elbow method is to run k-means clustering on the dataset for a range of values of k, and for each value of k calculate the within-cluster sum of squares (WCSS). Then the WCSS is plotted against the number of clusters. The WCSS decreases more dramatically as adding the first few clusters, which means that each added cluster helps explain a lot of variance. But at some point the margin will drop, giving an angle in the graph. In other words, after that point adding another cluster does not give much better modeling of the data, leading to the "elbow criterion." Although this "elbow" cannot always be unambiguously identified, the plot of WCSS against the number of clusters is always a good reference for k value selection.

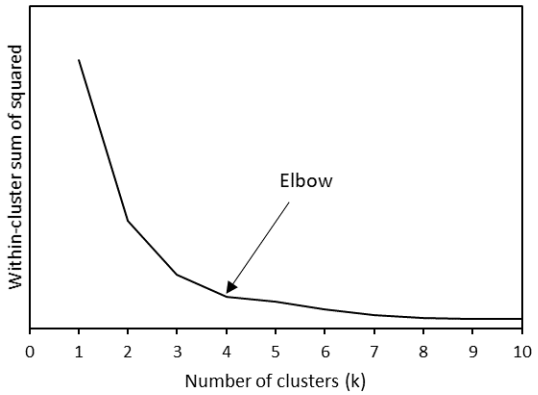

Figure 6.3. K-means within-clustering sum of squared against number of clusters

6.2.3 *Finite Element Analysis*

The effective properties of the selected combinations are then calculated through the finite element analysis developed in the previous chapter. Each pair of two materials is tested with different volume fractions, and three effective properties, effective electrical conductivity, thermal conductivity, and Seebeck coefficient are evaluated under two separated finite element models (relevant details described in Chapter 5).

6.2.4 *Supervised Machine Learning — Regression Analysis*

The end goal of the machine learning framework is to identify the most promising combinations that could possibly result in an improved effective figure of merit. A supervised learning algorithm is used to develop a model that maps the combination attributes to the effective figure. Ridge regression is employed as the supervised learning algorithm, which takes all the combination attributes, which include temperature, matrix and fillers' material properties and volume fraction of the fillers, as input features and the effective figure of merit calculated by the finite element analysis as output.

6.2.4.1 Ridge Regression Analysis

In a regression analysis, a learning algorithm seeks a function $h_\theta: X \to Y$, where X is the input space and Y is the output space. The function h_θ with θ_j as its parameters is an element of some space of possible functions H, usually called the hypothesis space. In order to measure how well a function fits the training data, a cost function $C: Y \times Y \to \mathbb{R}^{\geq 0}$ is defined. The most common approach is ordinary least squares linear regression. For training m example (x_i, y_i), the learning algorithm seeks a function that minimize the cost function defined as

$$C = \frac{1}{2m}\sum_{i=1}^{m}(h_\theta(x_i) - y_i)^2 \tag{6.4}$$

However, the least squares method is very sensitive to outliers and it has the tendency to overfit data. To avoid overfitting, a regularization term can be included in this minimization:

$$C = \frac{1}{2m}\left[\sum_{i=1}^{m}(h_\theta(x_i) - y_i)^2 + \lambda \sum_{j=1}^{n}\theta_j^2\right] \tag{6.5}$$

This is known as L_2 regularization, and the model which uses L_2 regularization is called Ridge Regression[93]. The regularization term introduces squared magnitude of parameters as a penalty to the large parameters and avoid overfitting. However, if λ is very large then it will add too much weight and will lead to under-fitting. Having said that it is important how λ is chosen.

6.2.4.2 Performance Measures

In order to adjust the model and use the model with confidence, we need to measure the performance of our regression model, that is, how accurately the model predicts results. A few

statistical tools like mean square error (MSE) and coefficient of determination[94] also called R^2 are commonly used to evaluate the performance of the regression model.

The **MSE** measures the average squared difference between the estimated values and what is estimated. Since MSE is the second moment of the error, it incorporates both the variance of the model and its bias.

$$MSE = \frac{1}{m}\sum_{i=1}^{m}(h_\theta(x_i) - y_i)^2 \tag{6.6}$$

The **R^2** gives us a measure of percentage of variance (how far observed values differ from the average of predicted value) is explained by the model. Value of R^2 normally ranges from 0 to 1, where a value of 1 means that the model explains all the variation in predicted variable around its mean. The R^2 formula is expressed as,

$$R^2 = 1 - \frac{\sum(y_i - h_\theta(x_i))^2}{\sum(y_i - \overline{y})} \tag{6.7}$$

where $\overline{y}$ is the mean of the observed data. The other two terms often mentioned when it comes to model evaluation are underfitting and overfitting[95].

Underfitting occurs when a model cannot capture the underlying trend of the data and comes with very high MSE and low R^2 .Underfitting is often a result of an excessively simple model.

Overfitting occurs when a model captures the noise of the data and fits the data too well. The model can capture accurately on the training data but poorly on the new data. Overfitting is often a result of an excessively complicated model and it can be prevented by fitting multiple models and using cross-validation to compare their predictive accuracies on test data.

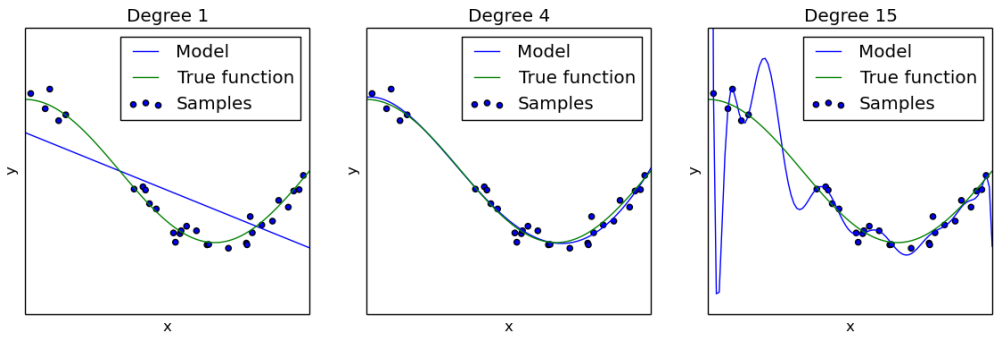

Figure 6.4. Demonstration of the problem of underfitting (left) and overfitting (right)

6.2.4.3 K-Fold Cross-validation

Cross-validation is one of the most useful techniques to the performance of the model. There are many different types of cross-validation, and the most common one would be k-fold cross-validation[96].

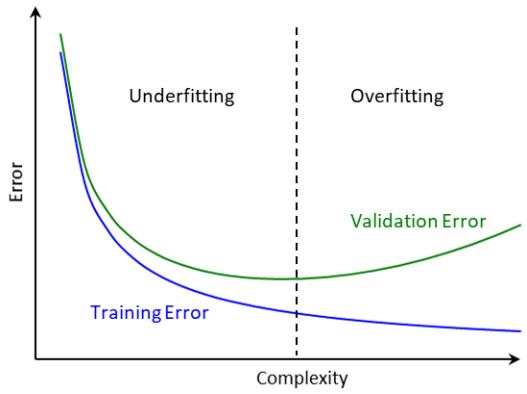

Figure 6.5. Scheme for the error as a function of the complexity of the calibration model

In k-fold cross-validation, the original dataset is split into k different subsets (the so-called "folds") where 1 fold is retained as test set, and the other k-1 folds are used for training the model. E.g., if we set k equal to 4, 3 different subsets of the original training set would be used to train the model, and the 4th fold would be used for evaluation. After 4 iterations, we can eventually calculate the average error rate of the model, which gives us an idea of how well our model generalizes.

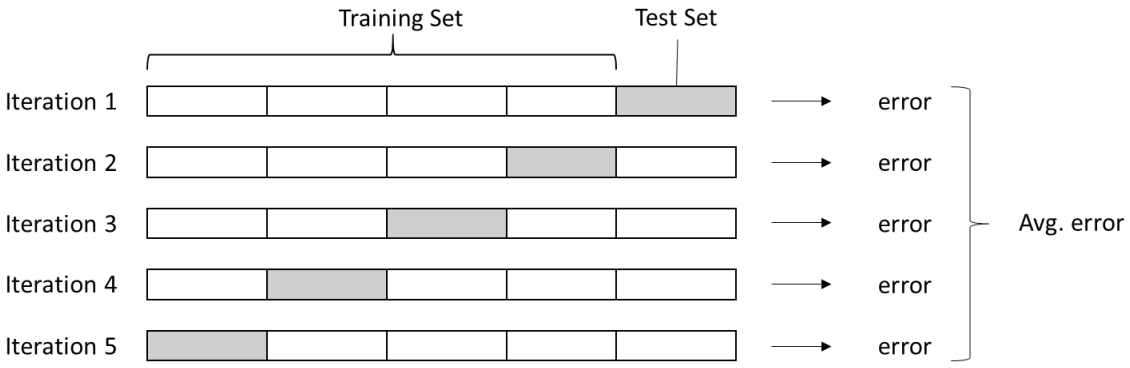

Figure 6.6. Scheme of k-fold cross-validation with k equals to 5

6.2.4.4 General Workflow of Supervised Learning

While there are many machine learning algorithms for supervised learning, most of them use the same workflow for obtaining the model. The steps for supervised learning are: (1) Collect the data and preprocess the data into clean input and output matrix. (2) Choose an algorithm and a model, a hypothesis, from the algorithm's hypothesis space. (3) Split the data into training set and test set, or into k subsets if using k-fold cross-validation. (4) Train the model with selected algorithm and training data set. (5) Evaluate the performance of the model by cross-validation. (6) If it shows signs of underfitting or overfitting, adjust the model, algorithm parameters or select a different learning algorithm and repeat steps 2 ~ 6 until achieving desirable accuracy. The workflow diagram is shown in Figure 6.7.

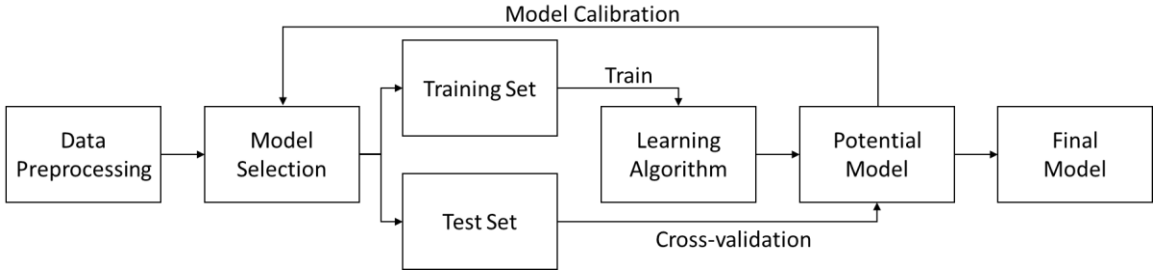

Figure 6.7. The workflow for training a supervised machine learning model

6.3 Searching the Improved Thermoelectric Figure of Merit by Machine Learning

6.3.1 *Data Preprocessing*

In order to study the possible combinations of thermoelectric composites, the stat-of-the art p-type thermoelectric materials[83] have been considered. Seebeck coefficient, thermal conductivity, and electric conductivity as functions of temperature of the 16 p-type thermoelectric are shown in the left column of Figure 6.8. Most of the materials were tested under a wide temperature range of 300K-900K, and some went up to 1200K while bismuth tellurides were only tested within 300K-525K. Although most of the materials' testing range is overlying to each other, their test temperature is not lined up, and many even have different test interval. To lineup data points, a linear interpolation function is used to estimate the material properties at every 25K, starting with

300K, as long as the data range of that material covers that temperature, the processed data is shown in the right column of Figure 6.8.

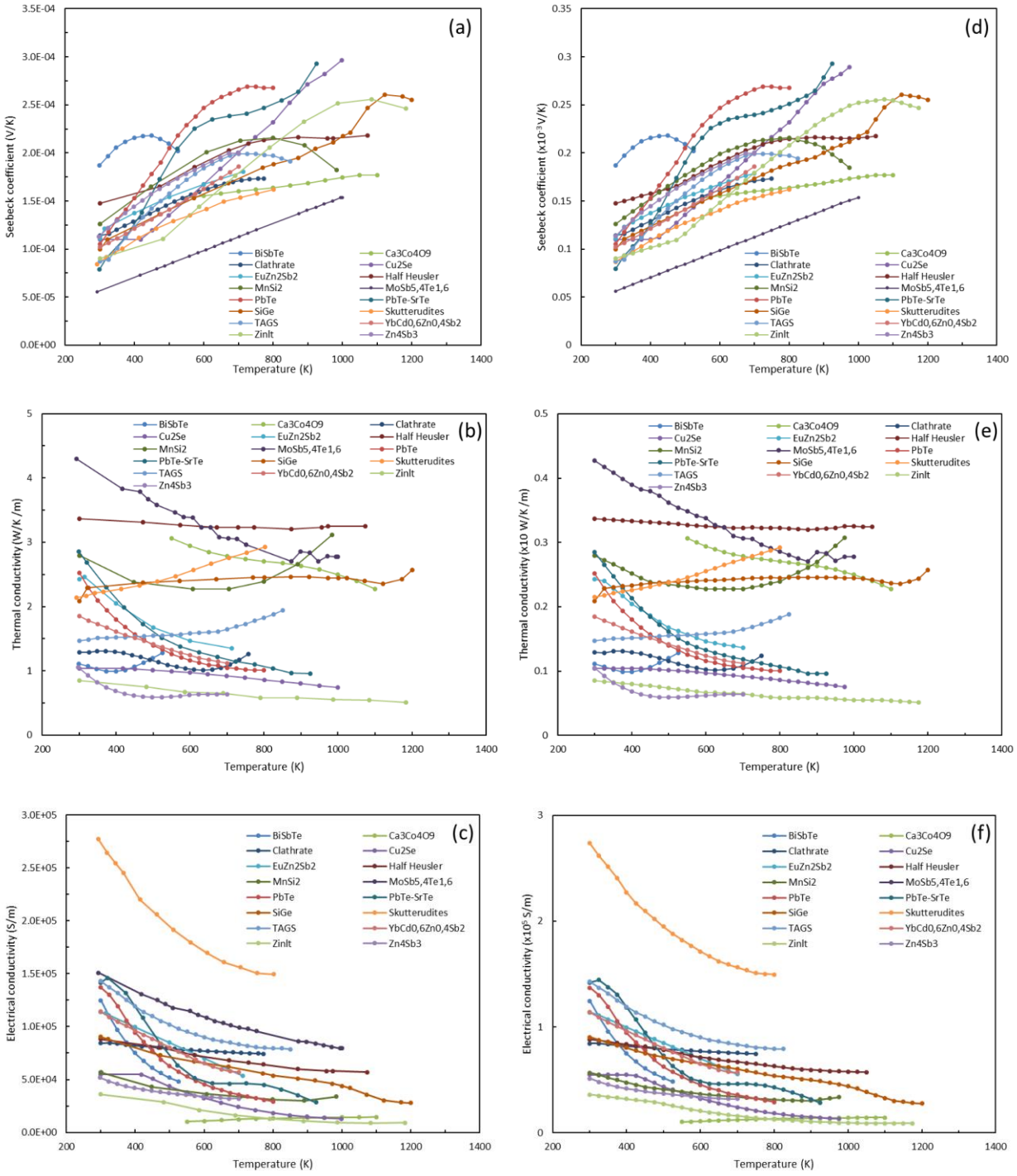

Figure 6.8. The raw data (left column) and the processed data (right column) of the state-of-the - art p-type thermoelectric materials. Material data is provided by Gerald Jeffrey Snyder, California Institute of Technology, USA[83].

After all the data points are lined up to each other, we can start to search for all the possible combinations. At each temperature, we list all the ways to assign available materials to matrix material and filler material. All the possible combinations are shown in Figure 6.9 where the horizontal axis denotes the material as a matrix, and the vertical axis denotes the material as filler. The diagonal blocks, the white blocks, represent combinations of the same material which does not need to be analyzed by FEA. Each gray block represents a combination of two different materials. Within every block, the horizontal axis denotes the temperature because materials have different properties at a different temperature, and the vertical axis denotes the volume fraction of the fillers. Each black pixel represents an unavailable combination at that certain temperature. Each gray pixel represents an available combination that can be analyzed by FEA, as shown in the zoom-in in Figure 6.10. In total, there are 4,496 possible material pairs, not accounting for volume fraction, and it is impossible to analyze all of them. Therefore, a machine learning methodology is proposed to assist this process.

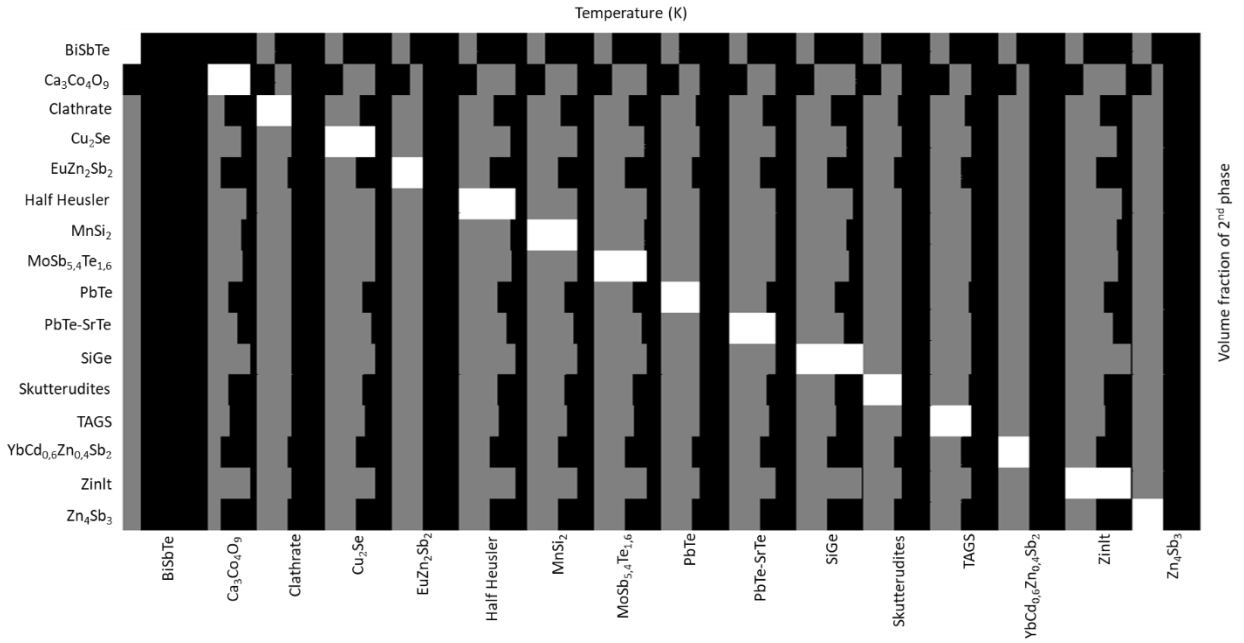

Figure 6.9. The map of the possible combinations (gray) where the horizontal axis denotes the material as matrix and temperature, and the vertical axis denotes the material as filler and the volume fraction of the filler.

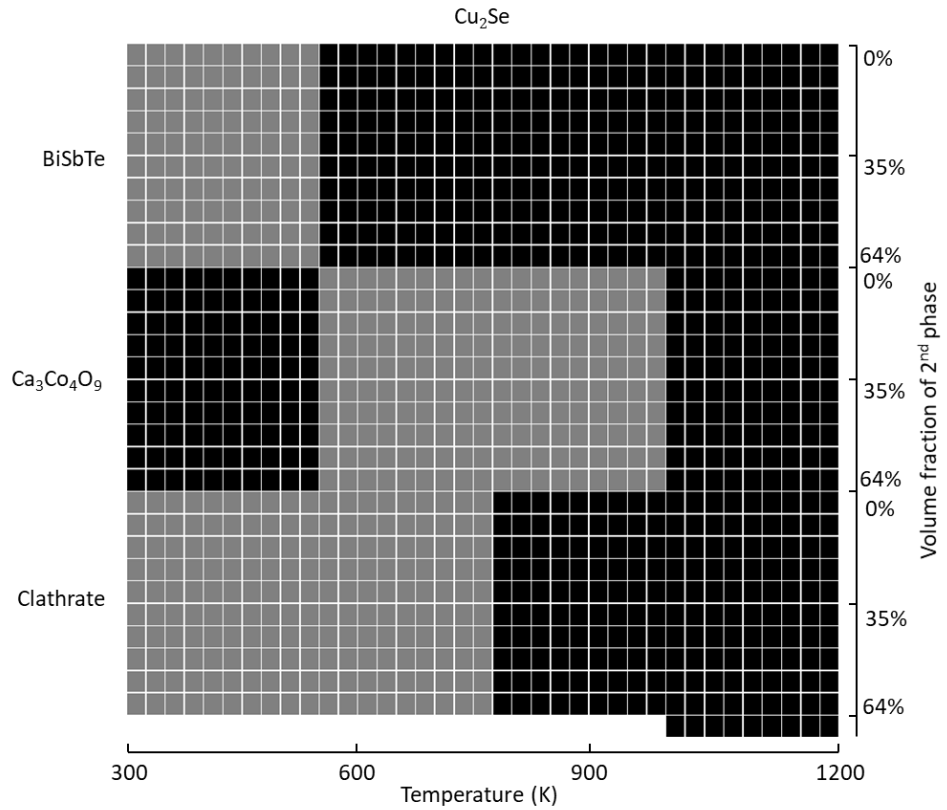

Figure 6.10. The zoom-in to a portion of Figure 6.9 where each pixel represents an unavailable combination (black), available combination (gray), and a combination of the same material (white).

Before the clustering and regression analysis all the features in the data need to be normalized into the same scale. Normalization is especially important for k-means clustering because k-means seeks to minimize the distance between the observations and the centroid within clusters. If one of the features has a much larger scale than others, then this feature becomes the only driver of distance which leads to poorer convergence[97]. A good thermoelectric material usually has very good electric conductivity at the scale of 10^6. The scale of the Seebeck coefficient is usually at 10^{-4}. Without normalization the result of the clustering analysis will align only with electric conductivity and other attributes will be ignored. Normalization is also a good practice for linear regression. Since most regression algorithms minimize cost function by gradient descent method, normalization improves the conditioning of the optimization problem and speeds up convergence[98].

6.3.2 *Clustering Analysis*

It is obvious that many materials have many similarities in one of their thermoelectric properties at a certain temperature range, as shown in Figure 6.8, but it is very hard to see if they are similar in all thermoelectric properties (even harder to see the similarity of material combinations). K-means clustering helps perceive the similarity in the 7-dimensional space: Temperature, matrix Seebeck coefficient, matrix thermal conductivity, matrix electric conductivity, filler Seebeck coefficient, filler thermal conductivity, and filler electric conductivity. Figure 6.11 shows the WCSS against the number of clusters. The WCSS decreases more dramatically as adding the first 25 clusters then the margin gradually decreases as more clusters are added. The elbow in this analysis is at about $k = 50$, that is, within these 50 clusters all the combinations have a certain degree of similarity. Thus, we can reduce the need of FEA from 4496 all possible combinations to 50 more distinct combinations. And we can easily expand the number when more training examples are needed for regression analysis. Each combination is analyzed with 6 different volume fractions, 0.78%, 7.07%, 19.64%, 38.48%, 50.27%, and 63.62% in the FEA. Therefore 300 training examples are generated for the initial test.

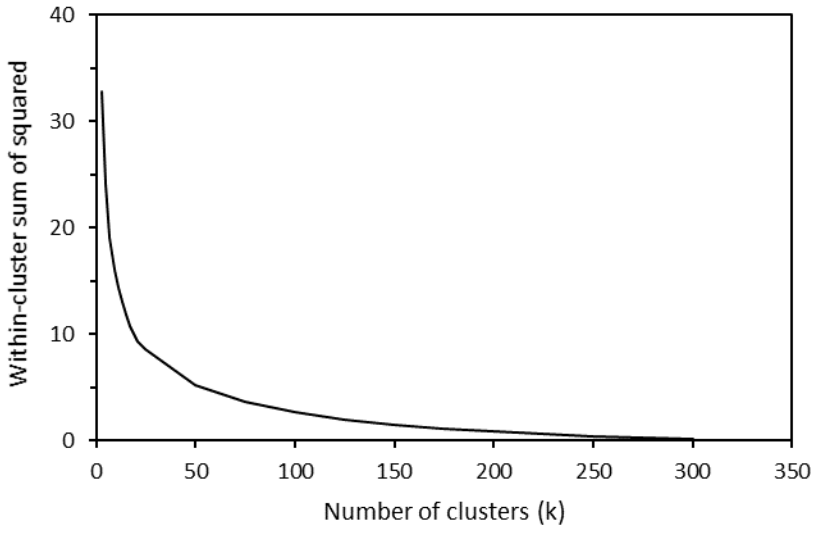

Figure 6.11. The within-cluster sum of squared against number of clusters from the clustering analysis of the thermoelectric material combinations.

6.3.3 *Regression Analysis*

The regression analysis is carried out with ridge model and three different hypothesis functions, 1st, 2nd, and 3rd degree polynomials. A parametric study of the regularization coefficient λ versus R^2 and MSE has been performed on each of these three cases. Figure 6.12 and Figure 6.13 show the results of this parametric study, and it is clear that the R^2 score of the 1st and 2nd degree polynomials are lower than the 3rd degree polynomial. Their MSR are higher than the 3rd degree polynomial at the same time, which means that the 1st and 2nd degree polynomials are too simple to catch the more complicated behavior of the thermoelectric composite. With the 3rd degree polynomial, the training score can be improved by decreasing the value of λ, that is to increase the complexity of the model. But the cross-validation score can only be improved to a certain degree and starts to drop as the model gets further complex and shows the sign of overfitting. This parametric study suggests that a 3rd degree polynomial with a value of $\lambda \cong 1E-7$ could yield good calibrate model.

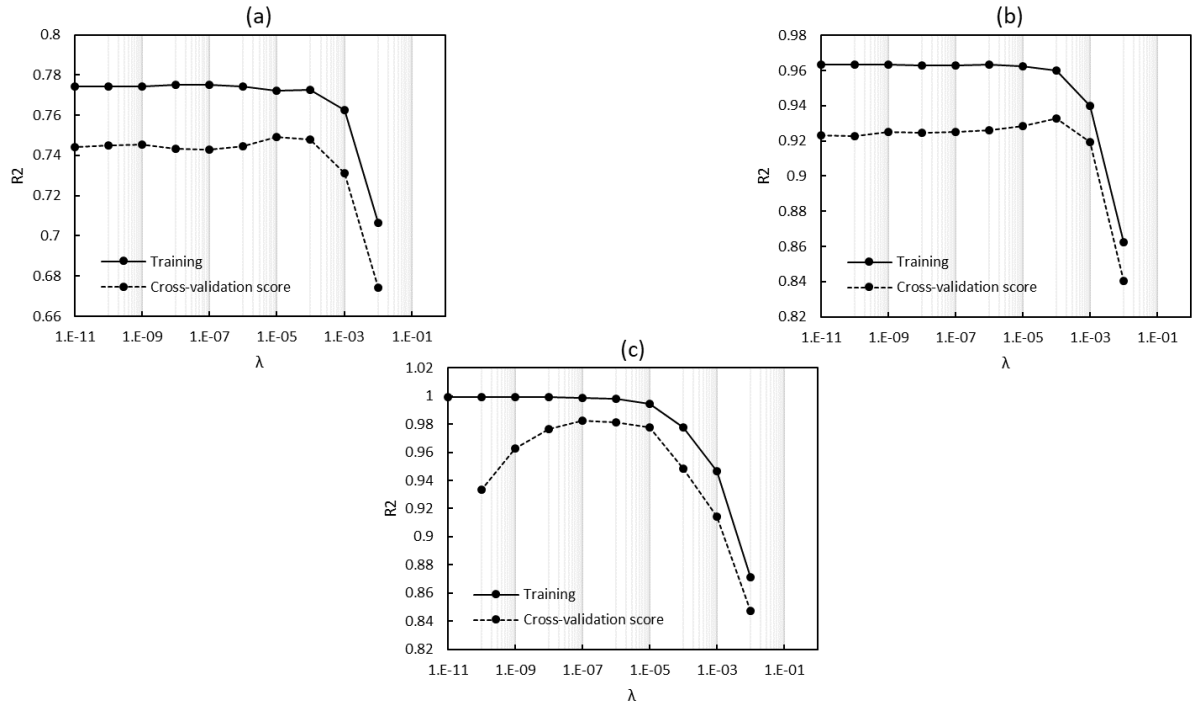

Figure 6.12. The R^2 scores of models with (a) 1st degree, (b) 2nd degree, and (c) 3rd degree polynomials against regularization coefficient λ.

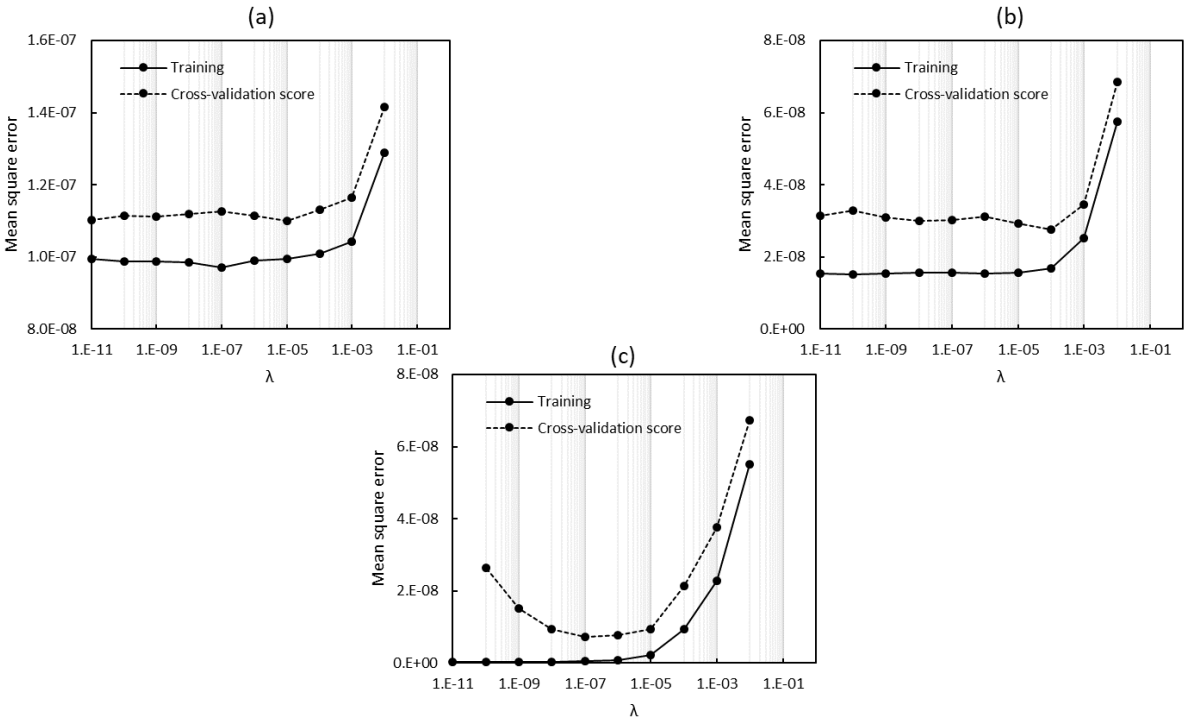

Figure 6.13. The mean square errors of models with (a) 1st degree, (b) 2nd degree, and (c) 3rd degree polynomials against regularization coefficient λ.

The accuracy of the model can be further improved by training the model with more training examples. Figure 6.14 shows that the accuracy of the model is increasing as we are adding more training examples. Each point represents the number of material combination of 25, 50, 100, 150, 200, 250 respectively. The cross-validation score stops increasing while the number of material combination reach 150, that is about 800 training examples, and the score is not much higher than the score of the model trained by 100 material combinations with 500 training examples. That has been said that with only 100 out of 4496 of all possible combinations we can train a model with satisfactory accuracy.

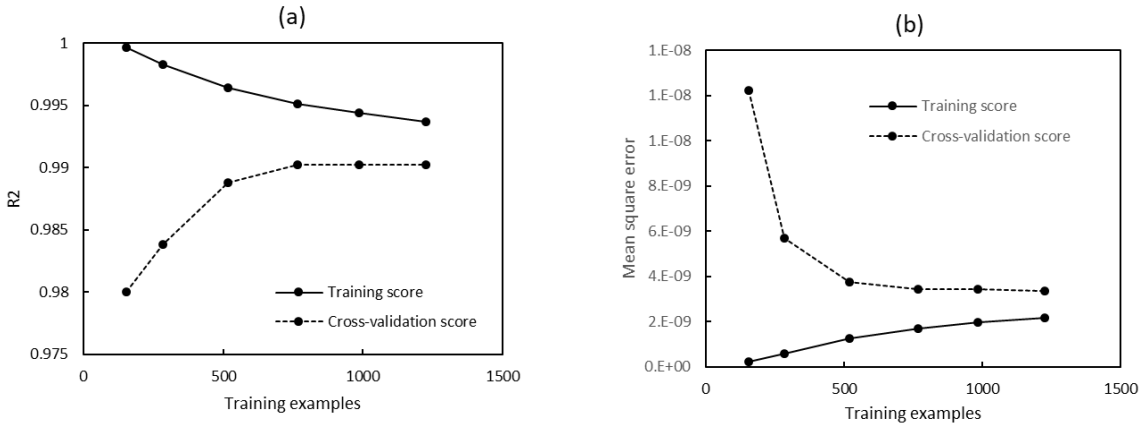

Figure 6.14. (a) The R^2 score and (b) mean square error of the training and cross-validation set against the number of training examples.

The machine learning model is then used to estimate the effective figure of merit of all the possible combinations. Figure 6.15 shows the estimated figure of merit of all the possible combination where the brighter gray denotes the higher figure of merit. All the high effective figure of merit appears to be the combination of BiSbTe with the other materials. This is because BiSbTe is hitherto the best performing material. It is not clear if there is any improvement in figure of merit obtained. Figure 6.16 shows the ratio of the estimated figure of merit to the higher component figure of merit. Needless to say, the ratio of the combination with the same materials is one, shown as the diagonal blocks. Any pixel shown with the color brighter than the diagonal blocks denotes the ratio greater than 1, indicating that an improved effective figure of merit might be achieved with that combination. While a machine learning algorithm only generates an approximate model, not the exact model, the output of a machine learning model can only be seen as estimations and needs to be further verified. Unfortunately, the effective figure of merit of those combinations are proved not better than the highest component figure of merit.

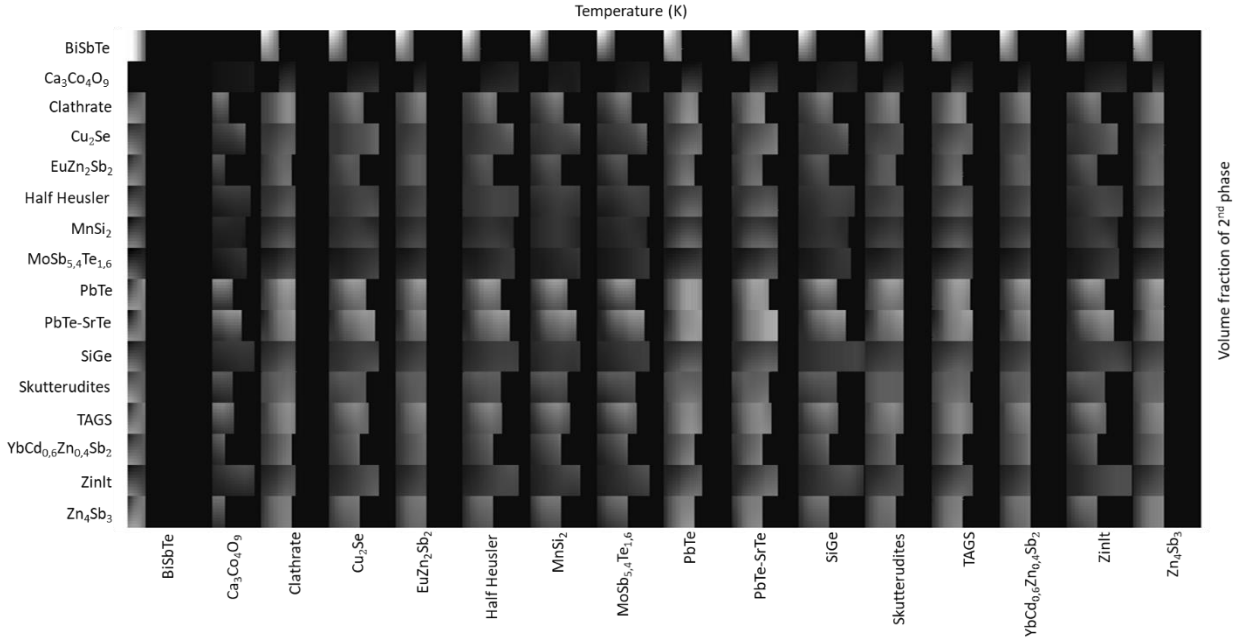

Figure 6.15. The effective figure of merit Z of all the possible combinations estimated by the regression model, where the brighter gray denotes the higher figure of merit.

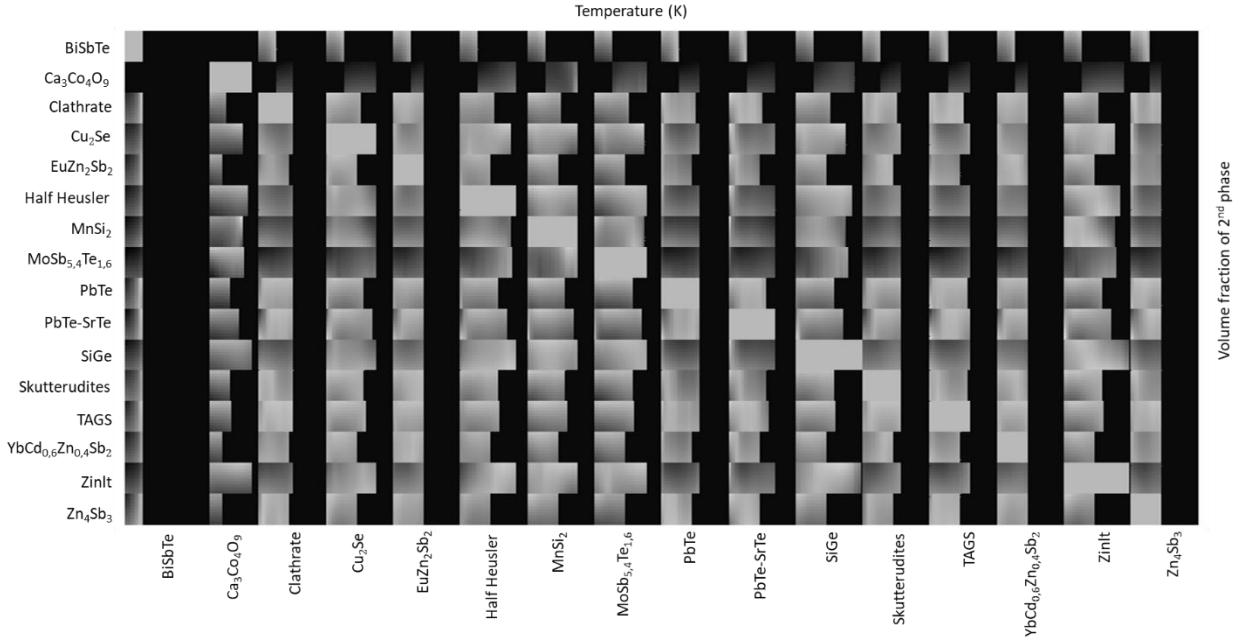

Figure 6.16. The ratio of effective figure of merit Z to the higher component figure of merit of all the possible combinations estimated by the regression model, where the brighter gray denotes the higher ratio.

6.4 SUMMARY

In conclusion, we have developed a machine learning methodology for identifying the more promising combinations while reducing the computational cost of FEA. It is shown that with only 100 out of the 4496 possible material combinations are needed in FEA to obtain a satisfactory accurate machine learning model. That has been said that this method reduced more than 95% of the cost from FEA. Through this study, we found no improved effective figure of merit from the combinations of the 16 state-of-the-art p-type thermoelectric materials. Nonetheless, the developed finite element method and machine learning methodology are proved to be effective in estimating the effective behavior of two-dimensional thermoelectric composites that can greatly accelerate the new composite discovery and design.

Chapter 7. CONCLUSIONS AND FUTURE WORKS

7.1 CONCLUSIONS

Motivated by Yang's work[1,81], we defined a new set of effective properties for thermoelectric composite with periodic 1D microstructure in Chapter 2. Through the analysis and calculation, we conclude that (1) the effective behavior of the 1D thermoelectric composites are the same as single phase thermoelectric materials; (2) this set of newly defined effective properties cam be used to calculate the composite's thermoelectric performance; (3) the effective figure of merit of the composite could not exceed both of its constituents; but (4) the effective power factor could be greatly enhanced. In other words, even though the maximum conversion efficiency cannot be improved, the maximum power output can be enhanced. This becomes especially valuable when designing a thermoelectric device which will be used in a space restricted condition. This set of effective properties can serve as a simple tool to find the balance between enhancing power output and keeping conversion efficiency in thermoelectric device design.

We extended our study from composite with periodic 1D microstructure to functionally graded thermoelectric material to seek an improved total conversion efficiency by matching compatibility factor with relative current density in Chapter 3. We show that the efficiency gain is insignificant due to the fact that the effective figure of merit is sacrificed when matching the compatibility factor and relative current density.

In Chapter 4, as we moved our study to the thermoelectric composites with periodic microstructure in 2D, we found some drawback on applying asymptotic homogenization method: (1) there is uncertainty on choosing a crucial parameter that governs the results of this analysis; (2) it is not computationally cheap, each case need several iterations; (3) the effective properties are ill-defined, and does not directly correlate with the conversion efficiency; (4) it can only be used in certain special cases.

Thus, we developed a direct finite element method as an alternative way in Chapter 5. This model was verified with well-established solutions and proved to be reliable. We proved that with enough number of repeating cells, we can simulate the behavior of a homogenized composite. With the model we solved for the effective behaviors that were very close to those in single-phase

materials. The effective properties we defined do correlate with the thermoelectric conversion efficiency and can be used to estimate the performance of the composite.

Although the direct finite element method was proved to be effective in evaluating the performance of thermoelectric composites, it is still not practical to test very possible combinations with the finite element method. Therefore, we proposed a machine learning methodology for identifying the more promising combinations in Chapter 6. It is shown that the need of using FEA is greatly reduced. Only 5% of the all possible combinations are needed to be analyzed by FEA to obtained satisfactory accurate machine learning model. Although there is no improved effective figure of merit found in this study, this study shows that the proposed methodology can greatly accelerate the new composite discovery and design.

7.2 FUTURE WORKS

We have demonstrated how effective a directive finite element method is on solving the thermoelectric problem with 2D periodic microstructure. This method can be extended to 3D and more complex microstructure in a straightforward way. We also demonstrated that machine learning models can be used to estimate the effective figure of merit of the thermoelectric composite. These models can be trained with more different cases, composites with different filler geometry, different dispersion, and be used not only to estimate figure of merit but also all the thermoelectric properties. The extended scope will provide with us more insight into the effective behavior of thermoelectric composites for their design and optimization.

BIBLIOGRAPHY

1. Yang, Y., Ma, F. Y., Lei, C. H., Liu, Y. Y. & Li, J. Y. Nonlinear asymptotic homogenization and the effective behavior of layered thermoelectric composites. *J. Mech. Phys. Solids* **61**, 1768–1783 (2013).
2. Rowe, D. M. CRC Handbook of Thermoelectrics: Macro to Nano (CRC/Taylor and Francis, Boca Raton, FL). (2006).
3. Houston, W. V. Electron theory of thermoelectric effects. *J. Appl. Phys.* **12**, 519–529 (1941).
4. Callen, H. B. *Thermodynamics: An Introduction to the Physical Theories of Equilibrium Thermostatics and Irreversible Thermodynamics*. (Wiley, 1960).
5. Disalvo, F. J. Thermoelectric Cooling and Power Generation. **703**, 703–706 (2013).
6. Andersen JR. Thermoelectric air conditioner for submarines. *Adv Energy Conv* **2**, 241–248 (1962).
7. Marlow, R., Buist, R. J. & Nelson, J. L. System aspects of thermoelectric coolers for hand held thermal viewers. Marlow Industries, Inc. Garland, TX, US. (1982).
8. Riffat, S. B. & Ma, X. Thermoelectrics: A review of present and potential applications. *Appl. Therm. Eng.* **23**, 913–935 (2003).
9. Sarbu, I. & Dorca, A. A comprehensive review of solar thermoelectric cooling systems. *Int. J. Energy Res.* **42**, 395–415 (2018).
10. Shashkov P., Khomutov G., Yerokhin A., U. S. (12) UnIted States Patent. **2**, 0–3 (2012).
11. Welling Jr, T. E. & others. The effect of thermoelectric cooler mounting orientation on cooling efficiency. Aes-vol. 37. *Proc. ASME Adv. Energy Syst. Div. ASME* 303–307 (1997).
12. Yang, J. & Caillat, T. Thermoelectric Materials for Space. *MRS Bull.* **31**, 224–229 (2006).
13. Yang, J. Potential Applications of Thermoelectric Waste Heat Recovery in the Automotive Industry. 1–5 (2005).
14. Aranguren, P., Astrain, D. & Pérez, M. G. Computational and experimental study of a complete heat dissipation system using water as heat carrier placed on a thermoelectric generator. *Energy* **74**, 346–358 (2014).
15. Luo, Q. *et al.* A Thermoelectric Waste-Heat-Recovery System for Portland Cement Rotary Kilns. *J. Electron. Mater.* **44**, 1750–1762 (2015).
16. Kuroki, T. *et al.* Research and Development for Thermoelectric Generation Technology Using Waste Heat from Steelmaking Process. *J. Electron. Mater.* **44**, 2151–2156 (2015).
17. Kaibe, H., Makino, K., Kajihara, T., Fujimoto, S. & Hachiuma, H. Thermoelectric generating system attached to a carburizing furnace at Komatsu Ltd., Awazu Plant. *AIP Conf. Proc.* **1449**, 524–527 (2012).
18. Kraemer, D. *et al.* Photovoltaic-thermoelectric hybrid systems: A general optimization methodology. *Appl. Phys. Lett.* **92**, (2008).
19. Tritt, T. M., Böttner, H. & Chen, L. Thermoelectrics: Direct Solar Thermal Energy Conversion. *MRS Bull.* **33**, 366–368 (2008).
20. Pu, X., Hu, W. & Wang, Z. L. Toward Wearable Self-Charging Power Systems: The Integration of Energy-Harvesting and Storage Devices. *Small* **14**, 1–19 (2018).
21. Stordeur, M. & Stark, I. Low Power Thermoelectric Generator - self-sufficient energy supply for micro systems. 575–577 (1997).

22. Kim, S. J., We, J. H. & Cho, B. J. A wearable thermoelectric generator fabricated on a glass fabric. *Energy Environ. Sci.* **7**, 1959 (2014).
23. Champier, D. Thermoelectric generators: A review of applications. *Energy Convers. Manag.* **140**, 167–181 (2017).
24. Rojas, J. P. *et al.* Review—Micro and Nano-Engineering Enabled New Generation of Thermoelectric Generator Devices and Applications. *ECS J. Solid State Sci. Technol.* **6**, N3036–N3044 (2017).
25. Harman, T. C. & Honig, J. M. *Thermoelectric and Thermomagnetic Effects and Applications*. (McGraw-Hill, 1967).
26. Shakouri, A. Recent Developments in Semiconductor Thermoelectric Physics and Materials. *Annu. Rev. Mater. Res.* **41**, 399–431 (2011).
27. Li, J.-F., Liu, W.-S., Zhao, L.-D. & Zhou, M. High-performance nanostructured thermoelectric materials. *NPG Asia Mater.* **2**, 152–158 (2010).
28. Koumoto, K., Wang, Y., Zhang, R., Kosuga, A. & Funahashi, R. Oxide Thermoelectric Materials: A Nanostructuring Approach. *Annu. Rev. Mater. Res.* **40**, 363–394 (2010).
29. Pichanusakorn, P. & Bandaru, P. Nanostructured thermoelectrics. *Mater. Sci. Eng. R Reports* **67**, 19–63 (2010).
30. Snyder, G. J. & Toberer, E. S. Complex thermoelectric materials. *Nat. Mater.* **7**, 105–114 (2008).
31. Jones, W. & March, N. H. *Theoretical Solid State Physics*. (Courier Dover Publications, 1985).
32. Zhao, X. B., Hu, S. H., Zhao, M. J. & Zhu, T. J. Thermoelectric properties of Bi0.5Sb1.5Te3/polyaniline hybrids prepared by mechanical blending. *Mater. Lett.* **52**, 147–149 (2002).
33. Shakouri, A. Recent Developments in Semiconductor Thermoelectric Physics and Materials. *Annu. Rev. Mater. Res.* **41**, 399–431 (2011).
34. Toshima, N., Imai, M. & Ichikawa, S. Organic-inorganic nanohybrids as novel thermoelectric materials: Hybrids of polyaniline and bismuth(III) telluride nanoparticles. *J. Electron. Mater.* **40**, 898–902 (2011).
35. Yu, H. *et al.* Graphene/polyaniline nanorod arrays: synthesis and excellent electromagnetic absorption properties. *J. Mater. Chem.* **22**, 21679 (2012).
36. Zhao, L. D. *et al.* All-scale hierarchical thermoelectrics: MgTe in PbTe facilitates valence band convergence and suppresses bipolar thermal transport for high performance. *Energy Environ. Sci.* **6**, 3346–3355 (2013).
37. See, K. C. *et al.* Water-processable polymer-nanocrystal hybrids for thermoelectrics. *Nano Lett.* **10**, 4664–4667 (2010).
38. Ji, X. & Tritt, T. M. Solution Chemical Synthesis of nanostructured Thermoelectric Materials Solution Chemical Synthesis of nanostructured Thermoelectric Materials. *J. South Carolina Acad. Sci.* **6**, (2008).
39. Xie, W., Tang, X., Yan, Y., Zhang, Q. & Tritt, T. M. Unique nanostructures and enhanced thermoelectric performance of melt-spun BiSbTe alloys. *Appl. Phys. Lett.* **94**, 1–4 (2009).
40. Poudeu, P. F. P., Guéguen, A., Wu, C. I., Hogan, T. & Kanatzidis, M. G. High figure of merit in nanostructured n-type KPbmSbTe m+2 thermoelectric materials. *Chem. Mater.* **22**, 1046–1053 (2010).
41. Pei, Y., May, A. F. & Snyder, G. J. Self-tuning the carrier concentration of PbTe/Ag 2Te composites with excess Ag for high Thermoelectric performance. *Adv. Energy Mater.* **1**,

291–296 (2011).
42. Heremans, J. P., Thrush, C. M., Morelli, D. T. & Wu, M.-C. Thermoelectric Power of Bismuth Nanocomposites. *Phys. Rev. Lett.* **59**, 216801 (1999).
43. Br, R. W. D. & Phys, J. A. Related content The use of semiconductors in thermoelectric refrigeration The use of semiconductors in thermoelectric refrigeration. (1954).
44. Kim, H. *et al.* High thermoelectric performance in convergence and improved by carrier concentration control. *Biochem. Pharmacol.* **20**, 452–459 (2017).
45. WRIGHT, D. A. Thermoelectric Properties of Bismuth Telluride and its Alloys. *Nature* **181**, 834 (1958).
46. Bergvall, P. PROPERTIES OF NON-. **6**, 133–136 (1963).
47. Yim, W. M. & Rosi, F. D. AND THEIR ALLOYS FOR PELTIER COOLING-A REVIEW. **15**, (1972).
48. Sugihara, S., Suzuki, H., Kawashima, S., Fujita, M. & Bnd, K. S. Thermoelectric Properties and Electronic Structures for Impurity -Doped BizTe , ' Department of Materials Science and Ceramic Technology , 2Electric Engineering a Shonan Institute of Technology , Doped Cu , O Se (middle) and 0 (lower) of doped Cu , O . (1998).
49. Chung, D. Y. *et al.* A new thermoelectric material: CsBi4Te6. *J. Am. Chem. Soc.* **126**, 6414–6428 (2004).
50. Poudel, B. *et al.* High-Thermoelectric Performance of Nanostructured Bismuth Antimony Telluride Bulk Alloys. **1871**, 634–639 (2008).
51. Fan, S. *et al.* nanocomposites with enhanced figure of merit. **182104**, (2010).
52. Chen, S., Logothetis, N., Ye, L. & Liu, J. A High Performance Ag Alloyed Nano-scale n-type Bi 2 Te 3 Based Thermoelectric Material. *Mater. Today Proc.* **2**, 610–619 (2015).
53. Ioffe, A. F. Semiconductor Thermoelements and Thermoelectric Cooling (Infosearch, London, 1957). *Google Sch.* 146 (1957).
54. Fritts, R. W. Lead telluride alloys and junctions. *Thermoelectr. Mater. Devices* (1960).
55. Mahan, G. D. Good thermoelectrics. *Solid State Phys.* **51**, 81–157 (1998).
56. Wang, H. *et al.* High-performance Ag0.8Pb18+xSbTe20 thermoelectric bulk materials fabricated by mechanical alloying and spark plasma sintering. *Appl. Phys. Lett.* **88**, 1–4 (2006).
57. Charoenphakdee, A., Yamanaka, S. & Snyder, G. J. Enhancement of Thermoelectric of the Electronic Density of States. *Science (80-.).* **321**, 1457–1461 (2008).
58. Biswas, K. *et al.* High-performance bulk thermoelectrics with all-scale hierarchical architectures. *Nature* **489**, 414 (2012).
59. Biswas, K. *et al.* High-performance bulk thermoelectrics with all-scale hierarchical architectures. *Nature* **489**, 414–418 (2012).
60. Wu, D. *et al.* Superior thermoelectric performance in PbTe-PbS pseudo-binary: Extremely low thermal conductivity and modulated carrier concentration. *Energy Environ. Sci.* **8**, 2056–2068 (2015).
61. Chen, Z. *et al.* Lattice Dislocations Enhancing Thermoelectric PbTe in Addition to Band Convergence. *Adv. Mater.* **29**, 1–8 (2017).
62. Dismukes, J. P., Ekstrom, L., Steigmeier, E. F., Kudman, I. & Beers, D. S. Thermal and electrical properties of heavily doped Ge-Si alloys up to 1300°K. *J. Appl. Phys.* **35**, 2899–2907 (1964).
63. Fleurial, J., Vandersande, J., Scoville, N., Bajgar, C. & Beaty, J. Progress in the optimization of n-type and p-type SiGe thermoelectric materials. *AIP Conf. Proc.* **271**,

759–764 (1993).
64. Kleint, C. A., Heinrich, A., Muehl, T., Schumann, J. & Hecker, M. Structural Properties of Strain Symmetrized Silicon / Germanium (111) Superlattices. *MRS Proc.* **626**, Z8.1 (2000).
65. Giri Joshi, Hohyun Lee, Yucheng Lan, Xiaowei Wang, Gaohua Zhu, Dezhi Wang, Ryan W. Gould, Diana C. Cuff, Ming Y. Tang, Mildred S. Dresselhaus, Gang Chen, and Z. R. *et al.* Enhanced thermoelectric figure of merit in nanostructured n-type silicon germanium bulk alloy. *Appl. Phys. …* **8**, 4670–4674 (2008).
66. Bathula, S. *et al.* Enhanced thermoelectric figure-of-merit in spark plasma sintered nanostructured n-type SiGe alloys. *Appl. Phys. Lett.* **101**, 0–5 (2012).
67. Bathula, S. *et al.* The role of nanoscale defect features in enhancing the thermoelectric performance of p-type nanostructured SiGe alloys. *Nanoscale* **7**, 12474–12483 (2015).
68. Drive, O. G. Pergamon PREPARATION A N D THERMOELECTRIC PROPERTIES OF SEMICONDUCTING ZnaSb 3. **58**, 1119–1125 (1997).
69. Liu, Y. B. *et al.* Synthesis and high-performance thermoelectric properties of beta-Zn 4Sb 3 nanowires. *Mater. Lett.* **84**, 116–119 (2012).
70. Zou, T. *et al.* Enhanced thermoelectric performance of β-Zn4Sb3based nanocomposites through combined effects of density of states resonance and carrier energy filtering. *Sci. Rep.* **5**, 1–9 (2015).
71. Liao, B. *et al.* Significant reduction of lattice thermal conductivity by the electron-phonon interaction in silicon with high carrier concentrations: A first-principles study. *Phys. Rev. Lett.* **114**, 1–6 (2015).
72. Dresselhaus, M. S. *et al.* New directions for low-dimensional thermoelectric materials. *Adv. Mater.* **19**, 1043–1053 (2007).
73. Yang, F., Ikeda, T., Snyder, G. J. & Dames, C. Effective thermal conductivity of polycrystalline materials with randomly oriented superlattice grains. *J. Appl. Phys.* **108**, (2010).
74. Minnich, A. & Chen, G. Modified effective medium formulation for the thermal conductivity of nanocomposites. *Appl. Phys. Lett.* **91**, 1–4 (2007).
75. Liu, L. A continuum theory of thermoelectric bodies and effective properties of thermoelectric composites. *Int. J. Eng. Sci.* **55**, 35–53 (2012).
76. Hao, F., Fang, D.N. & Li, J.Y. Thermoelectric transport in heterogeneous medium: the role of thermal boundary resistance. *Eur. Phys. J. Appl. Phys.* **58**, 30901 (2012).
77. Bergman, D. J. & Fel, L. G. Enhancement of thermoelectric power factor in composite thermoelectrics. *J. Appl. Phys.* **85**, 8205–8216 (1999).
78. Bergman, D. J. & Levy, O. Thermoelectric properties of a composite medium. *J. Appl. Phys.* **70**, 6821–6833 (1991).
79. Yang, Y., Xie, S. H., Ma, F. Y. & Li, J. Y. On the effective thermoelectric properties of layered heterogeneous medium. *J. Appl. Phys.* **111**, (2012).
80. Yang, Y., Ma, F. Y., Lei, C. H., Liu, Y. Y. & Li, J. Y. Is thermoelectric conversion efficiency of a composite bounded by its constituents? *Appl. Phys. Lett.* **102**, (2013).
81. Yang, Y., Lei, C., Gao, C. F. & Li, J. Asymptotic homogenization of three-dimensional thermoelectric composites. *J. Mech. Phys. Solids* **76**, 98–126 (2015).
82. Snyder, G. J. Thermoelectric Power Generation: Efficiency and Compatibility. in *Thermoelectric Handbook, Macro to Nano* (Taylor & Francis, 2006).
83. Ngan, P. H. *et al.* Towards high efficiency segmented thermoelectric unicouples. *Phys.*

Status Solidi Appl. Mater. Sci. **211**, 9–17 (2014).
84. Antonova, E. E. & Looman, D. C. Finite elements for thermoelectric device analysis in ANSYS. *Int. Conf. Thermoelectr. ICT, Proc.* **2005**, 200–203 (2005).
85. Silvester, P. P. & Ferrari, R. L. *Finite elements for electrical engineers*. (Cambridge university press, 1996).
86. Broderick, S. *et al.* Informatics for combinatorial materials science. *JOM* **60**, 56–59 (2008).
87. Li, Y. Predicting materials properties and behavior using classification and regression trees. *Mater. Sci. Eng. A* **433**, 261–268 (2006).
88. Doreswamy, Hemanth, K. S., Vastrad, C. M. & Nagaraju, S. Data Mining Technique for Knowledge Discovery from Engineering Materials Data Sets. in *Advances in Computer Science and Information Technology* (eds. Meghanathan, N., Kaushik, B. K. & Nagamalai, D.) 512–522 (Springer Berlin Heidelberg, 2011).
89. Ashby, M. F. Materials Selection in Mechanical Design Third Edition.
90. Xu, H., Liu, R., Choudhary, A. & Chen, W. A Machine Learning-Based Design Representation Method for Designing Heterogeneous Microstructures. *J. Mech. Des.* **137**, 051403 (2015).
91. Hartigan, J. A. & Wong, M. A. Algorithm AS 136: A K-Means Clustering Algorithm. *J. R. Stat. Soc. Ser. C (Applied Stat.* **28**, 100–108 (1979).
92. Bholowalia, P. EBK-Means : A Clustering Technique based on Elbow Method and K-Means in WSN. **105**, 17–24 (2014).
93. Hoerl, A. E. & Kennard, R. W. Ridge Regression : Biased Estimation for Nonorthogonal Problems Ridge Regression : Biased Estimation Nonorthogonal Problems. **1706**, (2012).
94. Nagelkerke, N. J. D. A Note on a General Definition of the Coefficient of Determination Miscellanea A note on a general definition of the coefficient of determination. **78**, 691–692 (2008).
95. Hawkins, D. M. The Problem of Overfitting. *J. Chem. Inf. Comput. Sci.* **44**, 1–12 (2004).
96. Fushiki, T. Estimation of prediction error by using K-fold cross-validation. *Stat. Comput.* **21**, 137–146 (2011).
97. Bottou, L. Convergence Properties of the K-Means Algorithms.
98. Salimans, T. Weight Normalization : A Simple Reparameterization to Accelerate Training of Deep Neural Networks. (2016).